

**EFFECT OF PIXEL SIZE AND SCINTILLATOR ON  
IMAGE QUALITY OF A CCD-BASED DIGITAL X-RAY  
IMAGING SYSTEM**

By

Michael J. Leal

A Thesis

Submitted to the Faculty

of the

WORCESTER POLYTECHNIC INSTITUTE

in partial fulfillment of the requirements for the

Degree of Master of Science

in

Biomedical Engineering

May 2001

APPROVED:

Andrew Karellas, Ph.D., Major Advisor  
Professor, Department of Radiology  
University of Massachusetts Medical School

Robert A. Peura, Ph.D., Co-Advisor  
Professor  
Biomedical Engineering Department, WPI

Christopher H. Sotak, Ph.D., Co-Advisor  
Professor and Department Head  
Biomedical Engineering Department, WPI

## **Abstract**

The term “Digital X-ray Imaging” refers to a variety of technologies that electronically capture x-ray images. Once captured the images may be electronically processed, stored, displayed and communicated. Digital imaging has the potential to overcome weaknesses inherent in traditional screen-film imaging, with high detection efficiency, high dynamic range and the capability for contrast enhancement. Image processing also makes possible innovative techniques such as computer-aided diagnosis, tomosynthesis, dual-energy imaging, and digital subtraction imaging. Several different approaches to digital imaging are being studied, and in some cases, have been developed and are being marketed. Common to all these approaches are a number of technological and medical issues to be resolved. One of the technological issues is the optimal pixel size for any particular image sensor technology. In general, the spatial resolution of the digital image is limited by the pixel size. Unfortunately while reducing pixel size improves spatial resolution this comes at the expense of signal to noise ratio (SNR). In a scintillator-charge-coupled device (CCD) system, the signal can be increased by improving the efficiency of the scintillator or by reducing noise. This study used a very low noise CCD to determine if image quality, as indicated by the modulation transfer function (MTF), the noise power spectrum (NPS) and the detective quantum efficiency (DQE), could be maintained while reducing pixel size. Two scintillators, one a commonly used radiographic screen the other a thallium doped cesium iodide scintillator, were used and the results compared. The results of this study show that image quality can be maintained as pixel size is reduced and that high DQE can be attained and maintained over a wide range of spatial frequencies with a well designed scintillator.

## **ACKNOWLEDGMENTS**

Mr. Leal wishes to acknowledge the assistance of the following people: teachers, colleagues and friends.

I would like to thank my major advisor, Dr. Andrew Karellas, for his extraordinary knowledge, patience, and encouragement. His suggestions were invaluable and to him I extend my heartfelt gratitude.

I am grateful for the academic advice and encouragement provided by Dr. Robert Peura, and his unceasing willingness to answer questions throughout my tenure as a student at WPI. I also appreciate the support of Dr. Christopher Sotak as a co-advisor.

I would also like to thank Srinivasan Vedantham and Sankararaman Suryanarayanan for sharing their expertise, and humor.

A special thanks to my wife, Cynthia, for her support, understanding and love. I would not be where I am today without her.

## **TABLE OF CONTENTS**

<b>ABSTRACT</b>	<b>i</b>
<b>ACKNOWLEDGEMENTS</b>	<b>ii</b>
<b>I. INTRODUCTION</b>	<b>1</b>
<b>II. METHODS AND MATERIALS</b>	<b>9</b>
A. Equipment	9
B. Presampling modulation transfer function measurement	12
C. Noise power spectrum (NPS) measurement	15
D. NEQ and DQE measurement	22
<b>III. RESULTS</b>	<b>24</b>
A. Presampling MTF	24
B. NPS	29
C. NEQ	38
D. DQE	46
<b>IV. DISCUSSION</b>	<b>53</b>
<b>V. CONCLUSION</b>	<b>55</b>
<b>VI. REFERENCES</b>	<b>57</b>
<b>APPENDIX A – SUPPLEMENTAL FIGURES</b>	<b>60</b>

## LIST OF FIGURES

Figure 1. Schematic of a Scintillator-CCD Detector. Incident X-ray photons interact with the scintillator where they are absorbed and light photons are emitted. Light photons enter the fiberoptic plate and are carried to the CCD where they are detected and converted to electrons.	2
Figure 2. Hardware binning process	6
Figure 3. Experimental setup for MTF measurement	13
Figure 4. 2-D NPS for Kodak MIN-R 2000™ (left) and CsI (right) scintillators. Both images were derived from 16 images with no binning (24 micron pixels) with 5 mAs exposures.	17
Figure 5. Experimental setup for NPS measurement	20
Figure 6. Presampling MTF for Kodak MIN-R 2000™ scintillator for 24 micron (unbinned), 48 micron, 72 micron and 96 micron pixel sizes through hardware binning.	25
Figure 7. Presampling MTF for CsI:Tl scintillator for 24 micron (unbinned), 48 micron, 72 micron and 96 micron pixel sizes through hardware binning.	26
Figure 8. Comparison of MTF with Kodak MIN-R 2000™ and CsI:Tl, with no binning (24 micron). Above 3 cycles/mm the CsI:Tl MTF is greater than the Kodak MIN-R 2000™ MTF and the CsI:Tl MTF is greater than 0.1 up to 13.5 cycles/mm while the Kodak MIN-R 2000™ MTF drops below 0.1 at 9.5 cycles/mm.	27
Figure 9. Comparison of MTF with Kodak MIN-R 2000™ and CsI:Tl, with 4 x 4 binning (96 micron). Above 3 cycles/mm the CsI:Tl MTF is slightly greater than the Kodak MIN-R 2000™ MTF indicating that there may be a slight improvement in resolution when the CsI:Tl scintillator is used.	28
Figure 10. NPS at 5, 10, 16 and 20 mAs with Kodak MIN-R 2000™ with no binning (24 micron). As expected, the normalized NPS decreases as exposure increases.	30

Figure 11. NPS at 5, 10, 16 and 20 mAs with CsI:Tl with no binning (24 micron). As expected, the normalized NPS decreases as exposure increases.	31
Figure 12. NPS comparison of Kodak MIN-R 2000™ and CsI:Tl at 5 mAs with no binning (24 micron). CsI shows lower noise, particularly at low frequencies, than Kodak MIN-R 2000™.	32
Figure 13. NPS comparison of Kodak MIN-R 2000™ and CsI:Tl at 20 mAs with no binning (24 micron). CsI shows lower noise, particularly at low frequencies, than Kodak MIN-R 2000™.	33
Figure 14. NPS for Kodak MIN-R 2000™ at 5 mAs for 24 micron, 48 micron, 72 micron and 96 micron pixel sizes. NPS decreases slightly as pixel size increases reflecting the relative increase in signal. No significant improvement in noise is noted.	34
Figure 15. NPS for CsI:Tl at 5 mAs for 24 micron, 48 micron, 72 micron and 96 micron pixel sizes. As in the case of Kodak MIN-R 2000™, NPS decreases slightly as pixel size increases reflecting the relative increase in signal. No significant improvement in noise is noted.	35
Figure 16. Hardware vs Software 2 x 2 Binning (48 micron), NPS for Kodak MIN-R 2000™ at 5 mAs and 20 mAs. No significant difference is noted between hardware and software binning.	36
Figure 17. Hardware vs Software 2 x 2 Binning (48 micron), NPS for CsI:Tl at 5 mAs and 20 mAs. As with Kodak MIN-R 2000™, no significant difference is noted between hardware and software binning.	37
Figure 18. NEQ for Kodak MIN-R 2000™ with no binning at 5 mAs, 10 mAs, 16 mAs and 20 mAs. As expected, the NEQ increases with exposure.	39
Figure 19. NEQ for CsI:Tl with no binning at 5 mAs, 10 mAs, 16 mAs and 20 mAs. As with Kodak MIN-R 2000™, the NEQ increases with exposure.	40
Figure 20. NEQ for Kodak MIN-R 2000™ with 4 x 4 binning at 5 mAs, 10 mAs, 16 mAs and 20 mAs. As previously noted, the NEQ increases with exposure.	41

Figure 21. NEQ for CsI:Tl with 4 x 4 binning at 5 mAs, 10 mAs, 16 mAs and 20 mAs. As with Kodak MIN-R 2000™, the NEQ increases with exposure.	42
Figure 22. NEQ for Kodak MIN-R 2000™ at 20 mAs (300170 quanta) for 24 micron, 48 micron, 72 micron and 96 micron pixels. The NEQ shows no significant difference as pixel size changes.	43
Figure 23. NEQ for CsI:Tl at 20 mAs (300170 quanta) for 24 micron, 48 micron, 72 micron and 96 micron pixels. The NEQ shows no significant difference as pixel size changes.	44
Figure 24. NEQ comparison of Kodak MIN-R 2000™ and CsI:Tl at 20 mAs for 1 x1 (24 micron) and 4 x 4 (96 micron) binning. The NEQ for the CsI:Tl scintillator is consistently higher than for the Kodak MIN-R 2000™ scintillator.	45
Figure 25. DQE for Kodak MIN-R 2000™ without binning at exposures of 5 mAs, 10 mAs, 16 mAs and 20 mAs. There is minimal influence of exposure on DQE.	47
Figure 26. DQE for CsI:Tl without binning at 5 mAs, 10 mAs, 16 mAs and 20 mAs. As with Kodak MIN-R 2000™, there is minimal influence of exposure on DQE..	48
Figure 27. DQE comparison of Kodak MIN-R 2000™ and CsI:Tl without binning at exposures of 5 mAs and 20 mAs. Not only is the DQE of the CsI:Tl initially higher than that of the Kodak MIN-R 2000™, it remains relatively high and does not begin to drop off until it reaches 10 cycles/mm. While the DQE for the Kodak MIN-R 2000™ falls below 0.1 at 9.5 cycles/mm, the DQE for the CsI:Tl does not drop below 0.1 until 19 cycles/mm.	49
Figure 28. DQE for Kodak MIN-R 2000™ with and without binning at 5 mAs. Other than limiting spatial resolution, pixel size does not influence the DQE in this system.	50
Figure 29. DQE for CsI:Tl with and without binning at 5 mAs. Other than limiting spatial resolution, pixel size does not influence the DQE in this system.	51

## I. INTRODUCTION

The term “Digital X-ray Imaging” refers to a variety of technologies that electronically capture x-ray images. Once captured the images may be electronically processed, stored, displayed and communicated. Images may also be printed on film for viewing and storage.

The first step in digital imaging is image acquisition. Traditionally image acquisition has been accomplished using a fluorescent screen and film. This screen-film technology and associated film processing have advanced in recent years and specialized screens and films have been developed for particular imaging specialties such as mammography<sup>1</sup>. While image quality has improved, screen-film technology has significant limitations with respect to dynamic range, granularity and contrast.

Digital imaging has the potential to overcome these weaknesses with high detection efficiency, high dynamic range and the capability for contrast enhancement. Image processing also makes possible innovative techniques such as computer aided diagnosis<sup>2, 3</sup>, tomosynthesis<sup>4</sup>, dual-energy imaging<sup>5</sup>, and digital subtraction imaging<sup>6</sup>.

Several different approaches to digital imaging are being studied, and in some cases, have been developed and are being marketed. Techniques being studied include dedicated detectors, which may be stationary or slot scanned, and removable stimuable phosphor plates<sup>7</sup> (CR plates), which are similar in appearance and use to current screen-film cassettes. Dedicated detectors may be either direct detection,



such as amorphous selenium<sup>8, 9, 10</sup> or CdZnTe, or indirect detection, using a scintillator to convert x-rays to light and a light sensitive detector such as an active matrix flat-panel imager (AMFPI)<sup>11, 12</sup> or a charge-coupled device (CCD)<sup>13, 14</sup> to detect the light. A schematic of a scintillator-CCD system is shown in Figure 1. Radiographic screens, such as Kodak MIN-R 2000™, have been used as scintillators as well as amorphous silicon and thallium doped cesium iodide (CsI:TI).

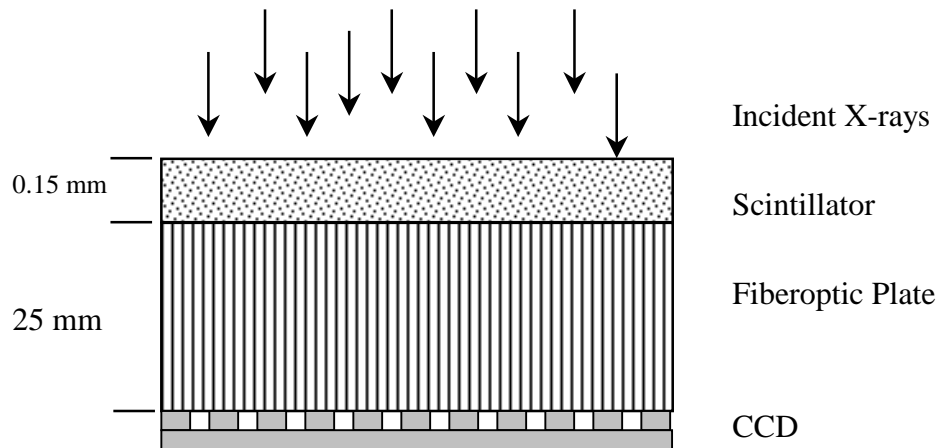


Figure 1. Schematic of a Scintillator-CCD Detector. Incident X-ray photons interact with the scintillator where they are absorbed and light photons are emitted. Light photons enter the fiberoptic plate and are carried to the CCD where they are detected and converted to electrons.

Among those commercially available are CR plates, amorphous silicon-based, flat-panel detectors and scintillator-CCD systems. CR plates are in use in general radiography<sup>15</sup> while amorphous silicon is in use in mammography<sup>16, 17</sup>. In these cases “full field” detectors have been developed, i.e. detectors comparable in size to their screen-film counterparts. The commercial scintillator-CCD systems are used in small field imaging for stereotactic localization and core biopsies<sup>18</sup>.

Common to all these approaches are a number of technological and medical issues to be resolved. One of the technological issues is the optimal pixel size for any particular image sensor technology<sup>19, 20, 21</sup>. In general, the spatial resolution of the digital image is limited by the pixel size. For a given detector technology the spatial resolution is inversely proportional to the pixel size and is defined as the Nyquist limit which states that the maximum resolution,  $R$ , is equal to the inverse of 2 times the pixel size,  $x$ , in mm [ $R = 1/(2 * x)$ ]. From this relationship, a system with a pixel size of 96 microns has a Nyquist limit of 5.2 cycles/mm while a system with a pixel size of 24 microns has a Nyquist limit of 20.8 cycles/mm. High resolution is important in applications such as mammography where microcalcifications on the order of tenths of a mm provide an early indication of cancer. However, this improvement in spatial resolution comes at the expense of signal to noise ratio (SNR) and as SNR degrades so does image quality.

In addition, other components of the system, such as the scintillator, also influence the system resolution. The system resolution ( $R_T$ ) can be derived from the following relationship:

$$\frac{1}{R_T^2} = \frac{1}{R_1^2} + \frac{1}{R_2^2} + \dots + \frac{1}{R_n^2} \quad (1)$$

where  $R_1, R_2, \dots, R_n$  represent the resolution of the various components in the imaging chain. From this relationship, a scintillator with a spatial resolution of 20.8 cycles/mm, coupled with a CCD with a spatial resolution of 20.8 cycles/mm will

result in a system resolution of 14.7 cycles/mm. In current clinical systems, screen-film mammography has spatial resolutions between 16 and 18 cycles/mm. Newer CR systems and amorphous selenium flat-panel systems have spatial resolutions up to 10 cycles/mm, and small field CCD systems have spatial resolutions between 5 and 10 cycles/mm.

In a scintillator-CCD system, SNR can be increased by increasing the x-ray exposure, by improving the efficiency of the scintillator or by reducing noise. Increasing x-ray exposure is undesirable since this increases patient dose. Improving the efficiency of the scintillator is possible, however, this must be accomplished without requiring additional dose, and without introducing artifacts or otherwise degrading the final image. Image degradation typically occurs as a thick scintillator causes greater light diffusion, a condition in which the light produced from one interaction illuminates several pixels of the detector.

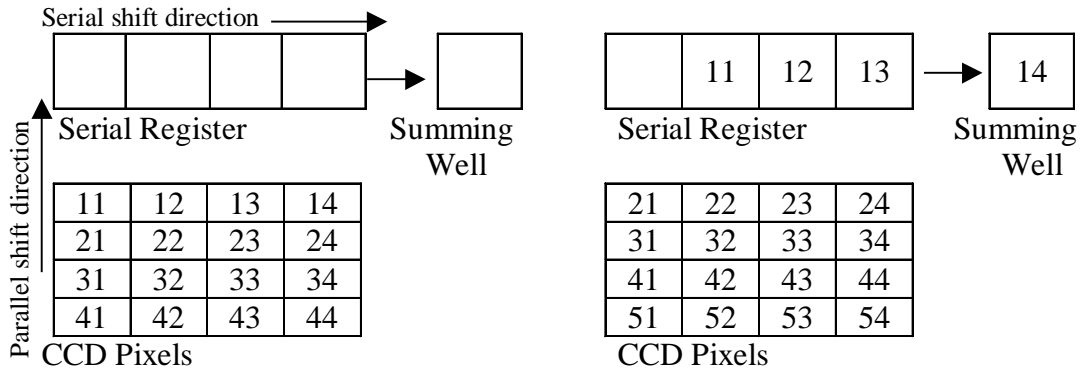
Reducing noise, by using a very low-noise CCD, is also possible. Photon noise, preamplifier noise and dark current noise are the three primary noise sources in a CCD. Dark current is thermally generated charge which can be measured and subtracted from data. There is a noise component of dark current that cannot be isolated and this may influence SNR if the signal is very low. Preamplifier noise is generated by the on-chip output amplifier and is also called read noise. By carefully choosing operating conditions this can be reduced to a few electrons. Photon noise is a fundamental property of the quantum nature of x-rays and light and is unavoidable.

The charge collected by a CCD exhibits a similar Poisson distribution as the incident photons so the noise is equal to the square root of the signal. Photon noise is always present in imaging systems and is simply the uncertainty of the data.

For very low-noise CCDs it is not known if image quality can be maintained while reducing pixel size. It is generally assumed that image quality, as measured by the detective quantum efficiency (DQE), will degrade as pixel size decreases thus negating any gain in resolution<sup>21</sup>. The DQE is a comparison of the output signal to noise ratio ( $SNR_{out}$ ) to the input signal to noise ratio ( $SNR_{in}$ ) and is equal to the square of the  $SNR_{out}$  divided by the square of the  $SNR_{in}$ . Ideally the  $SNR_{out}$  should equal the  $SNR_{in}$  so that the ideal DQE is equal to 1 at all frequencies. In reality the  $SNR_{out}$  is less than the  $SNR_{in}$  so the DQE is always less than 1.

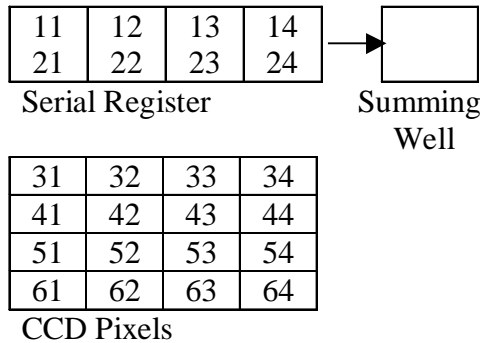
Another method of increasing SNR is pixel binning, which will henceforth be referred to as “binning”. Binning is the process of combining charge from adjacent pixels in a CCD prior to readout (hardware binning) or combining digital values from adjacent pixels in an image (software binning). The process of hardware binning is shown in Figure 2. During exposure each pixel accumulates charge (Figure 2A). Without binning each pixel of the CCD is individually transferred to the serial register, then to the summing well and read (Figure 2B). In this case, each pixel is displayed individually in the final image. With binning adjacent pixels are transferred into the serial register 2, 3 or 4 at a time (Figure 2C). They are then

transferred to the summing well 2, 3 or 4 at a time then read together (Figure 2D). In the case of 2 x 2 binning, 4 adjacent pixels are summed,



A. Individual pixels accumulate electrons during exposure.

B. Individual pixels are shifted to the serial register and then to the summing well during readout in 1 by 1 (full field) mode.



C. Individual pixels are shifted to the serial register two at a time during readout in 2 x 2 binning mode.

D. The serial register is shifted to the summing well two at a time during readout in 2 x 2 binning mode.

Figure 2. Hardware binning process. A. During exposure, individual pixels accumulate electrons in proportion to the light photons they detect. B. During readout, each row of pixels is shifted to the serial register, then each cell of the serial register is shifted to the summing well where it is read out. After all the serial register cells are read the next row of pixels is shifted into the serial register. C. For 2 x 2 binning, 2 rows of pixels are shifted to the serial register where they are summed. D. Two cells of the serial register are then shifted to the summing well, where they are

summed, and read out. After all the serial register cells are read the next 2 rows of pixels is shifted into the serial register.

the sum is then processed and displayed as a single pixel in the final image. If the CCD has 24 micron pixels then 2 x 2 binning will yield an effective pixel size of 48 microns. Similarly, 3 x 3 binning will yield an effective pixel size of 72 microns and 4 x 4 binning will yield an effective pixel size of 96 microns.

One limitation of hardware binning is saturation, the point at which a pixel, the serial register or the summing well reaches its capacity. When saturation occurs any charge beyond the saturation value will be truncated and the final image will reflect the maximum pixel value rather than the actual value. An even greater problem is degradation of contrast due to charge spilling to adjacent pixels. Since 4, 9 or 16 individual pixels may be summed in the summing well its capacity may be exceeded during the binning process even though the individual pixels have not reached saturation. If this occurs, software binning may be a suitable option.

A comparison of full-field digital mammography (FFDM) with screen-film mammography, a procedure dependent on high resolution and high image quality, showed no difference in cancer detection rate<sup>22</sup>. The FFDM system used an amorphous silicon area detector bonded to a cesium iodide crystal (GE Medical Systems) with a pixel size of 100 microns. This limited the spatial resolution of the FFDM system to 5 cycles/mm compared to spatial resolutions between 16 and 18 cycles/mm for current screen-film mammography systems. In order for digital x-ray

imaging to achieve its potential, and exceed comparable screen-film procedures, the limiting spatial resolution must be increased and this must be accomplished without degrading image quality.

This study compares the effect of pixel size and scintillator on image quality of a CCD based digital imaging system. The modulation transfer function (MTF), noise power spectrum (NPS), and detective quantum efficiency (DQE) are used as indicators of image quality. The study was conducted using two different scintillators, one designed as a screen for screen-film mammography, and one designed as a scintillator for use with a CCD. A very low-noise CCD with a 24 micron pixel pitch and with binning capability was used. Both hardware and software binning techniques were used to obtain pixel sizes of 48, 72 and 96 microns.

## II. METHODS AND MATERIALS

### A. Equipment

For this study a “SciTe”, Photometrics, Inc., Tucson, AZ, calibrated 1024 x 1024 pixel (24  $\mu\text{m}$  x 24  $\mu\text{m}$ ) CCD was used. This CCD has a 100% fill factor, meaning that the entire area of each pixel is active and can accumulate charge. The CCD is also fully binnable, i.e. the pixels can be read individually or in groups. The CCD is back illuminated, meaning that the image is focused on the backside of the CCD where there is no gate structure. This gives the CCD high sensitivity to light from the soft x-ray to the near infrared regions of the spectrum. The CCD has thermoelectric cooling with a liquid circulation chiller and thermal isolation around the CCD. The CCD was operated between  $-25^{\circ}\text{C}$  and  $-35^{\circ}\text{C}$  resulting in a dark current between 12.6 electrons/pixel/second and 6 electrons/pixel/second. Read noise for this CCD is 10 electrons rms or better.

The CCD is bonded to a fiberoptic plate approximately 1 inch long. (See Figure 1) The fiberoptic plate carries light from the scintillator to the CCD while protecting the CCD from excessive x-radiation. The fiberoptic is straight so there is neither magnification nor demagnification between the scintillator and the CCD.

Hardware binning for this CCD is accomplished by summing the charges from adjacent pixels during readout (See Figure 2). For example, when 2 x 2 binning is



selected, charge is integrated in the individual pixels while the CCD is exposed. During the parallel read out, the charge from two rows of pixels, rather than a single row, are shifted into the serial register. Charge is then shifted from the serial register two pixels at a time into the summing well. This accumulated charge, from four pixels on the CCD, then becomes one pixel in the acquired image.

For software binning the full field (unbinned) images were binned by averaging pixel values from adjacent pixels and assigning the result to the corresponding binned image pixel. Before software binning the full field images were converted from 16 bit to 32 bit floating point to preclude truncation error.

The x-ray source for the study was a General Electric Senographe 500TS mammography system. The typical breast support/cassette holder was replaced with a support in which the CCD was mounted. The support was designed to maintain a fixed source to image distance (SID) of 650 mm. All measurements were performed at 28 kVp with a Mo/Mo filter/target combination with approximately 4.5 cm of Lucite™ filtration in the beam.

To determine exposure on the surface of the detector a calibrated MDH 1515 (RadCal Corp.) dosimeter with a calibrated mammographic ionization chamber was used. The chamber was mounted on a tripod and placed in the central portion of the x-ray beam at a distance of 45 cm from the x-ray source to the active area of the chamber. The

average of 5 exposures was used to improve precision. Using the inverse square law, the exposure at 65 cm was calculated.

The first scintillator used was a Kodak MIN-R 2000™ screen. This is a commonly used screen in film-screen mammography and is designed for use with Kodak MIN-R 2000™ film. An approximately 2-inch square was cut from a new screen and the adhesive was removed from the back. For this study, the square of screen was placed on top of the fiberoptic plate and a piece of rigid foam was placed on top to assure good contact between the screen and the plate. This was then covered with a piece of paper-backed black plastic and the edges were taped down with black tape to prevent the CCD from being exposed to extraneous room light. In addition, images were acquired with the room lights out.

The second scintillator was a 0.15 mm thick, thallium-doped Cesium Iodide (CsI:Tl) scintillator (Hamamatsu Corporation, Anaheim, CA). This scintillator consists of a thin layer of cesium iodide on a substrate. The cesium iodide layer consists of many thin, rod-shaped, cesium iodide crystals aligned parallel to one another and extending from the top surface of the cesium iodide to the substrate on which they were produced. When an x-ray photon is absorbed in a cesium iodide fiber the cesium iodide produces light. The light reflects within the fiber and is transmitted out one end. This helps to reduce diffusion in the scintillator and makes it well suited for use with a CCD. This scintillator is hygroscopic however and had to be handled carefully

to minimize moisture absorption. This scintillator was placed on the CCD in the same manner as the Kodak MIN-R 2000™ screen.

Images were acquired at each binning combination using x-ray machine settings of 5 milliamp-seconds (mAs), 10 mAs, 16 mAs and 20 mAs. In screen-film mammography, using the same 28 kV energy, output readings of 80 to 120 mAs are typical per exposure. At 65 cm from the x-ray source, this system delivered 0.28 milliRoentgen (mR) per mAs, giving exposures at the CCD of 1.41 mR, 2.81 mR, 4.50 mR and 5.62 mR respectively. This compares favorably with clinical exposures of 8 to 15 mR. At exposures greater than 20 mAs the 4 x 4 pixel elements (super-pixels) exhibited saturation therefore the maximum mAs was limited to 20.

#### B. Presampling modulation transfer function measurement

The presampling modulation transfer function (MTF) was measured according to the technique described by Fujita *et al.*<sup>23</sup> The experimental procedure for this measurement has also been described in detail by Dobbins *et al.*<sup>24</sup> The effects of undersampling have also been described in detail by Dobbins.<sup>25</sup> The experimental setup is shown in Figure 3.

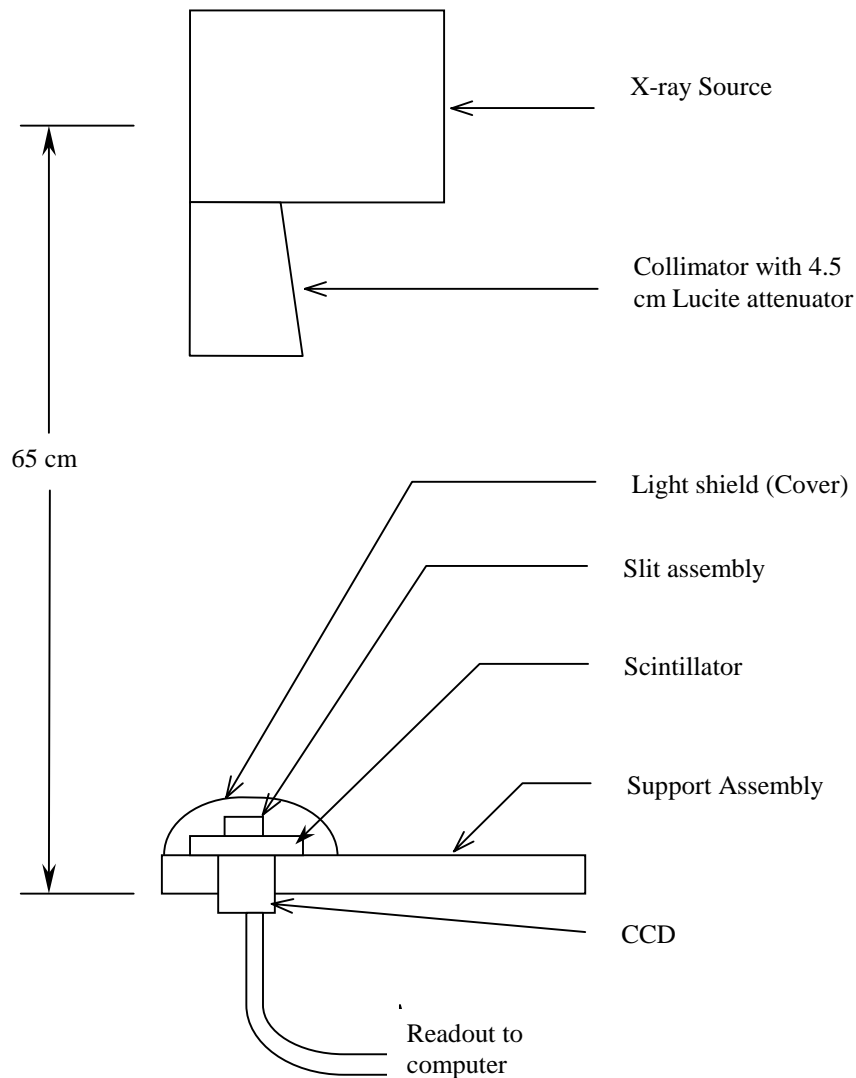


Figure 3. Experimental setup for MTF measurement

An image of a 10 mm long,  $10\mu\text{m}$  ( $\pm 1\mu\text{m}$ ) wide slit made of 1.5 mm thick tantalum placed at a slight angle (approximately  $1.2^\circ$ ) to the anode-cathode axis at the center of the detector was obtained at each binning combination. The area around the slit was covered with lead (0.5 cm thick). Due to the thickness of the slit housing the slit was approximately 7 mm from the surface of the scintillator. The exposure technique was

adjusted to ensure that the tails of the dark-image subtracted slit image obtained had no significant electronic noise. This slit image represents the systems response to a line object and is called the line spread function (LSF) of the system. This blurred image defines the degree of spatial correlation. The appropriate techniques resulted in maximum pixel values between 50% and 70% of the saturation value. The slit image obtained was corrected for variations along the edge of the slit. This was accomplished by normalizing the signal values along the horizontal direction (perpendicular to the anode-cathode axis) by dividing each pixel value by the sum of the pixel values in that particular row.

This normalization method assumes that the slit width is approximately constant over the length used for obtaining the finely sampled LSF and that the signal spreading is approximately equal along each line of data. The validity of these assumptions has previously been verified<sup>16</sup>. Before performing this normalization the pixel values were converted from 16-bit to 32-bit floating-point numbers to avoid loss of information due to truncation. The pixel amplitudes along the column or vertical direction (along the anode-cathode axis) were plotted. This provided the adequate number of individual LSF's needed to obtain a finely sampled LSF. Since each pixel represented a sample of the LSF at a distance equal to the distance between the center of the slit and the pixel center, the finely sampled LSF was obtained by plotting the pixel intensity from the center of the slit. The finely sampled LSF was synthesized by using 34 individual LSF's and normalized to a peak value of one. The Fourier transform (FT) of the finely sampled LSF was performed and the resultant FT was

deconvolved of the finite dimension of the slit by dividing the resultant FT by a sinc function in the frequency domain to provide the presampling MTF.

This process was repeated for each scintillator and for each binning combination.

### C. Noise power spectrum (NPS) measurement

The entire two-dimensional (2D) NPS was computed and an estimation of the one-dimensional (1D) NPS from the 2D NPS was used. The 1D NPS was estimated from the 2D NPS using a radial-averaging technique. For each data value (u,v) at radius r from the center of the image (excluding the axes) the frequency was computed as  $\sqrt{u^2 + v^2}$  for the 1D NPS estimate.

One difficulty was to determine the size of the region-of-interest (ROI) of the noise data required to provide adequate resolution for proper representation of the NPS without the finite size of the ROI overtly affecting the NPS estimate. Since the measured NPS is produced by convolving the “true” NPS with the sinc<sup>2</sup> function in the frequency domain, due to the finite ROI of the noise data, the choice of ROI is a concern. In this study the limiting factor was the maximum size of the 4 x 4 binned image. Since the CCD had 1024 x 1024 pixels the unbinned image size was 1024 x 1024 pixels. When the images were binned the size was reduced to 512 x 512 pixels for 2 x 2 binning, 341 x 341 pixels for 3 x 3 binning and 256 x 256 pixels for 4 x 4

binning. Previous studies have shown that a 256 x 256 ROI is the smallest ROI required for proper representation of the NPS with minimum spectral distortion<sup>16</sup>. Therefore, the 256 x 256 ROI was utilized for NPS estimation. For full field (1 x 1) images, which contain 1024 x 1024 pixels, the central 256 x 256 pixels were used as the ROI for the NPS estimate. For 2 x 2 binned images, which contain 512 x 512 pixels, the central 256 x 256 pixels were used as the ROI for the NPS estimate. For 3 x 3 binned images, which contain 341 x 341 pixels, the central 256 x 256 pixels were used as the ROI for the NPS estimate. For 4 x 4 binned images, the entire 256 x 256 pixel image was used for the NPS estimate.

The other difficulty was to determine the number of NPS realizations needed to be averaged in order to obtain a smooth and accurate curve depicting the noise power spectrum. Ideally, a large number of NPS realizations are needed so that they can be averaged to obtain a smooth spectrum. Previous experience has shown that the ensemble average of 15 NPS realizations taken from the same location through 15 images is sufficient to accurately characterize the NPS of the system<sup>16</sup>. Initially it was decided to use 16 images for each NPS determination since we could select four 256 x 256 ROI's from full field and 2 x 2 binned images. This would reduce the total number of raw images needed, however, it was found that the resultant NPS curves exhibited greater variability than those generated from 16 separate images. The final results are based on 16 images acquired at each exposure for each binning configuration. Figure 4 shows the 2-D NPS images for Kodak MIN-R 2000™ (left)

and CsI (right) scintillators. Both images were derived from 16 images with no binning (24 micron pixels) with 5 mAs exposures.

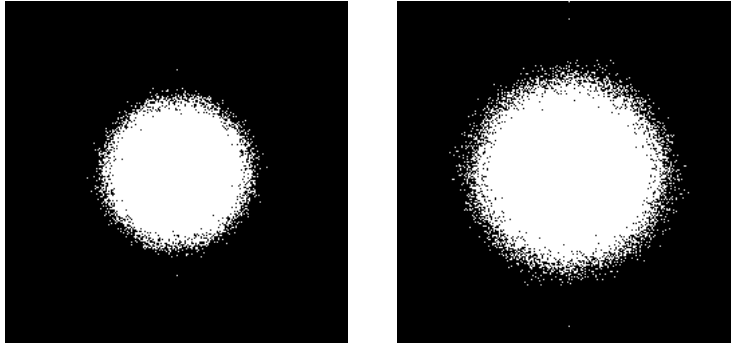


Figure 4. 2-D NPS for Kodak MIN-R 2000™ (left) and CsI (right) scintillators. Both images were derived from 16 images with no binning (24 micron pixels) with 5 mAs exposures.

Problems associated with background trends such as from the heel effect can corrupt the noise spectrum and provide artificially inflated values<sup>15, 24</sup> along the axes. The heel effect is due to the geometry of the target in the mammographic x-ray tube and the manner in which the tube is mounted. The result is a slightly higher exposure at the outer edge (chest wall) of the image receptor than at the inner edge (nipple side). The exposure decreases linearly along the image receptor resulting in a density gradient along the image. This is advantageous in mammographic imaging since the breast is thickest at the chest wall and thinnest at the nipple, however, this contributes to noise in the NPS measurement. Techniques for suppression of such background trends have been described by various authors<sup>15, 24</sup>. We considered surface (ramp) fitting each ROI and subtracting these background trends, however, we felt that this would smooth the images and reduce values. Hence, we did not surface fit or



otherwise process the ROI's, but we avoided using data values directly on the axes, as they were not representative in amplitude of the rest of the 2D NPS in the vicinity of the axes.

The determination of the noise power spectrum requires that the detector be linear and shift invariant.<sup>26</sup> The linear response and sensitivity of the system was measured by averaging the pixel intensity over a 256 x 256 ROI at the center of the CCD at various exposure levels. All images for the noise power spectral estimate used for calculation of DQE were acquired by accumulating charge over a 5 second period during which the x-ray exposure was made. These raw images were dark subtracted [Equation (2)], to remove the effect of dark current, and flat-field corrected [Equation (3)], to adjust for the variation in response between pixels,

$$\text{dark subtracted}_i(x,y) = \text{raw}_i(x,y) - \text{dark}_i(x,y), \quad (2)$$

$$\text{flat field}_i(x,y) = \frac{\text{dark subtracted}_i(x,y)}{(1/n)\sum_{i=1}^n \text{dark subtracted}_i(x,y)} \times \frac{1}{m^2} \sum_{y=1}^m \sum_{x=1}^m \left[ \frac{1}{n} \sum_{i=1}^n \text{dark subtracted}_i(x,y) \right] \quad (3)$$

where  $\text{raw}_i(x,y)$  and  $\text{dark}_i(x,y)$  represent the raw and dark ROIs, respectively;

$(1/n) \sum_{i=1}^n \text{dark subtracted}_i(x,y)$  is the average of the dark subtracted ROI;

$\frac{1}{m^2} \sum_{y=1}^m \sum_{x=1}^m \left[ \frac{1}{n} \sum_{i=1}^n \text{dark subtracted}_i(x,y) \right]$  is the mean of the average of the dark

subtracted ROIs; and, in our case,  $m=256$  and  $n= 16$ . The result is a nominally uniform image.

The ROIs (256 x 256) used for the NPS analysis were taken from the same location (centered) from multiple (16) images. Though the detector might not to be completely shift invariant, the process of flat-field correcting and using the same ROI from multiple images for NPS analysis allows for the reasonable assumption of the “shift-invariant” property of the system<sup>16</sup>.

The noise power spectra were determined at four exposure levels, and with two different scintillators, and were obtained with 4.5 cm thick Lucite in the x-ray beam path. This thickness of Lucite was used as it was found to be the median thickness range (4.5 - 4.99 cm) of the compressed breast from a random sample of 100 patient exams obtained from a population of 1400 patients<sup>16</sup>. In order to minimize the detection of scattered radiation, the 4.5-cm-thick Lucite block was mounted onto the tube housing. The experimental setup for NPS measurement is shown in Figure 5.

Sixteen dark-image subtracted, flat-field corrected, images were acquired as described previously. Before performing dark-image subtraction and flat-field correction, the pixel intensity values were converted to 32 bit floating point numbers, from the original 16 bit digital values, to avoid truncation error. The ensemble average of the squares of the magnitude of these 16 Fourier transformed 256 x 256 ROI, scaled as shown in Equation (4), provided the 2D raw noise power spectrum,  $NPS_{\text{raw}}(u, v)$ .

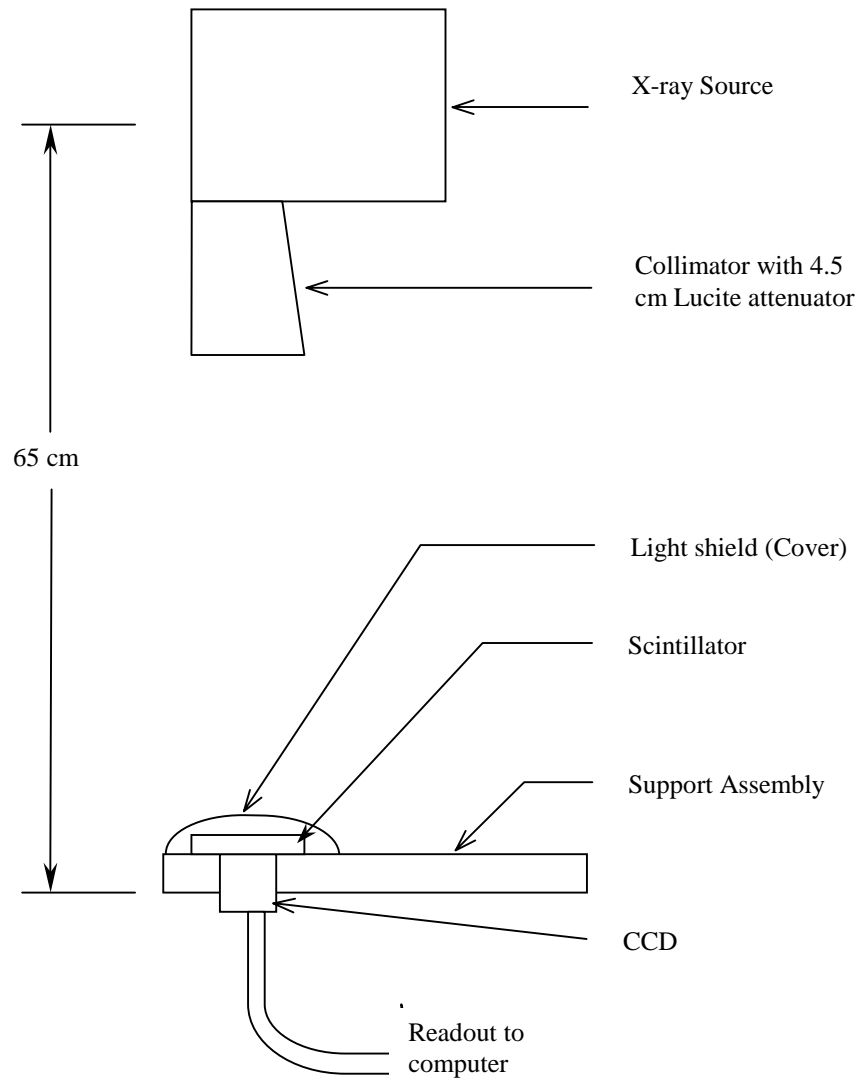


Figure 5. Experimental setup for NPS measurement

The  $NPS_{raw}(u, v)$  was obtained by

$$NPS_{raw}(u, v) = \frac{\langle |FT[flatfield(x, y)]|^2 \rangle}{N_x N_y} \Delta_x \Delta_y \quad (4)$$

where  $\langle [FT[flatfield(x, y)]]^2 \rangle$  represents the ensemble average of the squares of the magnitude of the Fourier transformed 256 x 256 ROI's,  $N_x$  and  $N_y$  are the number of elements in the  $x$  and  $y$  directions respectively (which are equal and 256 in this case), and  $\Delta_x$  and  $\Delta_y$  are the pixel pitch in the  $x$  and  $y$  directions, respectively. The pixel pitch for the full field image is 24  $\mu\text{m}$ . For the 2 x 2, 3 x 3 and 4 x 4 binned images, the pixel pitch is 48  $\mu\text{m}$ , 72  $\mu\text{m}$  and 96  $\mu\text{m}$  respectively.

The 2D  $NPS_{normalized}(f)$  to be used for the DQE calculations was obtained by scaling the 2D  $NPS_{raw}(f)$  for the mean signal by

$$NPS_{normalized}(f) = \frac{NPS_{raw}(f)}{(\text{mean signal of } 256 \times 256 \text{ ROI})^2} \quad (5)$$

The mean signal of the 256 x 256 ROI is expressed in digital values.

To compute the noise equivalent quanta (NEQ), a commonly used form of the signal to noise ratio, and the DQE, a 1D NPS curve was required. This was achieved by using a radial-averaging technique. For each data value  $(u,v)$  at radius  $r$  from the center of the image (excluding the axes), the frequency was computed as  $\sqrt{u^2 + v^2}$  for the 1D NPS estimate. The final 1D NPS at each exposure level is the average of 128 data points grouped into frequency bins. Each bin represents 0.164

cycles/mm for 24 micron pixels (no binning), 0.082 cycles/mm for 48 micron pixels (2 x 2 binning), 0.055 cycles/mm for 72 micron pixels (3 x 3 binning) and 0.042 cycles/mm for 96 micron pixels (4 x 4 binning).

#### D. NEQ and DQE measurement

The NEQ was computed as

$$\text{NEQ}(f) = \frac{\text{MTF}^2(f)}{\text{NPS}_{\text{normalized}}(f)} \quad (6)$$

The NEQ of the system was computed for the four exposure levels at each binning configuration. For the purpose of calculating the DQE of the imaging system, Eqs (7) and (8) were used<sup>24</sup>:

$$\text{DQE}(f) = \frac{\text{MTF}^2(f)}{\text{NPS}_{\text{normalized}}(f)q} \quad (7)$$

and hence

$$\text{DQE}(f) = \frac{\text{NEQ}(f)}{q} \quad (8)$$

where  $MTF(f)$  is the modulation transfer function of the system;  $NPS_{normalized}(f)$  is the normalized noise power spectrum of the imaging system;  $q$  is the number of x-ray photons incident on the detector per unit area;  $NEQ(f)$  is the noise equivalent quanta of the imaging system and  $f$  is the spatial frequency. The only factor that needs to be determined is  $q$  and this has previously been done for this system<sup>16</sup>.

### III. RESULTS

#### A. Presampling MTF

An object can be represented in the frequency domain by a series of discrete frequencies. The modulation transfer function (MTF) is a measure of the ability of a system to reproduce the original object frequencies in the final image. Figures 6 through 9 show and compare the MTF curves for this imaging system with a Kodak MIN-R 2000™ scintillator and with a CsI:Tl scintillator. Figure 6 and Figure 7 show that the MTF decreases slightly as pixel size increases for both scintillators. Since larger pixels cannot adequately sample high frequencies this result is expected. Larger pixels can sample low frequencies as well as small pixels can so the curves tend to merge at low frequencies. Because small objects or abrupt changes in x-ray attenuation are represented by high frequencies systems must be capable of detecting these higher frequencies in order to display small objects. This is especially important in applications such as mammography where microcalcifications tenths of a mm in diameter provide early evidence of cancer.

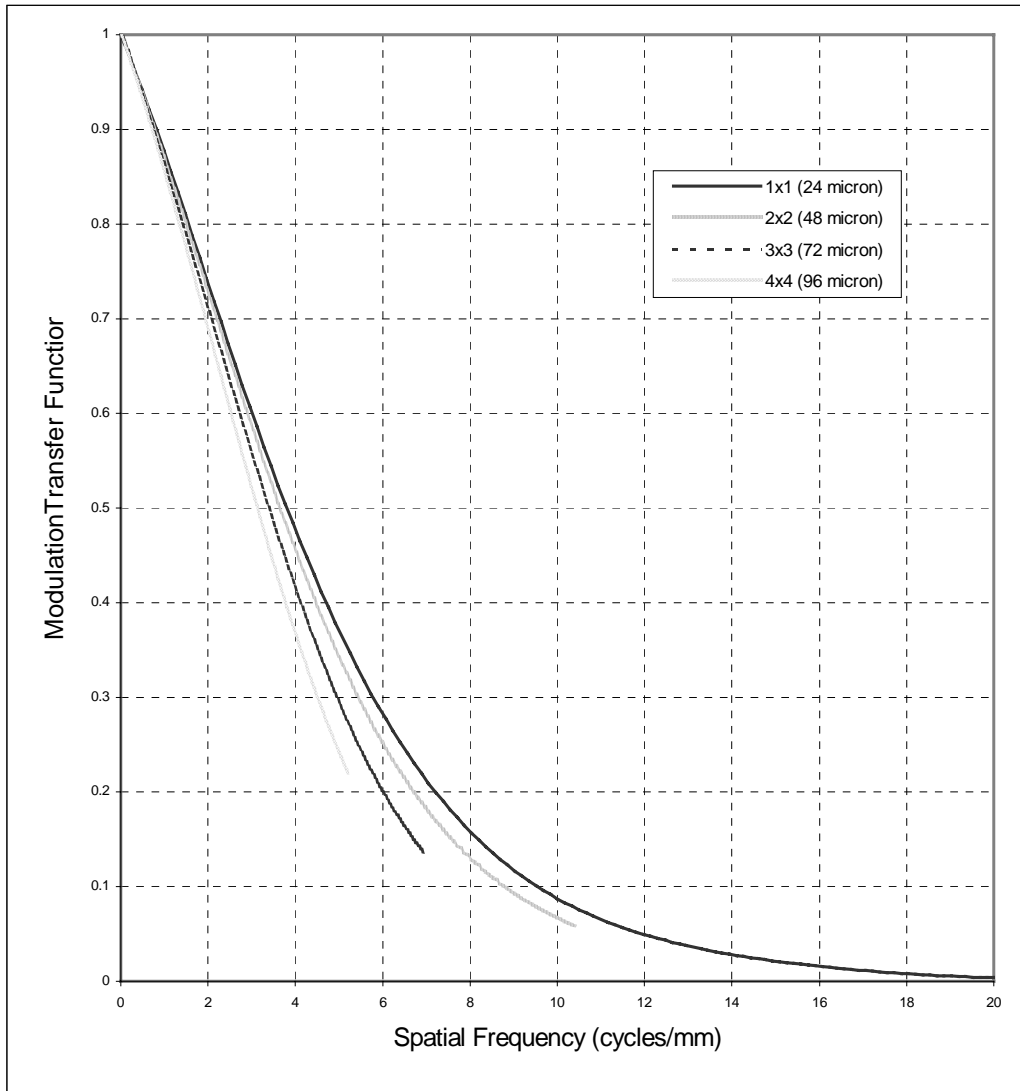


Figure 6. Presampling MTF for Kodak MIN-R 2000™ scintillator for 24 micron (unbinned), 48 micron, 72 micron and 96 micron pixel sizes through hardware binning.



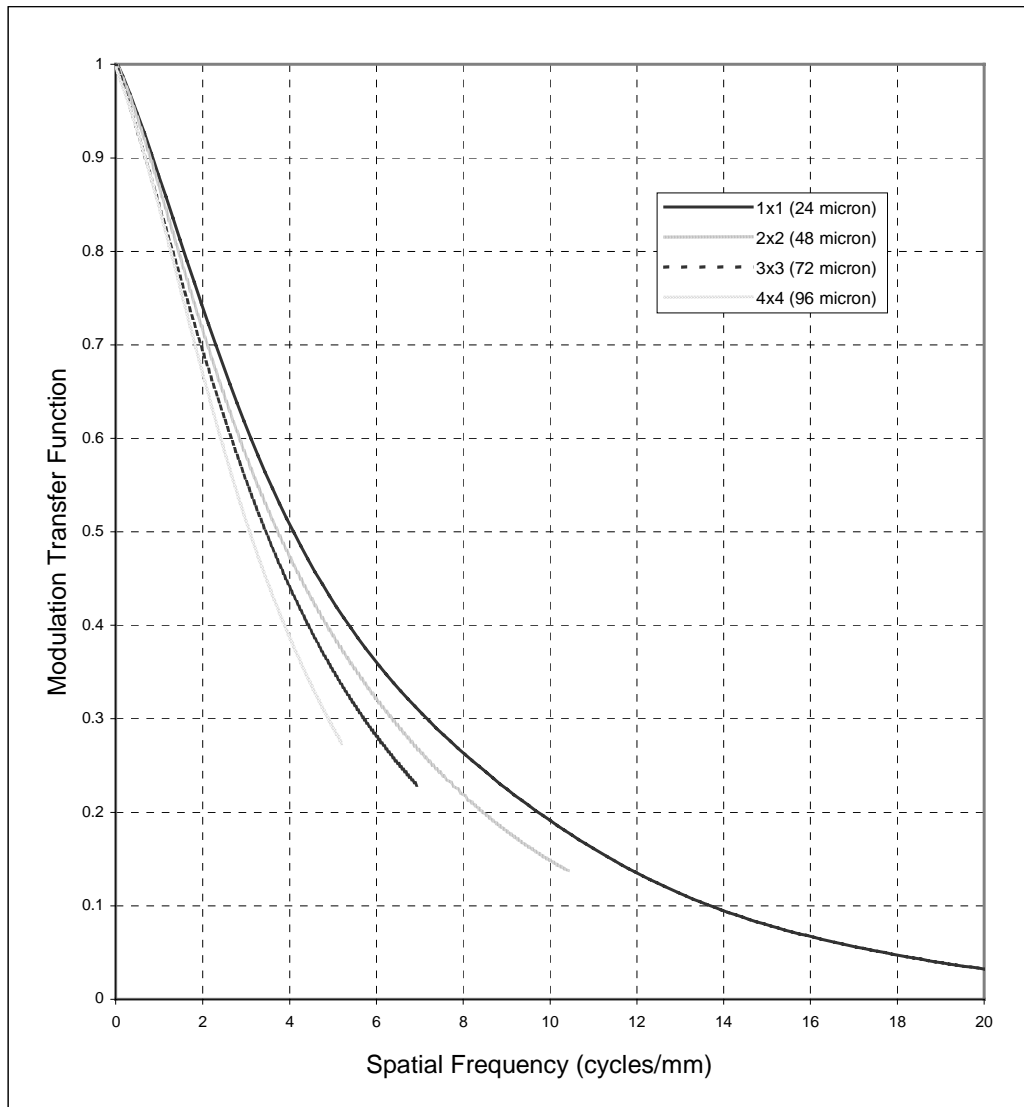


Figure 7. Presampling MTF for CsI:Tl scintillator for 24 micron (unbinned), 48 micron, 72 micron and 96 micron pixel sizes through hardware binning.

Figure 8 and Figure 9 compare the MTF curves of Kodak MIN-R 2000™ and CsI:Tl with and without pixel binning. In Figure 8 the curves show the MTF without binning, i.e. with a 24 micron pixel. This shows that up to about 3 cycles/mm the two scintillators are comparable. Above 3 cycles/mm the CsI:Tl MTF is greater than the Kodak MIN-R 2000™ MTF. In this system, the MTF of Kodak MIN-R 2000™

drops below 0.1 at about 9.5 cycles/mm while the CsI:Tl MTF remains above 0.1 until about 13.5 cycles/mm. This shows that with the CsI:Tl scintillator this system is capable reproducing higher frequencies than with the Kodak MIN-R 2000™.

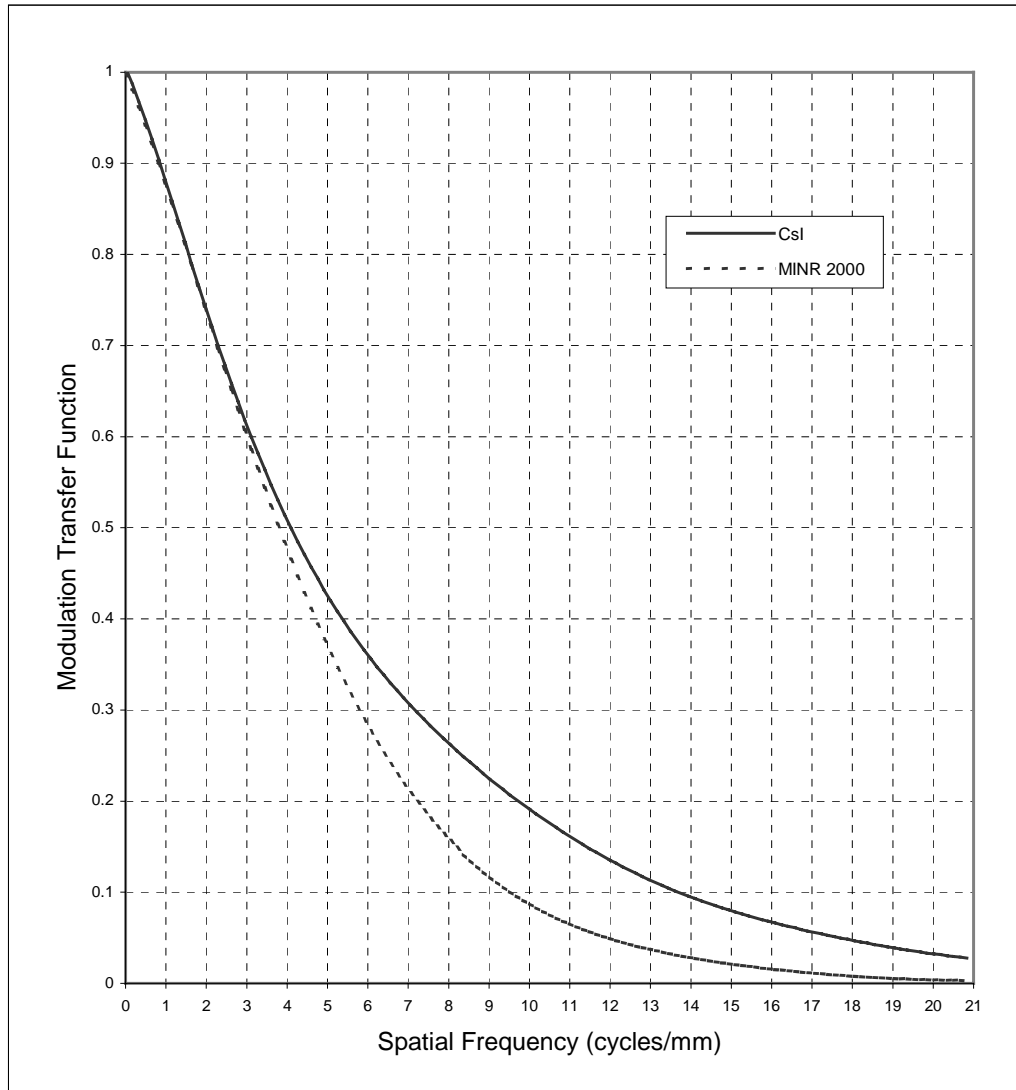


Figure 8. Comparison of MTF with Kodak MIN-R 2000™ and CsI:Tl, with no binning (24 micron). Above 3 cycles/mm the CsI:Tl MTF is greater than the Kodak MIN-R 2000™ MTF and the CsI:Tl MTF is greater than 0.1 up to 13.5 cycles/mm while the Kodak MIN-R 2000™ MTF drops below 0.1 at 9.5 cycles/mm.

Figure 9 compares the MTF curves with 4 x 4 hardware binning which produces a 96 micron pixel. In this case the Kodak MIN-R 2000™ curve appears to be slightly higher than the CsI:Tl curve up to about 3.5 cycles/mm. From that point up to the

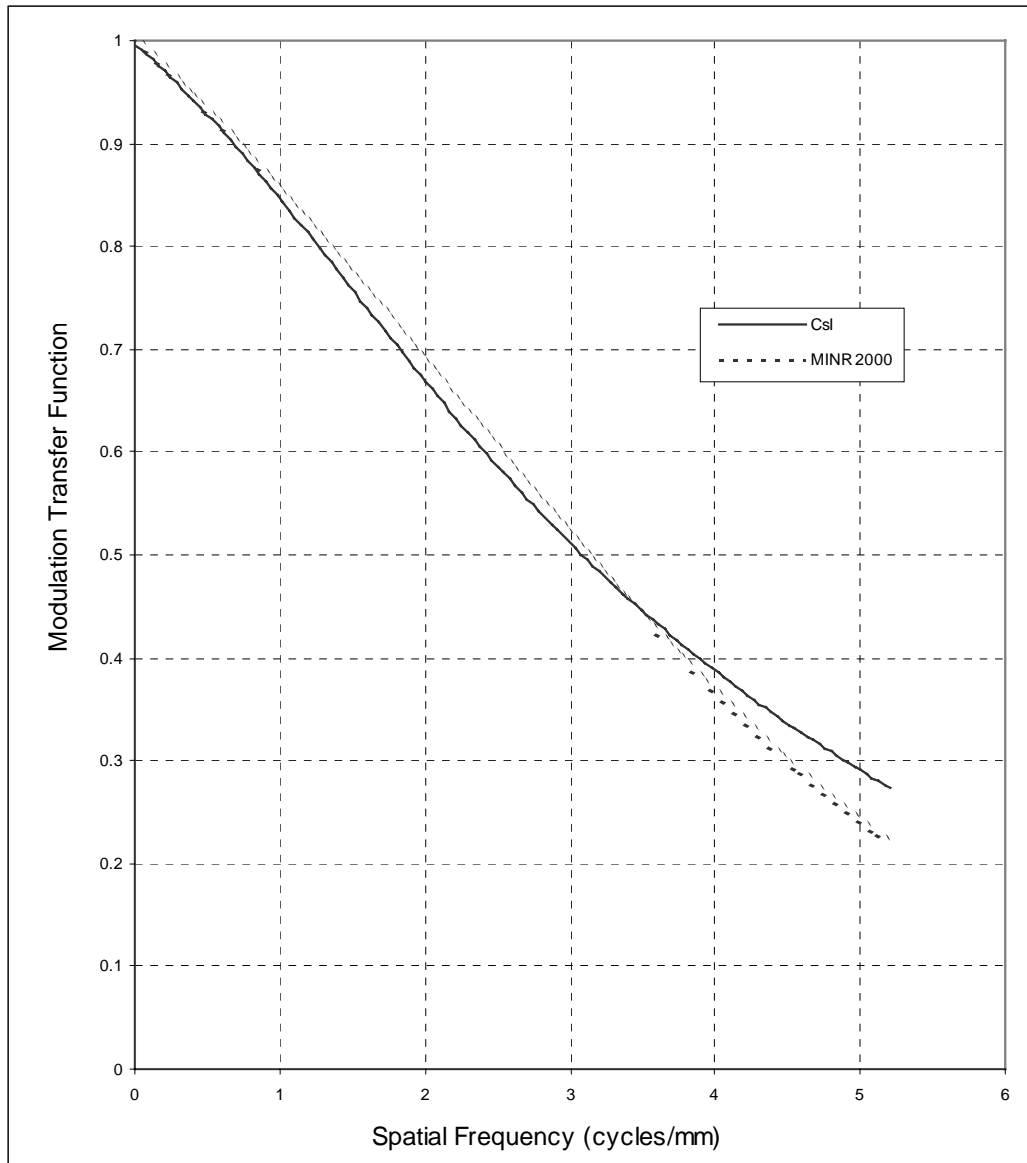


Figure 9. Comparison of MTF with Kodak MIN-R 2000™ and CsI:Tl, with 4 x 4 binning (96 micron). Above 3 cycles/mm the CsI:Tl MTF is slightly greater than the Kodak MIN-R 2000™ MTF indicating that there may be a slight improvement in resolution when the CsI:Tl scintillator is used.

Nyquist limit, CsI:Tl shows a higher MTF. This indicates that there may be a slight improvement in resolution when the CsI:Tl scintillator is used. This is typical of 2 x 2 and 3 x 3 binning (48 micron and 76 micron pixels, respectively), for which results are not shown.

## B. NPS

Figures 10 through 17 show and compare the 1-D NPS curves for this system. Figures 10 and 11 show the NPS curves for Kodak MIN-R 2000™ and CsI:Tl respectively, with no binning, at the four exposure levels used. Both curves show that the normalized NPS decreases as exposure increases for both scintillators. Figures 12 and 13 compare the NPS curves for Kodak MIN-R 2000™ and CsI:Tl, with no binning, at exposures of 5 mAs (1.41 mR) and 20 mAs (5.62 mR), respectively. Both curves show that CsI:Tl has lower noise than Kodak MIN-R 2000™. This is also true for exposures of 10 mAs (2.82 mR) and 16 mAs (4.50 mR), for which results are not shown.

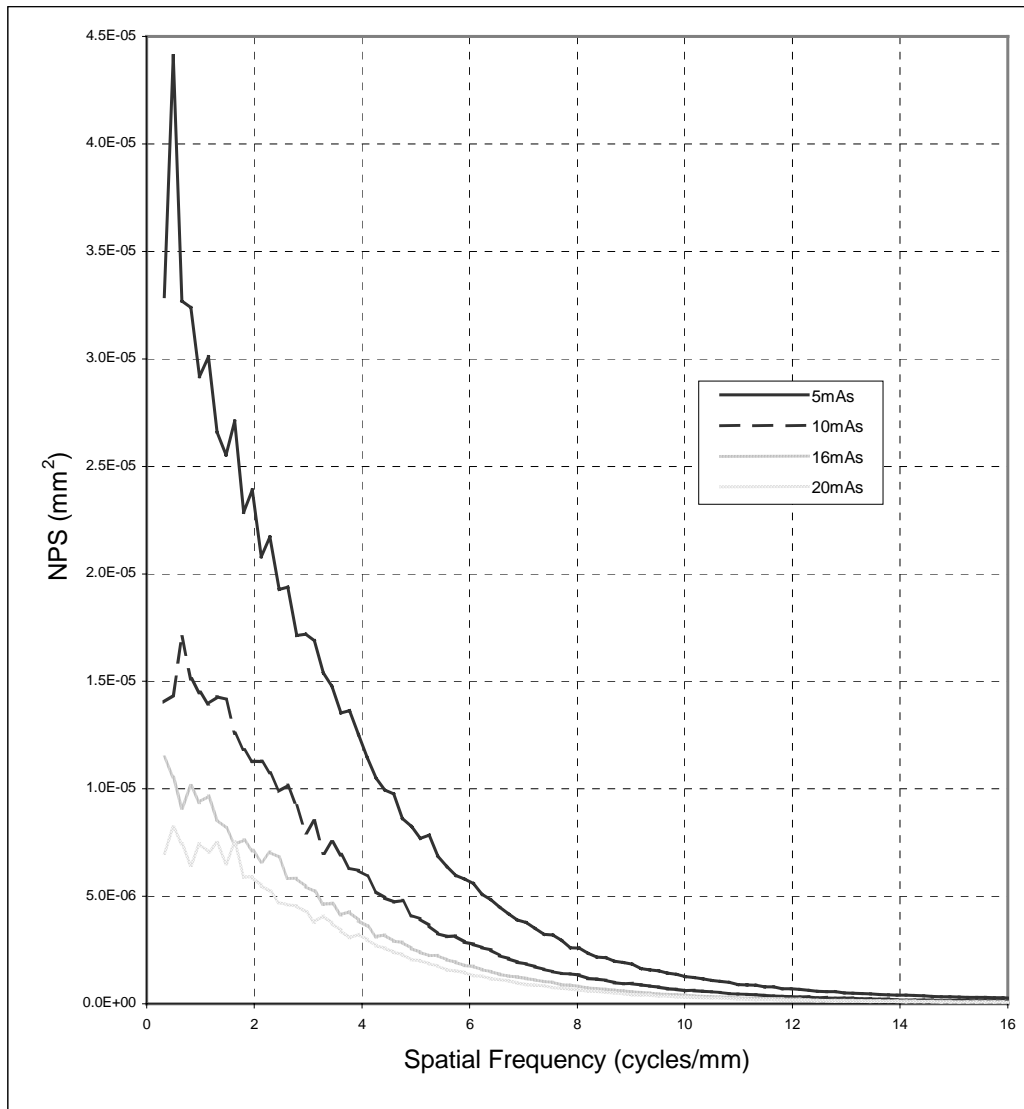


Figure 10. NPS at 5, 10, 16 and 20 mAs with Kodak MIN-R 2000™ with no binning (24 micron). As expected, the normalized NPS decreases as exposure increases.

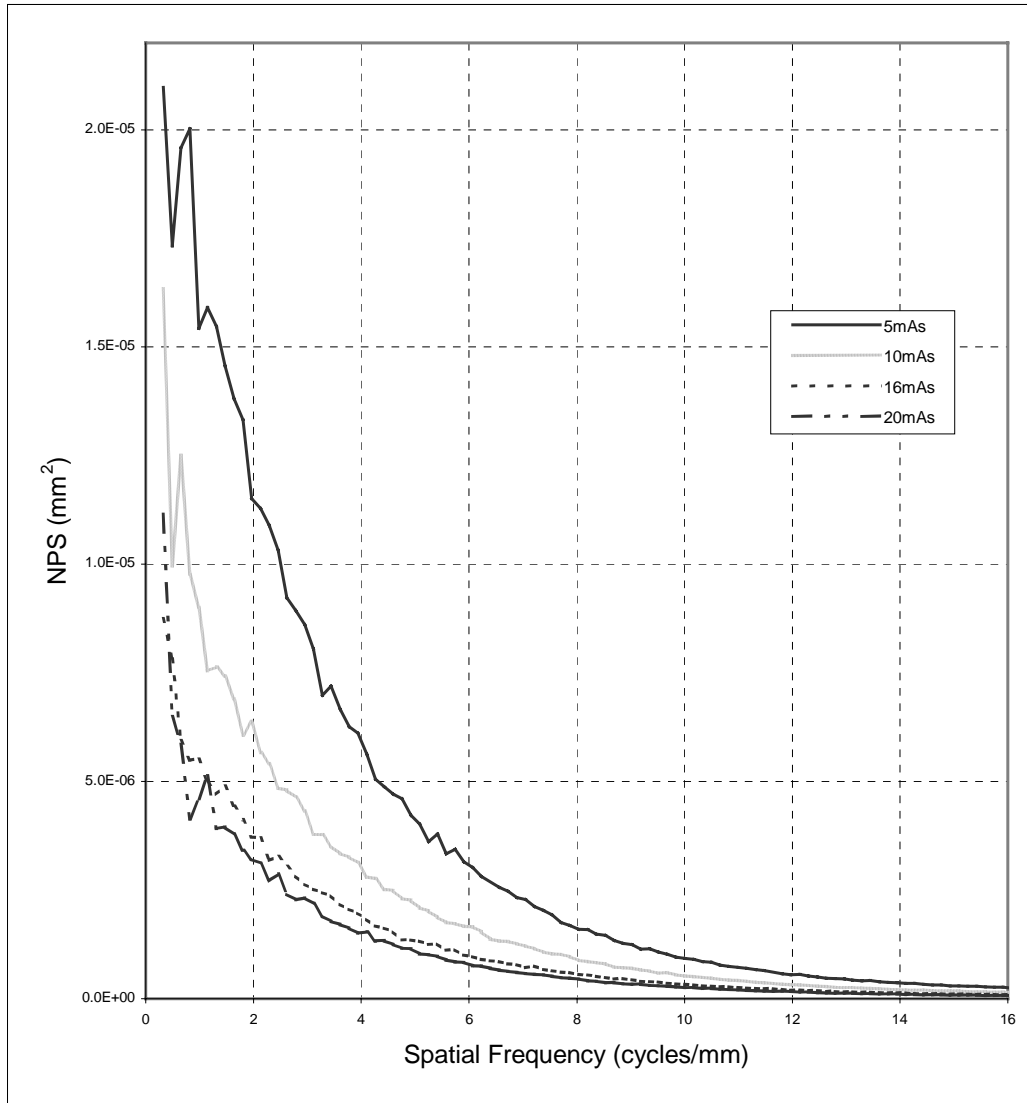


Figure 11. NPS at 5, 10, 16 and 20 mAs with CsI:Tl with no binning (24 micron). As expected, the normalized NPS decreases as exposure increases.

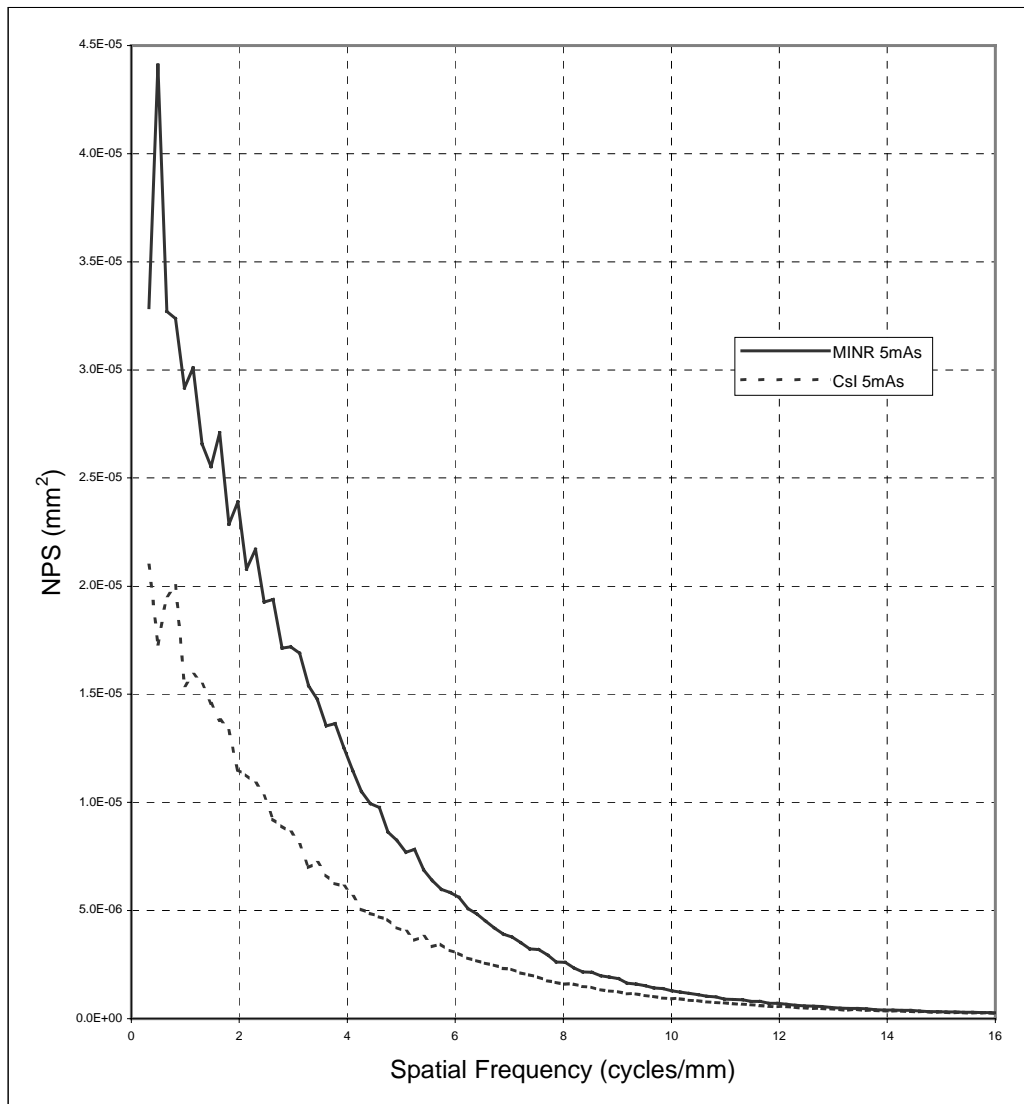


Figure 12. NPS comparison of Kodak MIN-R 2000™ and CsI:Tl at 5 mAs with no binning (24 micron). CsI shows lower noise, particularly at low frequencies, than Kodak MIN-R 2000™.

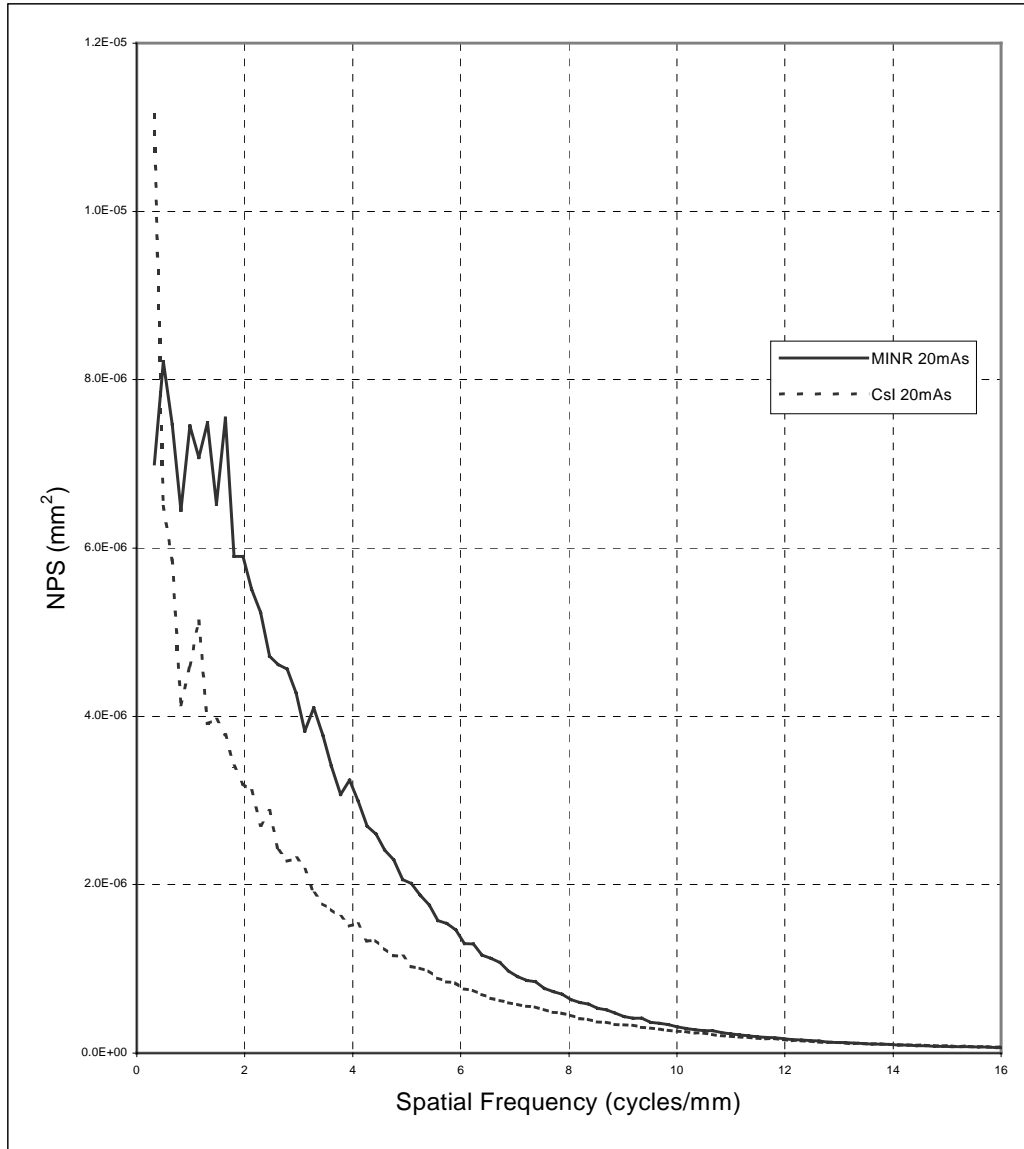


Figure 13. NPS comparison of Kodak MIN-R 2000™ and CsI:Tl at 20 mAs with no binning (24 micron). CsI shows lower noise, particularly at low frequencies, than Kodak MIN-R 2000™.



There was much less of a difference in the 1-D NPS as a function of pixel size as shown in Figures 14 and 15. In these figures hardware binning is used. Figure 14 shows the NPS as pixel size increases for Kodak MIN-R 2000™ at 5 mAs, Figure 15 shows the same curves for CsI:Tl. These curves at 20 mAs are shown as Figures A1 and A2 of Appendix A.

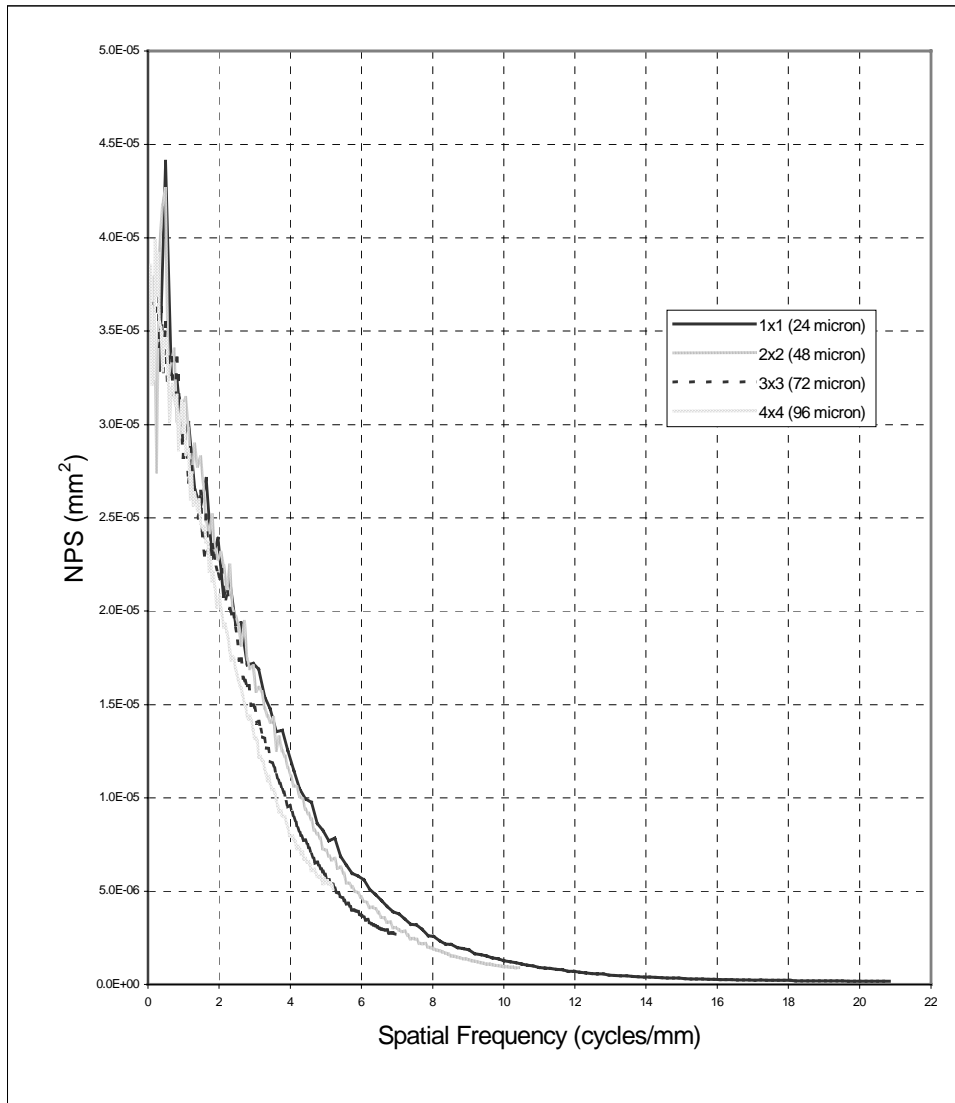


Figure 14. NPS for Kodak MIN-R 2000™ at 5 mAs for 24 micron, 48 micron, 72 micron and 96 micron pixel sizes. NPS decreases slightly as pixel size increases reflecting the relative increase in signal. No significant improvement in noise is noted.

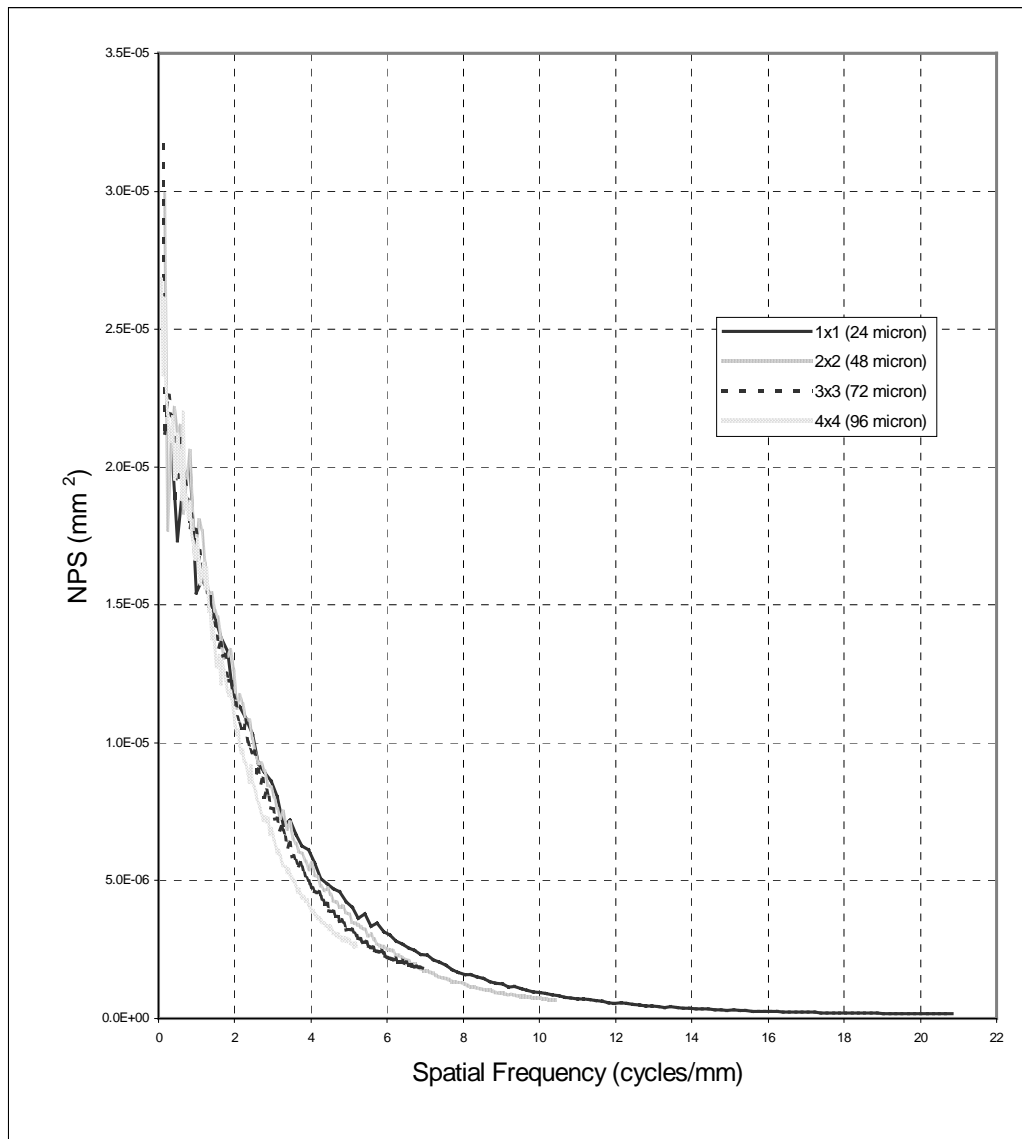


Figure 15. NPS for CsI:Tl at 5 mAs for 24 micron, 48 micron, 72 micron and 96 micron pixel sizes. As in the case of Kodak MIN-R 2000™, NPS decreases slightly as pixel size increases reflecting the relative increase in signal. No significant improvement in noise is noted.

In all cases, and in the cases of 10 mAs and 16 mAs exposures which are not shown, NPS decreases slightly as pixel size increases. While this reflects the relative increase in signal as pixel size increases it does not indicate a significant improvement in noise as is noted when comparing Kodak MIN-R 2000™ and CsI:Tl.

The effect of hardware vs software binning is shown in Figures 16 and 17. The software binned values were calculated from the unbinned (24 micron) images at each exposure level. Figure 16 shows NPS curves for Kodak MIN-R 2000™ using hardware and software binning at exposures of 5 mAs and 20 mAs for 2 x 2 binning. Figure 17 shows the same curves for CsI:Tl.

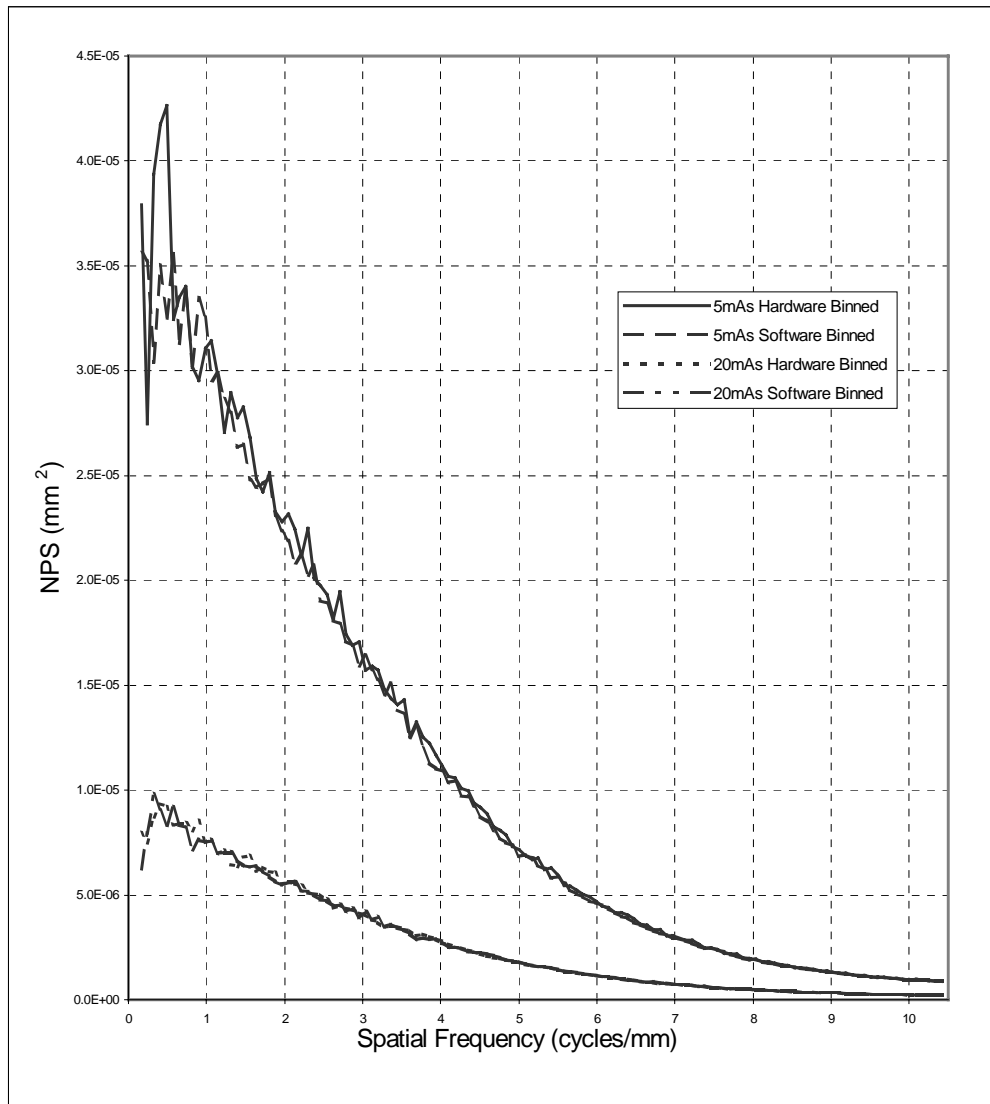


Figure 16. Hardware vs Software 2 x 2 Binning (48 micron), NPS for Kodak MIN-R 2000™ at 5 mAs and 20 mAs. No significant difference is noted between hardware and software binning.

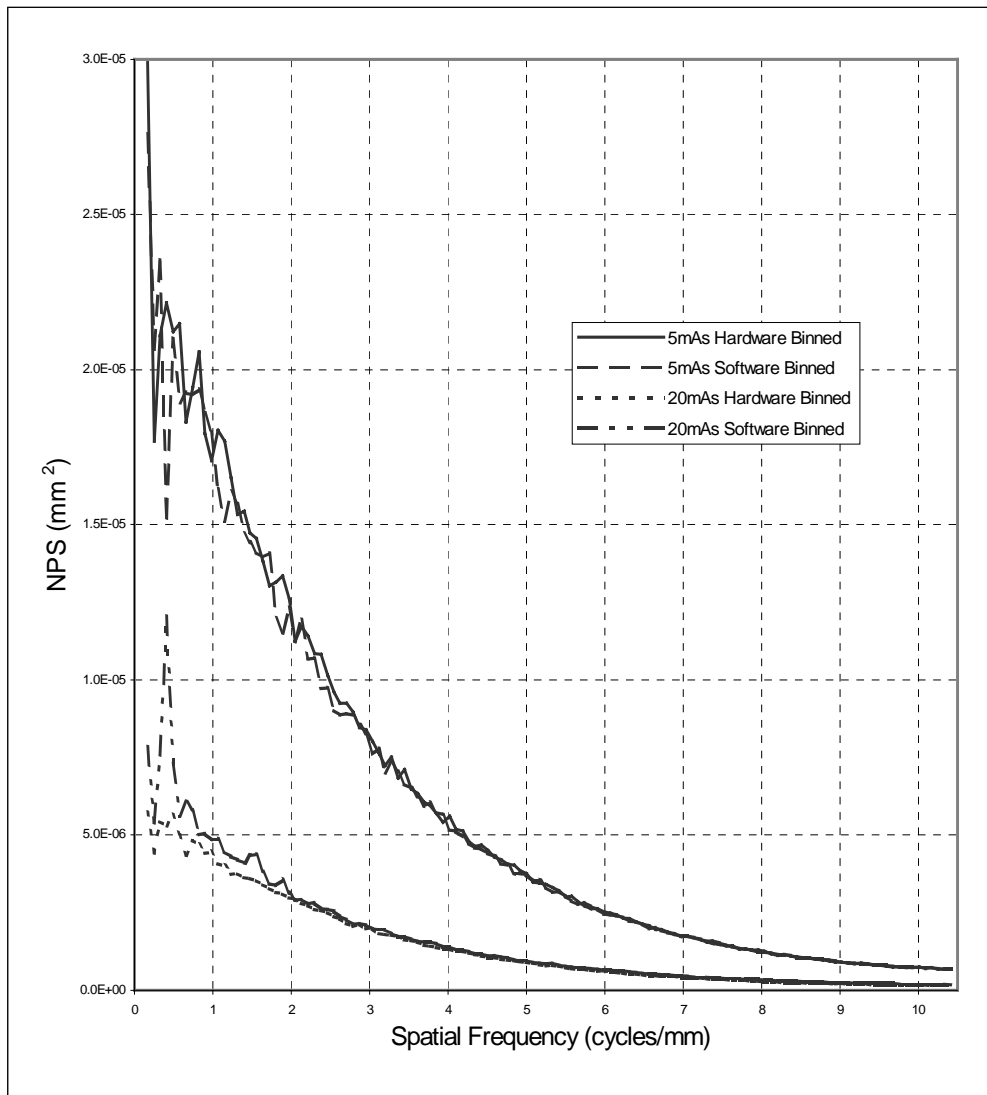


Figure 17. Hardware vs Software 2 x 2 Binning (48 micron), NPS for CsI:Tl at 5 mAs and 20 mAs. As with Kodak MIN-R 2000™, no significant difference is noted between hardware and software binning.

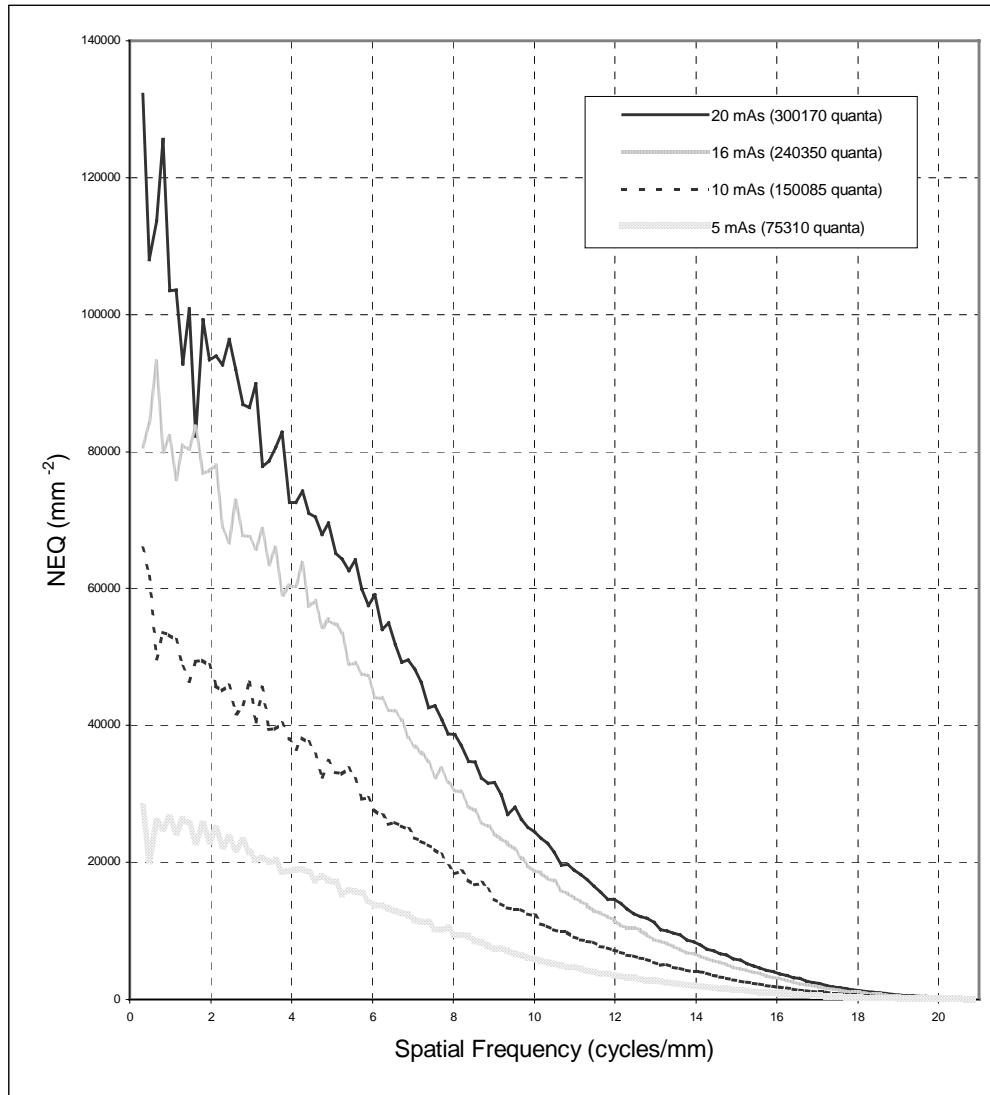
These curves for 3 x 3 binning (72 micron) and 4 x 4 binning (96 micron) are included in Appendix A as Figures A3 and A4 for Kodak MIN-R 2000™, and A5 and A6 for CsI:Tl. Not shown are NPS curves for exposures of 10 mAs and 16 mAs, which follow the trends of the curves shown. In all cases, there is no significant difference between hardware and software binning.

This indicates that the read noise per pixel for this CCD is very low when compared to the signal per pixel and that where maximum resolution is not needed either binning technique can be used without degrading image quality.

### C. NEQ

The NEQ is shown in Figures 18 through 24 indicating how the signal to noise ratio changes with exposure and pixel size. Figures 18 and 19 show how the NEQ with no binning varies at different exposures for Kodak MIN-R 2000™ and CsI:Tl respectively. As expected in both cases, NEQ is higher at higher exposures. With hardware binning the results are the same, as shown in Figures 20 and 21, NEQ with 4 x 4 binning (96 micron) at different exposures for Kodak MIN-R 2000™ and CsI:Tl respectively. This was also true with 2 x 2 binning (48 micron) and 3 x 3 binning (72 micron) for which results are not shown.

Figure 18. NEQ for Kodak MIN-R 2000™ with no binning at 5 mAs, 10 mAs, 16 mAs and 20 mAs. As expected, the NEQ increases with exposure.



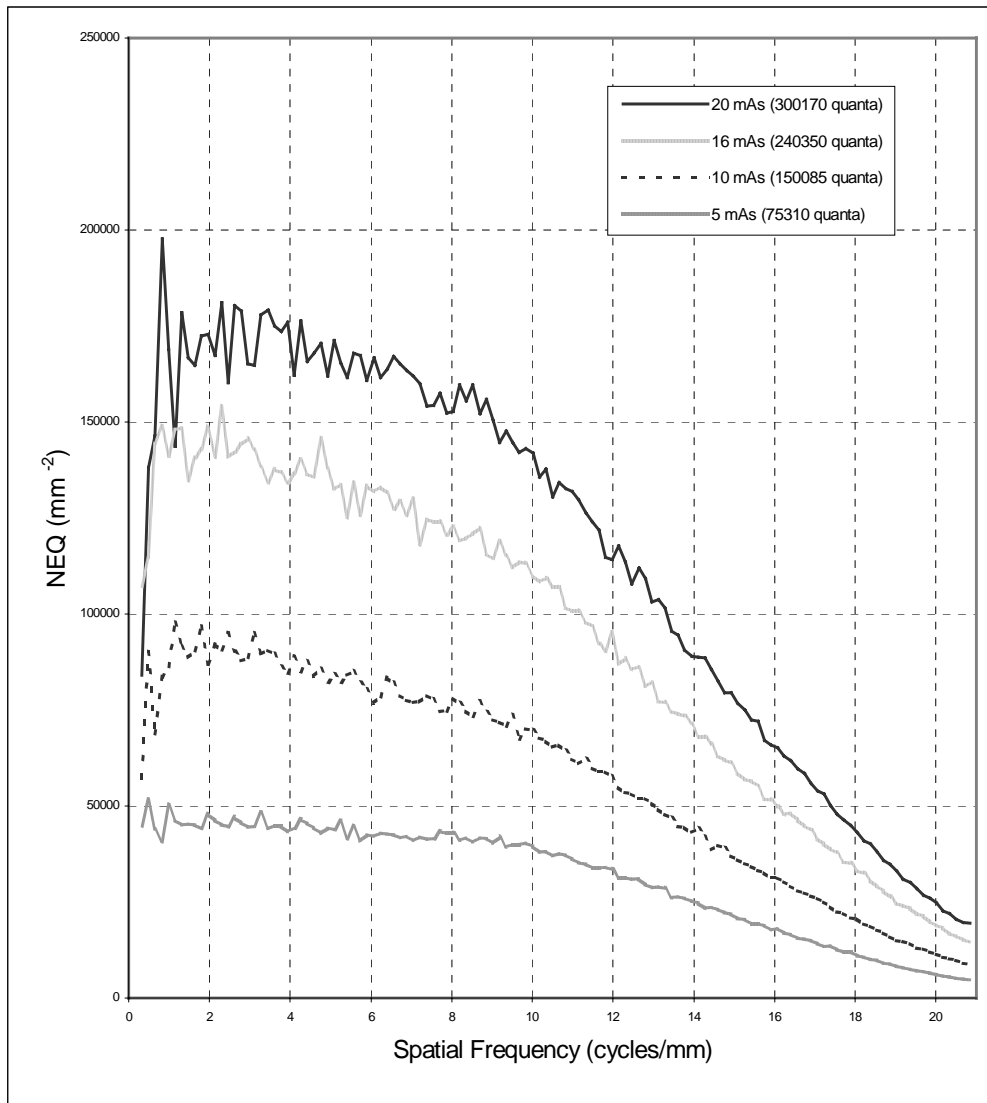


Figure 19. NEQ for CsI:Tl with no binning at 5 mAs, 10 mAs, 16 mAs and 20 mAs. As with Kodak MIN-R 2000™, the NEQ increases with exposure.

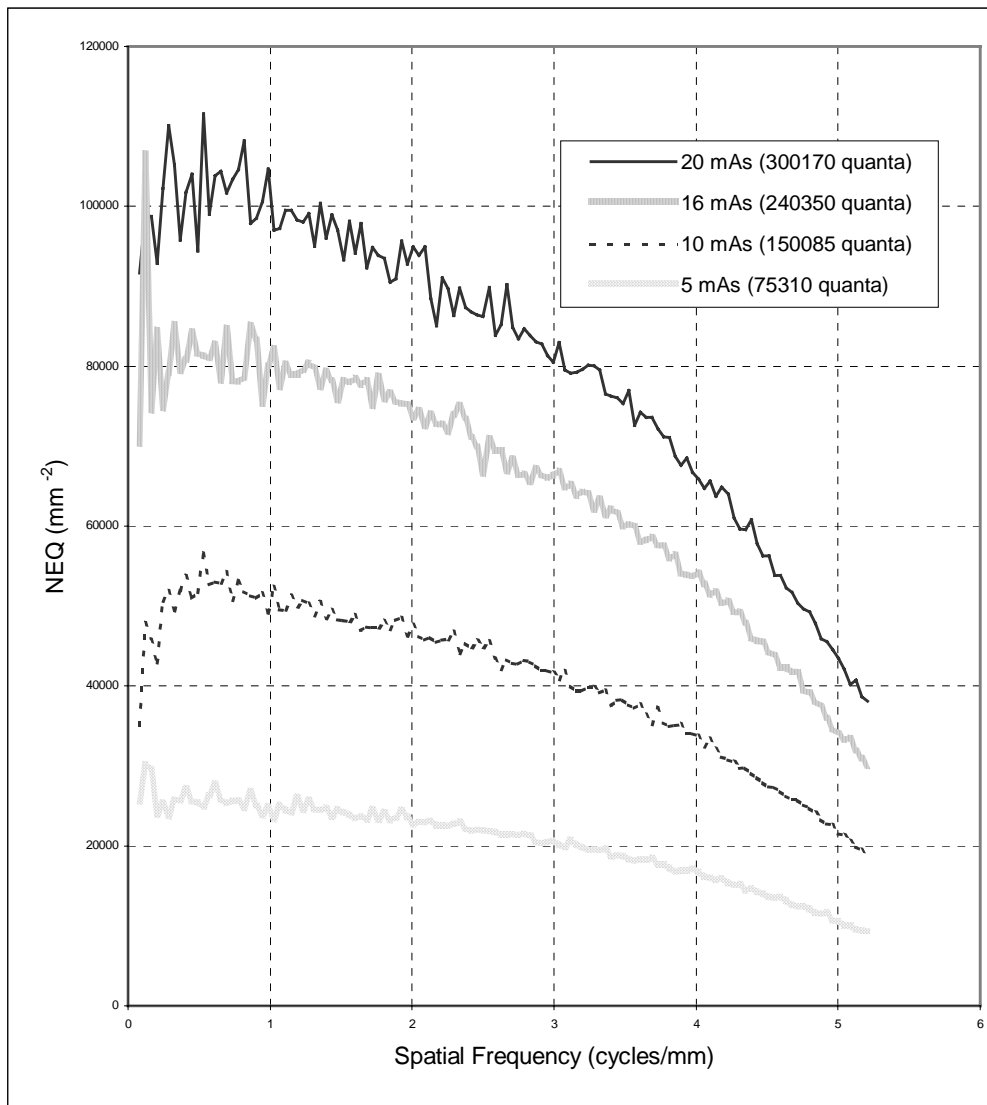


Figure 20. NEQ for Kodak MIN-R 2000™ with 4 x 4 binning at 5 mAs, 10 mAs, 16 mAs and 20 mAs. As previously noted, the NEQ increases with exposure.



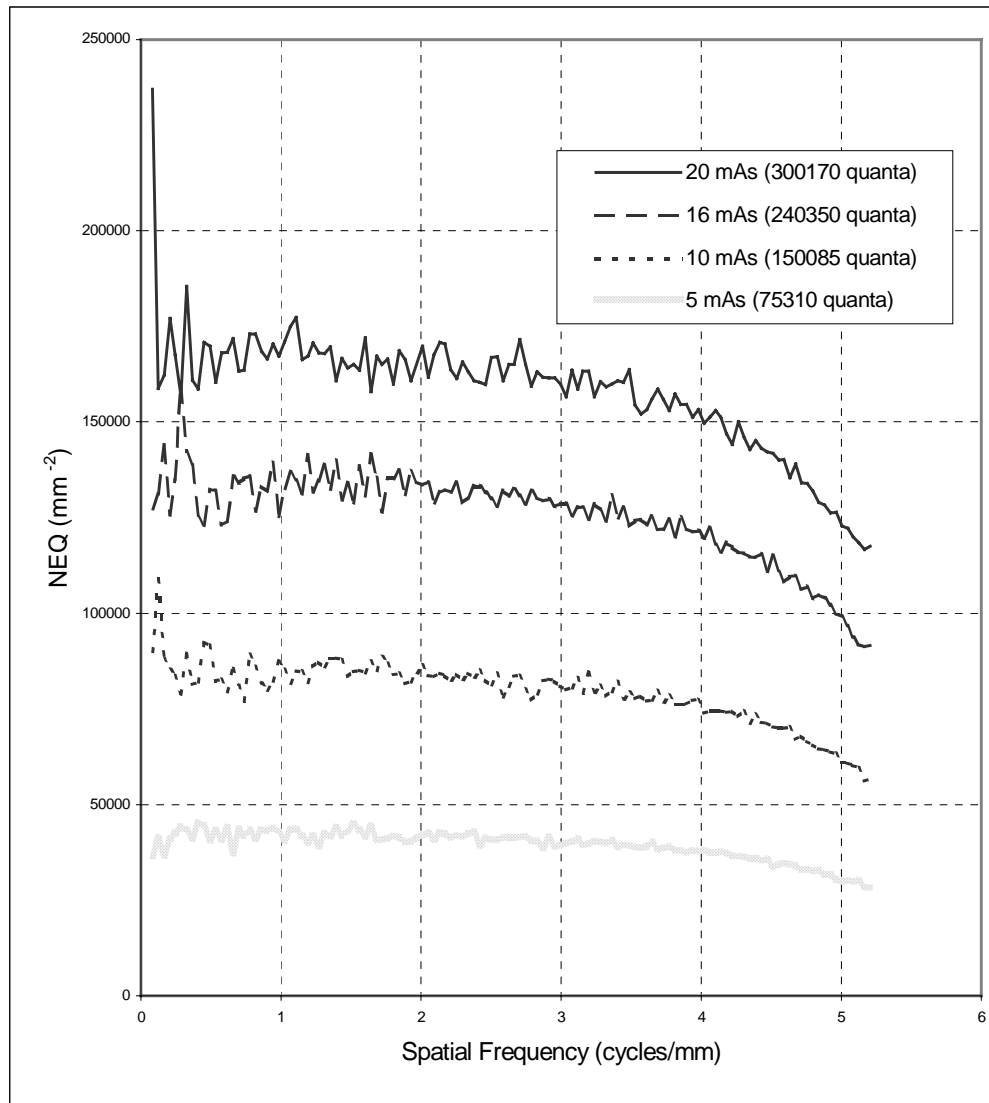


Figure 21. NEQ for CsI:Tl with 4 x 4 binning at 5 mAs, 10 mAs, 16 mAs and 20 mAs. As with Kodak MIN-R 2000™, the NEQ increases with exposure.

Using the highest exposure, 20 mAs (5.62 mR), NEQ shows no significant difference as pixel size changes. Figures 22 and 23 show the NEQ at 20 mAs, for Kodak MIN-R 2000™ and CsI:Tl, respectively for each pixel size.

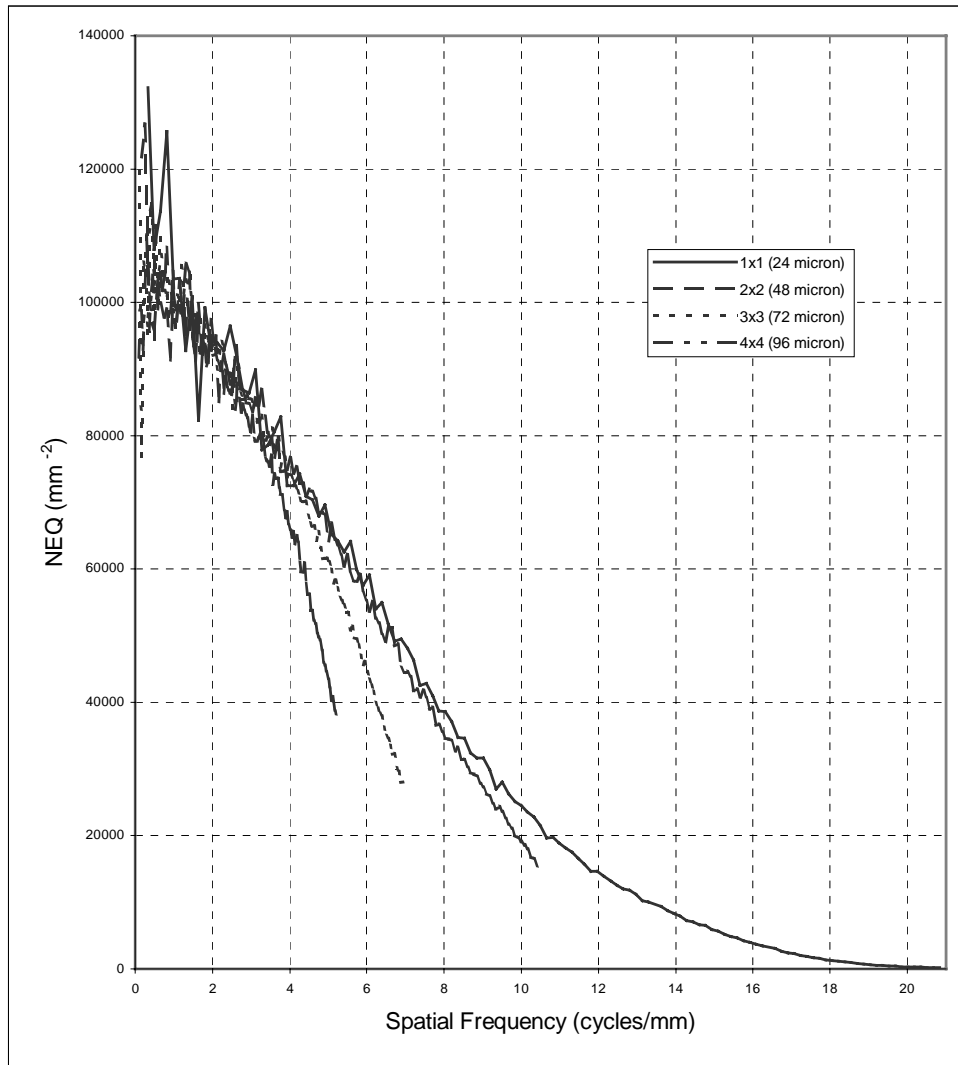


Figure 22. NEQ for Kodak MIN-R 2000™ at 20 mAs (300170 quanta) for 24 micron, 48 micron, 72 micron and 96 micron pixels. The NEQ shows no significant difference as pixel size changes.

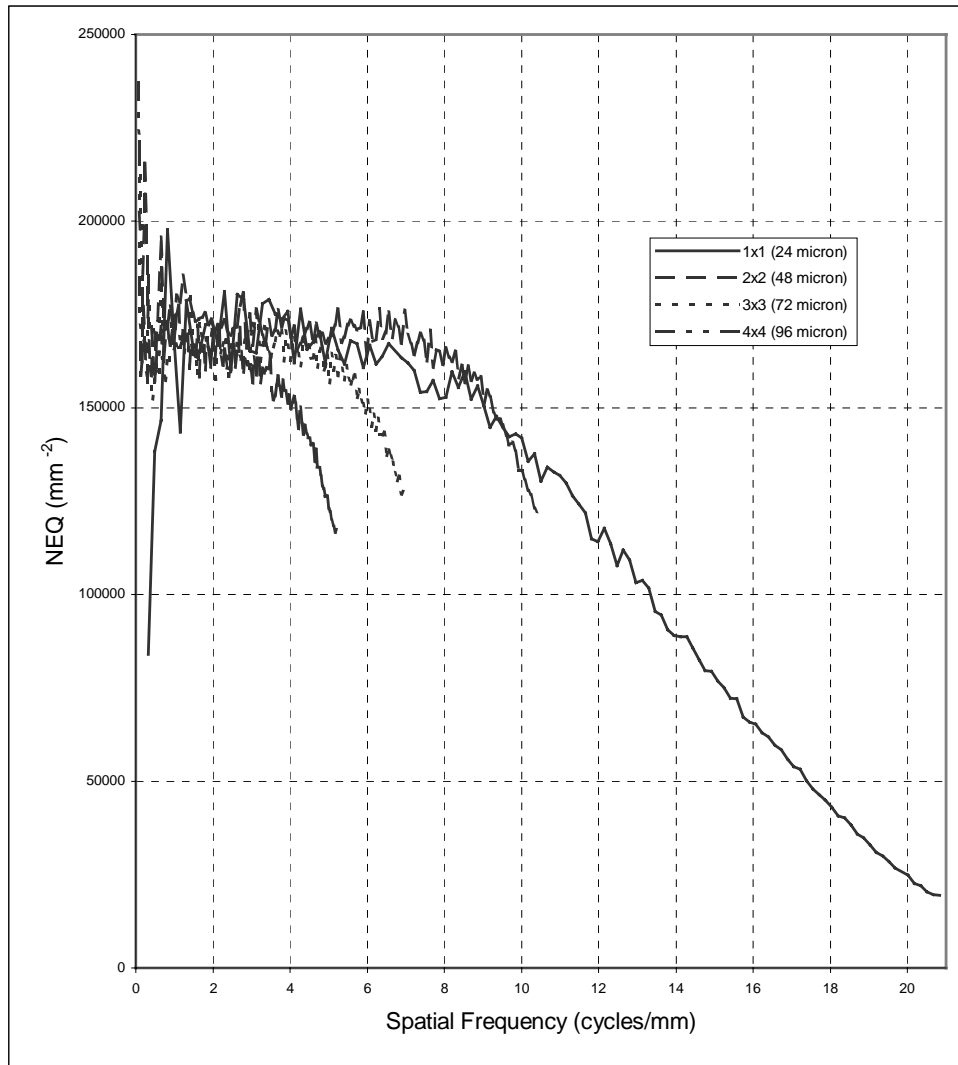


Figure 23. NEQ for CsI:Tl at 20 mAs (300170 quanta) for 24 micron, 48 micron, 72 micron and 96 micron pixels. The NEQ shows no significant difference as pixel size changes.

The NEQ for the CsI:Tl scintillator is consistently higher than for the Kodak MIN-R 2000™ scintillator. This is shown in Figure 24, NEQ at 20 mAs using 1 x 1 (24 micron) and 4 x 4 (96 micron) binning with both scintillators. Results followed the same trend at all exposures.

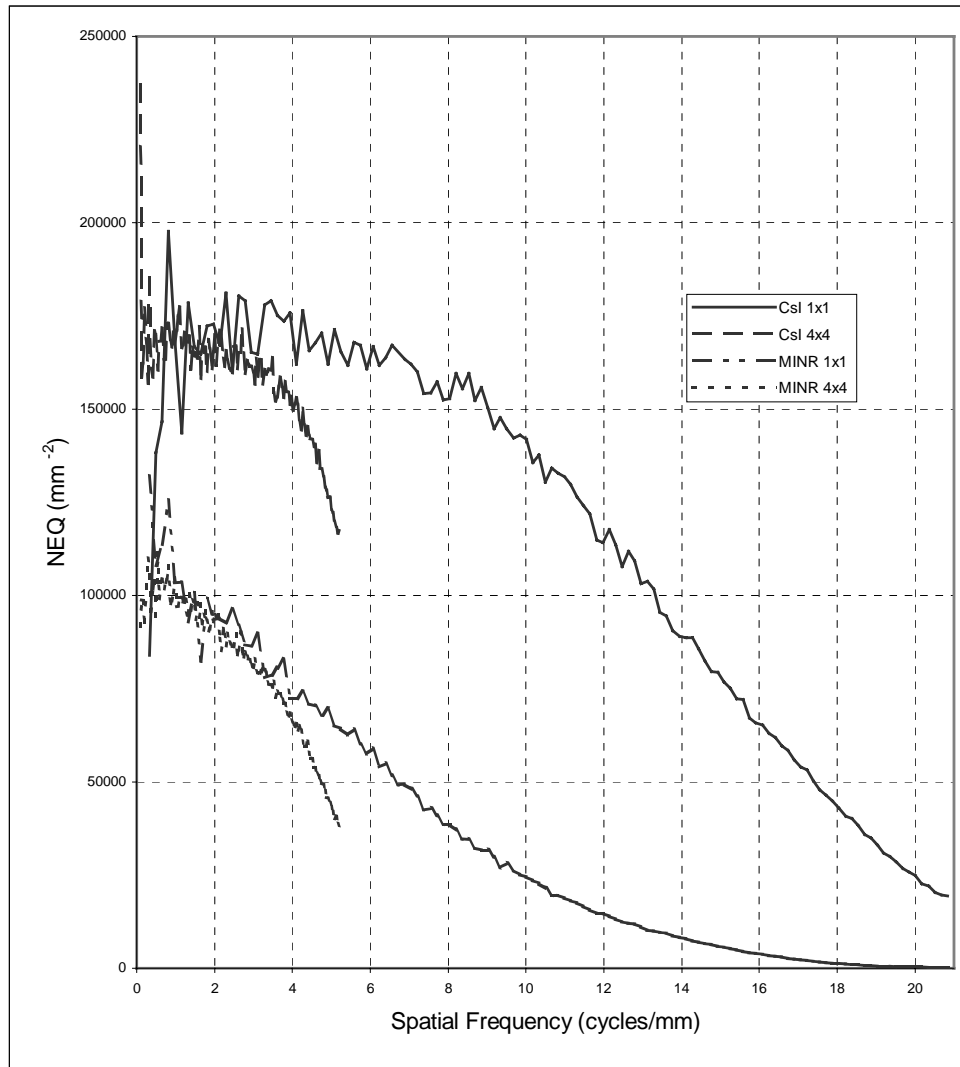


Figure 24. NEQ comparison of Kodak MIN-R 2000™ and CsI:Tl at 20 mAs for 1 x 1 (24 micron) and 4 x 4 (96 micron) binning. The NEQ for the CsI:Tl scintillator is consistently higher than for the Kodak MIN-R 2000™ scintillator.

As previously shown in Figures 16 and 17, there was no difference between hardware and software binning.

#### D. DQE

The photon flux incident on the detector was previously determined to be  $5.34 \times 10^4$  photons/mm<sup>2</sup>/mR. The exposure at the detector was determined by measuring the exposure at a distance of 45 cm and calculating the exposure at 65 cm. These were then used to calculate the DQE.

The DQE of the system at the four exposure levels without binning is shown in Figure 25 for Kodak MIN-R 2000™ and in Figure 26 for CsI:Tl. As shown, there is minimal influence by exposure on the DQE for either scintillator. DQE is influenced by scintillator, however, as shown in Figure 27, DQE without binning at 5 mAs and 20 mAs for both scintillators. This continues to hold true with hardware binning as shown in Appendix A, Figures A7, A8 and A9, DQE at 5 mAs and 20 mAs for both scintillators with 2 x 2 (48 micron), 3 x 3 (72 micron) and 4 x 4 (96 micron) binning, respectively.

As previously noted in Figures 16 and 17, the binning method does not change the results. Comparisons of hardware and software binning are shown in Appendix A, Figures A10, A11 and A12, which depict the DQE for hardware and software binning at 5 mAs for both scintillators at 2 x 2 (48 micron), 3 x 3 (72 micron) and 4 x 4 (96 micron) binning, respectively.

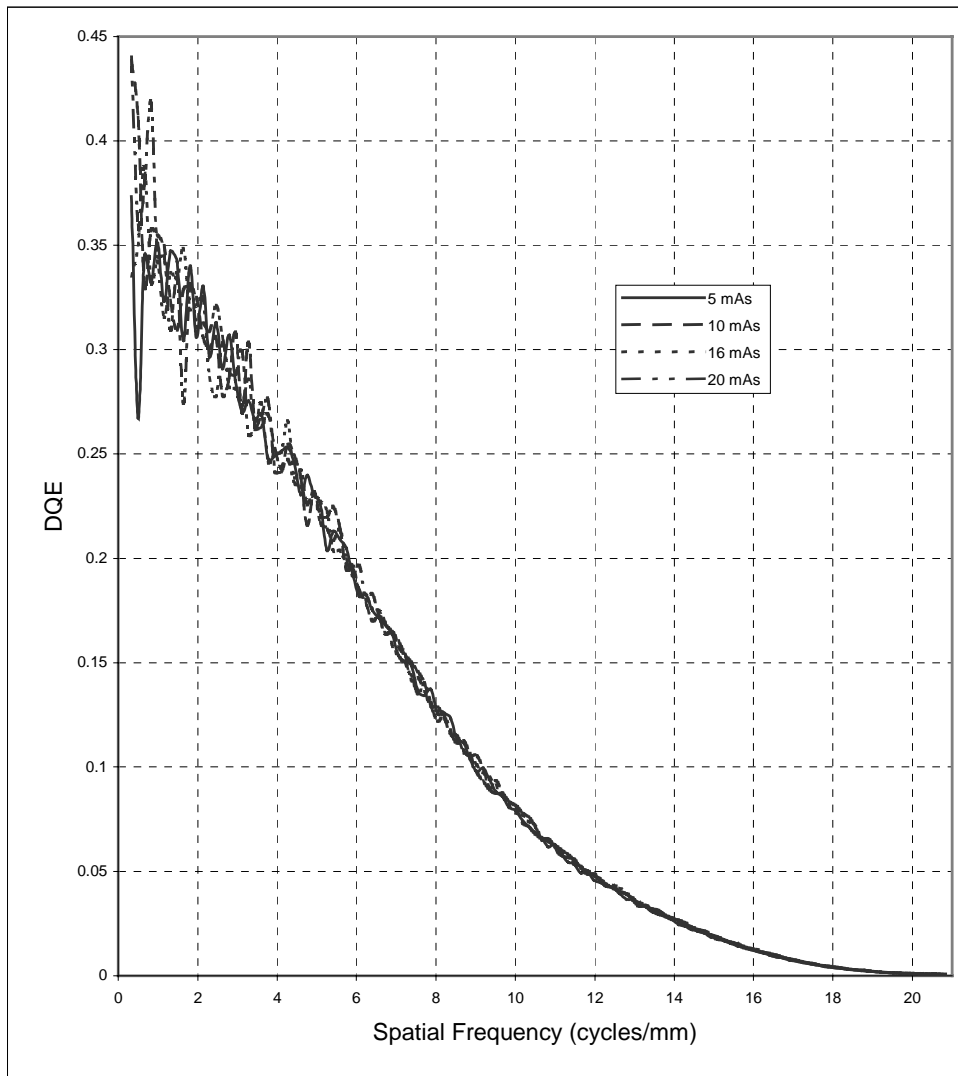


Figure 25. DQE for Kodak MIN-R 2000™ without binning at exposures of 5 mAs, 10 mAs, 16 mAs and 20 mAs. There is minimal influence of exposure on DQE.

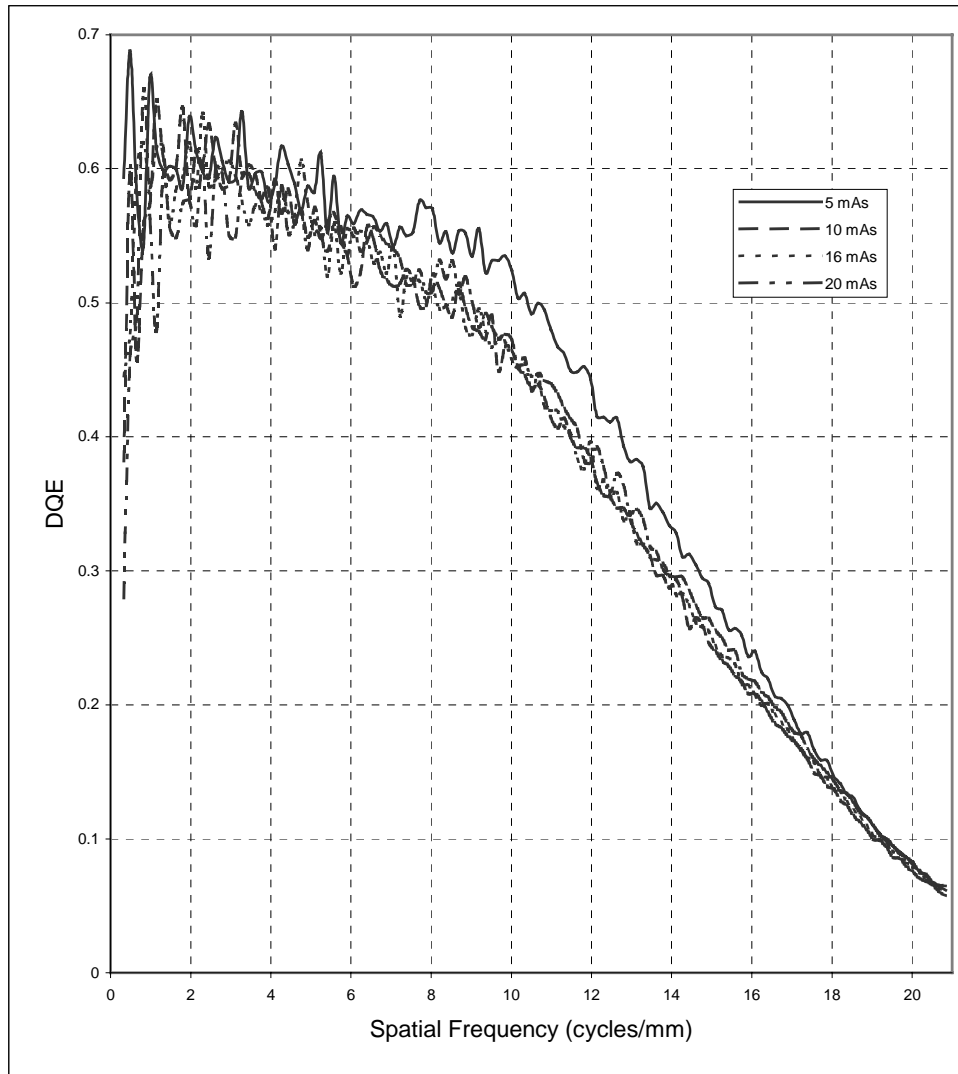


Figure 26. DQE for CsI:Tl without binning at 5 mAs, 10 mAs, 16 mAs and 20 mAs. As with Kodak MIN-R 2000™, there is minimal influence of exposure on DQE..

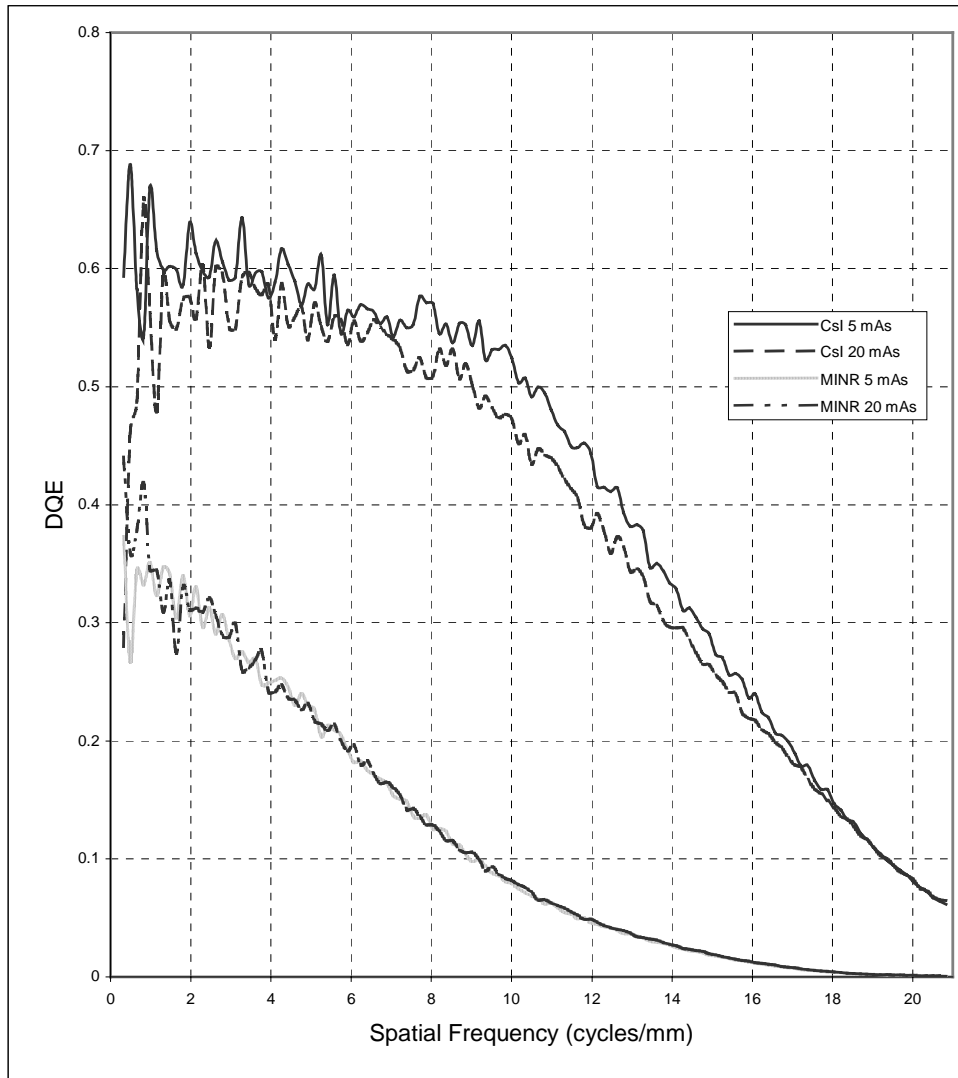


Figure 27. DQE comparison of Kodak MIN-R 2000™ and CsI:Tl without binning at exposures of 5 mAs and 20 mAs. Not only is the DQE of the CsI:Tl initially higher than that of the Kodak MIN-R 2000™, it remains relatively high and does not begin to drop off until it reaches 10 cycles/mm. While the DQE for the Kodak MIN-R 2000™ falls below 0.1 at 9.5 cycles/mm, the DQE for the CsI:Tl does not drop below 0.1 until 19 cycles/mm.



There is also minimal influence by pixel size on the DQE as shown in Figures 28 and 29, DQE at 5 mAs with and without binning for Kodak MIN-R 2000™ and CsI:TI respectively. This holds true as exposure increases as shown in Appendix A, Figures A13 and A14, 10 mAs; A15 and A16, 16 mAs and A17 and A18, 20 mAs.

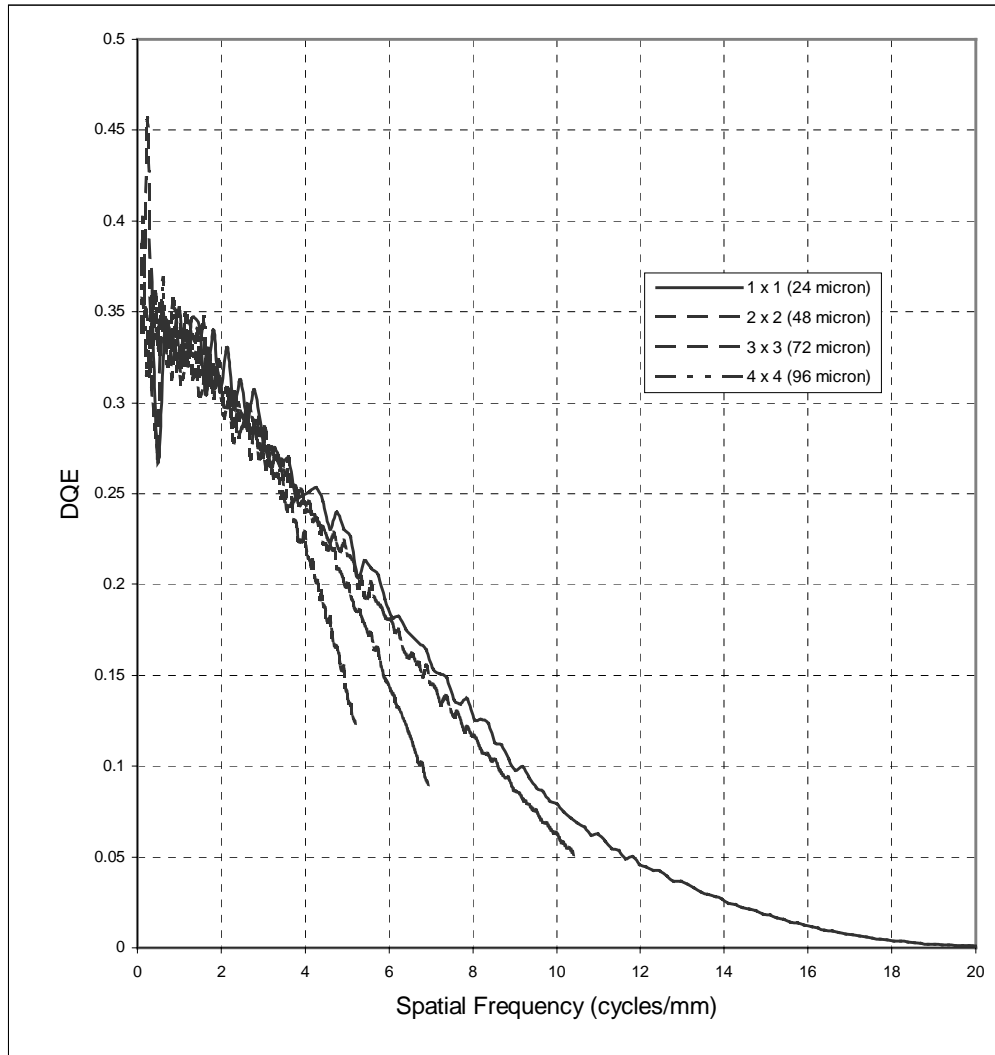


Figure 28. DQE for Kodak MIN-R 2000™ with and without binning at 5 mAs. Other than limiting spatial resolution, pixel size does not influence the DQE in this system.

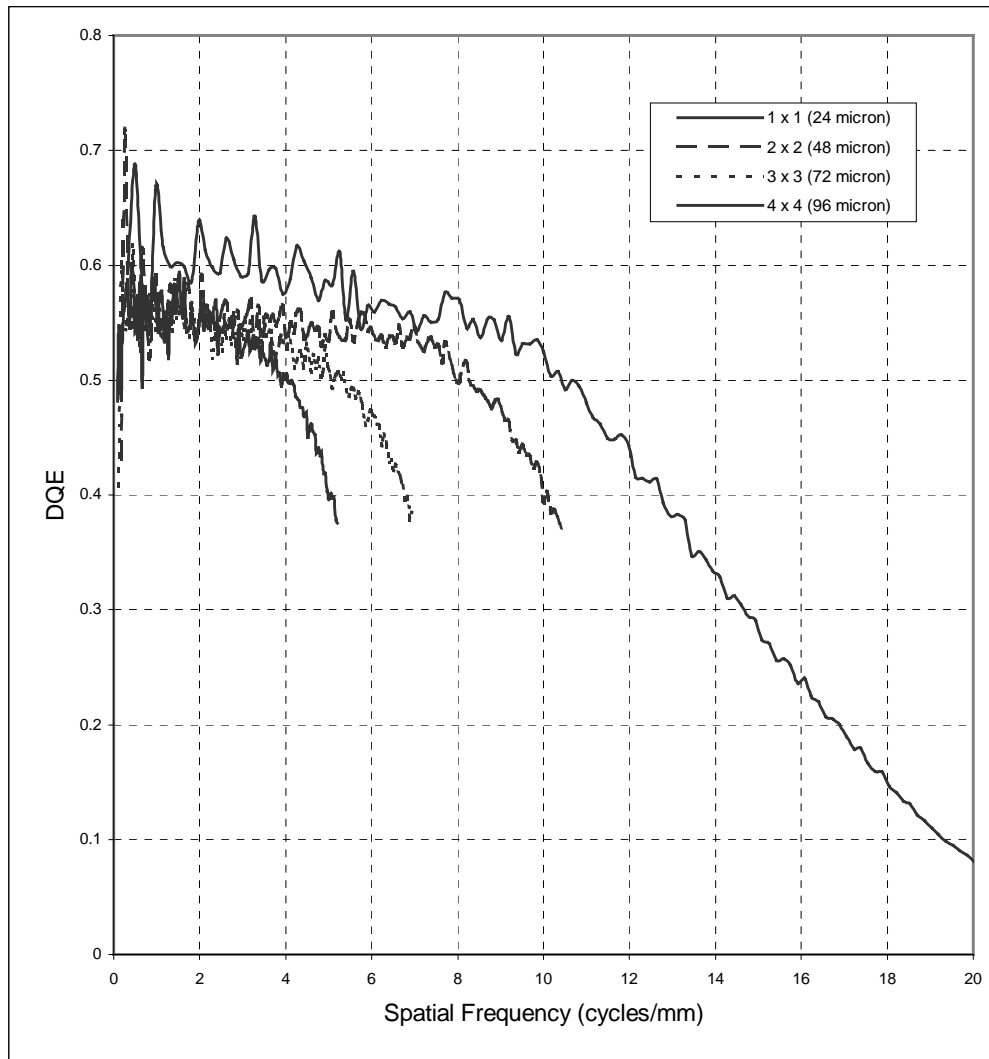


Figure 29. DQE for CsI:Tl with and without binning at 5 mAs. Other than limiting spatial resolution, pixel size does not influence the DQE in this system.

In each of these figures, only hardware binning is shown since software binning was found to be identical.

For comparison purposes, reference is made to the zero frequency value for DQE. This value is estimated from the DQE curves by curve fitting to a spatial frequency of 0. In this study the zero frequency value for the Kodak MIN-R 2000™ scintillator is

approximately 0.35. The zero frequency value for the CsI:Tl scintillator is approximately 0.6. For a clinical prototype, full breast digital mammography system the zero frequency DQE at comparable exposures was approximately 0.48<sup>16</sup>.

#### IV. DISCUSSION

As shown in Figure 8, the resolution characteristics of the CsI:Tl scintillator are comparable to the Kodak MIN-R 2000™ scintillator at low frequencies, but exhibits a higher MTF above about 3 cycles/mm. This indicates that the CsI:Tl scintillator has a greater ability to reproduce the higher frequencies that represent smaller objects and sharper edges. This is particularly important in applications such as mammography where small microcalcifications and the shape of masses provide early evidence of cancer.

The data also shows that there is a small increase in the MTF as the pixel size decreases. This difference is expected since larger pixels cannot adequately sample higher frequencies.

As shown in Figures 12 and 13, the normalized NPS for the Kodak MIN-R 2000™ scintillator is higher than that for the CsI:Tl scintillator. This is noted particularly at low frequencies and may be due to the columnar structure of the CsI:Tl scintillator.

This is also reflected in the NEQ and DQE results showing that the CsI:Tl scintillator produced not only higher NEQ and DQE but maintained those high levels to a higher frequency than the Kodak MIN-R 2000™ scintillator. Figure 30 shows the NEQ comparison and Figure 33 shows the DQE comparison. In both cases the Kodak MIN-R 2000™ scintillator curve falls off sharply as frequency increases while the

CsI:Tl scintillator curve stays very close to the zero frequency value almost halfway to the limiting frequency.

The NEQ results showed an increase with increased exposure, as expected since increased exposure provides increased signal. The results also showed no significant difference as pixel size decreased. This indicates that noise in the system was dominated by the x-ray photon (quantum) noise.

The results showed no significant difference in DQE with either exposure or pixel size. This also indicates that the noise in the system is predominantly x-ray photon noise. It also indicates that exposure need not be increased to improve image quality and that decreasing pixel size does not necessarily degrade image quality.

## V. CONCLUSION

By using a very low-noise CCD the DQE of a digital x-ray imaging system can be maintained while pixel size is reduced. Combined with a properly designed scintillator resolution can be substantially improved without compromising image quality.

Where maximum resolution is not required, hardware or software binning can be used to increase pixel size. Hardware and software binning were shown to be identical with no degradation of image quality.

While gadolinium oxysulfide screens, such as Kodak MIN-R 2000™, are well suited for use with film, they do not perform as well as a scintillator designed for use with a CCD. For the system represented in Figure 28, the DQE falls to 0.1 at about 9 cycles/mm for both the 48 micron pixel (2 x 2 binning) and the 24 micron pixel (no binning). Using 0.1 as a lower limit for DQE, and maintaining the exposure at 5 mAs, this system with a 48 micron pixel will perform as well as this system with a 24 micron pixel, i.e. smaller objects and sharper edges will not be imaged any more clearly with this system with a 24 micron pixel.

The columnar structure of CsI:Tl appears to be far superior to the granular structure of gadolinium oxysulfide. The DQE using the CsI:Tl scintillator achieved a higher initial DQE and maintained a relatively high DQE to a higher frequency than did the

DQE using Kodak MIN-R 2000™. For the system represented in Figure 29 the DQE, at an exposure of 5 mAs, for the 96 micron pixel (4 x 4 binning), the 72 micron pixel (3 x 3 binning) and the 48 micron pixel (2 x 2 binning) is greater than 0.35 when the Nyquist limits are reached. For the 24 micron pixel (no binning) the DQE falls to 0.1 at about 19 cycles/mm. In this system, at an exposure of 5 mAs, resolution will be increased by reducing the pixel size to 24 microns. Compared with the above Kodak MIN-R 2000™ scintillator, this system will have more than twice the resolution and would have slightly better resolution than current screen-film mammography systems that operate in the 16 to 18 cycles/mm range.

## REFERENCES

1. Bunch P, The effects of reduced film granularity on mammographic image quality. *Opt. Soc. Int. Eng. (SPIE)*, 3032, 302-317 (1997).
2. Yoshida H, Doi K, Nishikawa RM, et al: An improved computer-assisted diagnostic scheme using wavelet transform for detecting clustered microcalcifications in digital mammograms. *Acad Radiol* 3(8): 621-627, 1996.
3. Anastasio MA, Yoshida H, Nagel R, et al: A genetic algorithm-based method for optimizing the performance of a computer-aided diagnosis scheme for detection of clustered microcalcifications in mammograms. *Med Phys* 25(9): 1613-1620, 1998.
4. Suryanarayanan S, Karellas A, Vedantham S, et al: Comparison of Tomosynthesis Methods Used with Digital Mammography. *Acad Radiol* 2000; 7:1085-1097 (2000).
5. Chakraborty DP and Barnes GT, An energy sensitive cassette for dual-energy mammography, *Med. Phys.* 16(1), 7-13 (1989).
6. Flanagan FL, Murray JG, Gilligan P, Stack JP and Ennis JT, Digital subtraction in Gd-DTPA enhanced imaging of the breast, *Clin. Radiol.* 50(12), 848-854 (1995).
7. Hillen W, Schiebel U, and Zaengel T, Imaging performance of a storage phosphor system, *Med. Phys.* 14(5), 744-751 (1987).
8. Hillen W, Schiebel U, and Zaengel T: A selenium-based detector system for digital slot-radiography. *SPIE Vol. 914 Medical Imaging II* 253-261, 1988
9. Neitzel U, Maack I, Gunther-Kohfahl S: Image quality of a digital chest radiography system based on a selenium detector. *Med Phys* 21(4): 509-516, 1994.
10. Zhao W, Rowlands JA: Digital radiology using active matrix readout of amorphous selenium: Construction and evaluation of a prototype real-time detector. *Med Phys* 24(12): 1834-1843, 1997.
11. Antonuk LE, El-Mohri Y, Jee K, et al: Performance Evaluation of a Large Area, 97  $\mu\text{m}$  Pitch: Indirect Detection Active Matrix Flat-panel Imager (AMFPI) for Radiography and Fluoroscopy. *Radiology* 209(P): 357, 1998.



12. Siewerdsen JH, Antonuk LE, El-Mohri Y, et al: Empirical and theoretical investigation of the noise performance of indirect detection, active matrix flat-panel imagers (AMFPIs) for diagnostic radiology. *Med Phys* 24(1): 71-89, 1997.
13. Hejazi S, Trauernicht DP: System considerations in CCD-based x-ray imaging for digital chest radiography and digital mammography. *Med Phys* 24(2): 287-297, 1997.
14. Karellas, L.J. Harris, H. Liu, M.A. Davis and C.J. D'Orsi, "Charge-coupled device detector: Performance considerations and potential for small-field mammographic imaging applications," *Med. Phys.* 19(4), 1015-1023 (1992).
15. Bradford CD, Pepler WW and Dobbins JT, Performance characteristics of a Kodak computed radiography system, *Med. Phys.* 26(1), 27-37 (1999).
16. Vedantham S, Karellas A, Suryanarayanan S, et al: Full Breast Digital Mammographic Imaging with an Amorphous Silicon-based Flat Panel Detector: Physical Characteristics of a Clinical Prototype. *Med Phys* 27(3): 558-567, 2000.
17. Vedantham S, Karellas A, Suryanarayanan S, et al: Breast Imaging Using an Amorphous Silicon-based Full-Field Digital Mammographic System: Stability of a Clinical Prototype. *Journal of Digital Imaging*, Vol 13, No 4, 191-199, 2000.
18. Vedantham S, Karellas A, Suryanarayanan S, et al: Mammographic Imaging with a small format CCD-based digital cassette: Physical characteristics of a clinical system. *Med Phys* 27(8), 2000.
19. MacMahon H, Vyborny C, Powell G, et al: The effect of pixel size on the detection rate of early pulmonary sarcoidosis in digital chest radiographic systems. *Medical Imaging and Instrumentation* 14-20, 1984
20. Freedman M, Steller D, et al: Digital Mammography: Tradeoffs between 50 and 100 micron pixel size. *Proc. Of SPIE Vol 2432, Medical Imaging 1995*
21. Chan H-P, Helvie MA, Petrick N, et al: Digital Mammography: Observer Performance Study of the Effects of Pixel Size on Radiologists' Characterization of Malignant and Benign Microcalcifications. *Proc. Of SPIE Vol 3659, Medical Imaging 1999*
22. Lewin J M, Hendrick R E, D'Orsi CJ, et al: Comparison of Full-Field Digital Mammography with Screen-Film Mammography for Cancer Detection: Results of 4,945 Paired Examinations. *Radiology* 2001; 218:873-880

23. Fujita H, Tsai DY, Itoh T, Doi K, Morishita J, Ueda K, and Ohtsuka A, A simple method for determining the modulation transfer function in digital radiography, *IEEE Trans. Med. Imaging* 11, 34-39 (1992)
24. Dobbins JT, Ergun DL, Rutz L, Hinshaw DA, Blume H, and Clark DC,  $DQE(f)$  of four generations of computed radiography acquisition devices, *Med. Phys.* 22, 1581-1593 (1995)
25. Dobbins JT, Effects of undersampling on the proper interpretation of modulation transfer function, noise power spectra, and noise equivalent quanta of digital imaging systems, *Med. Phys.* 22, 171-181 (1995)
26. Dainty JC and Shaw R, *Image Science* (Academic, New York, 1974)

## Appendix A – Supplemental Figures

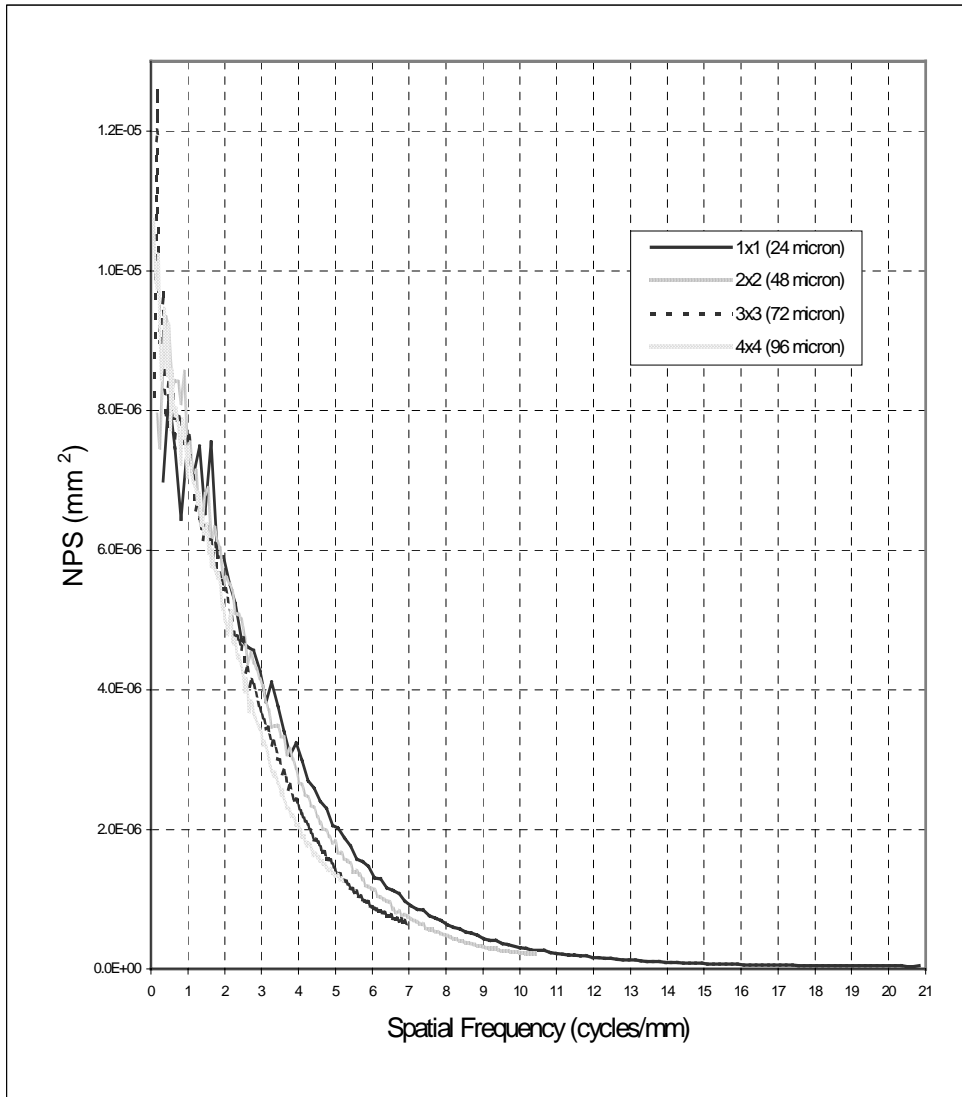


Figure A1. NPS for Kodak MIN-R 2000™ at 20 mAs for 24 micron, 48 micron, 72 micron and 96 micron pixel sizes. NPS decreases slightly as pixel size increases even at higher exposures. This reflects the relative increase in signal as pixel size increases while there is no significant improvement in noise.

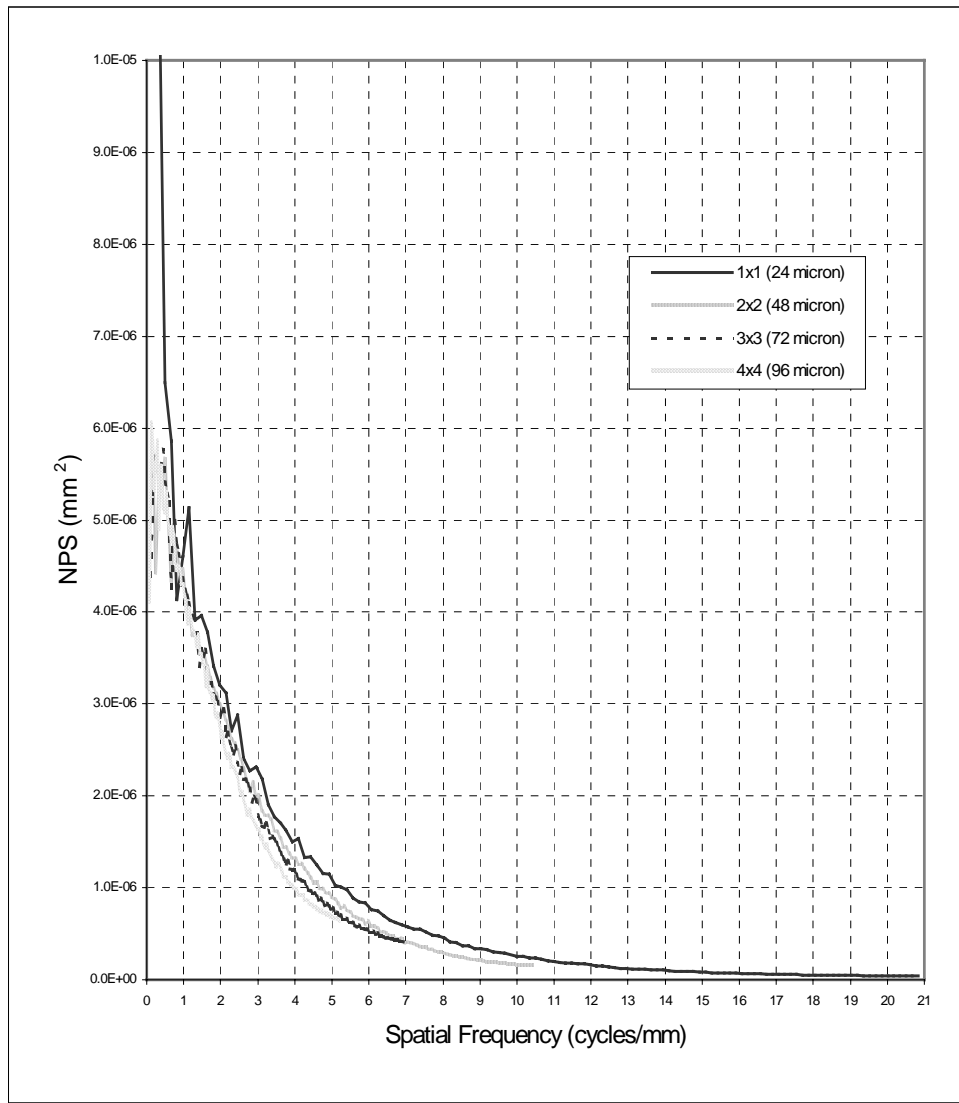


Figure A2. NPS for CsI:Tl at 20 mAs for 24 micron, 48 micron, 72 micron and 96 micron pixel sizes. As in the case of Kodak MIN-R 2000™, NPS decreases slightly as pixel size increases even at higher exposures. This reflects the relative increase in signal as pixel size increases while there is no significant improvement in noise.

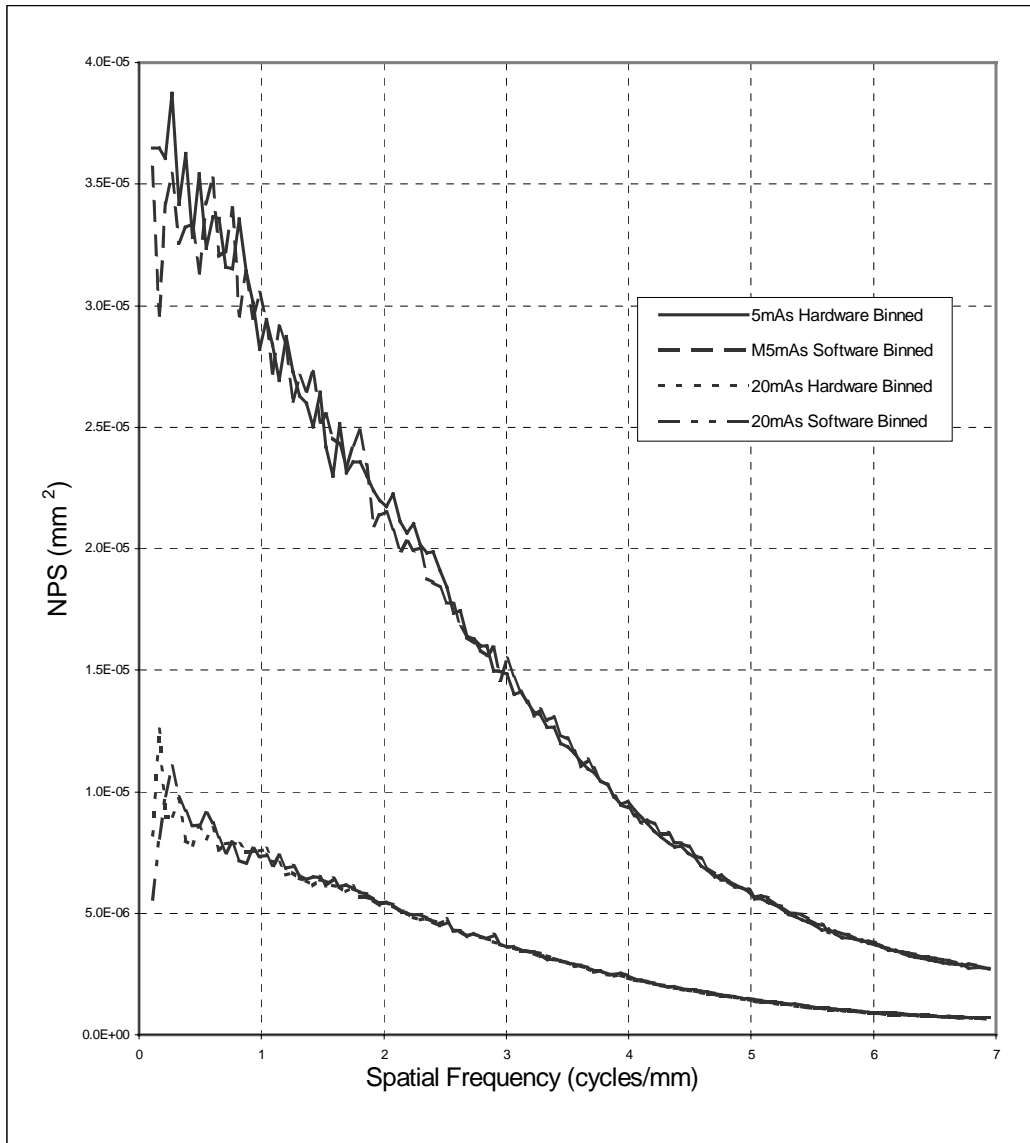


Figure A3. Hardware vs Software 3 x 3 Binning (72 micron), NPS for Kodak MIN-R 2000™ at 5 mAs and 20 mAs. No significant difference is noted between hardware and software binning.

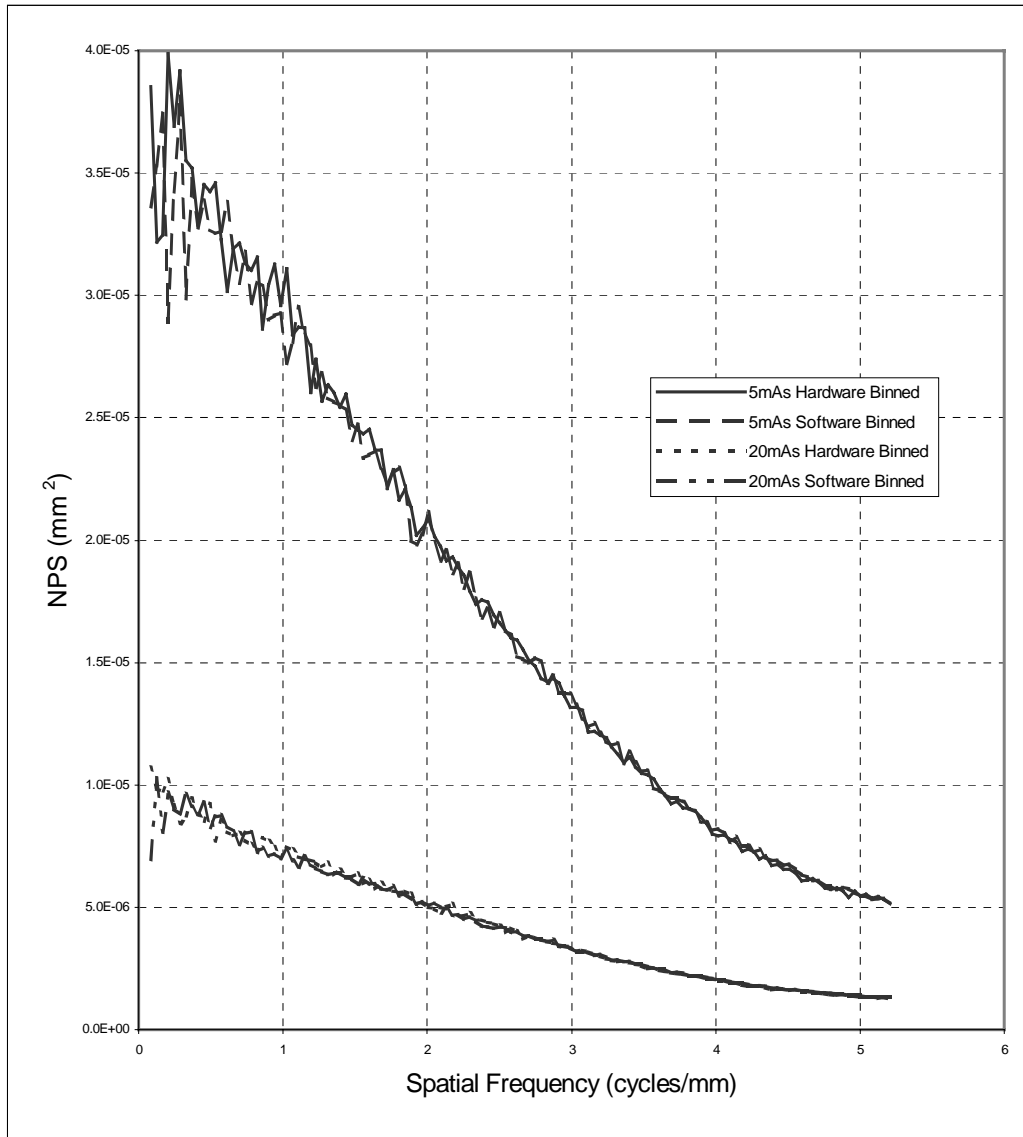


Figure A4. Hardware vs Software 4 x 4 Binning (96 micron), NPS for Kodak MIN-R 2000™ at 5 mAs and 20 mAs. No significant difference is noted between hardware and software binning.

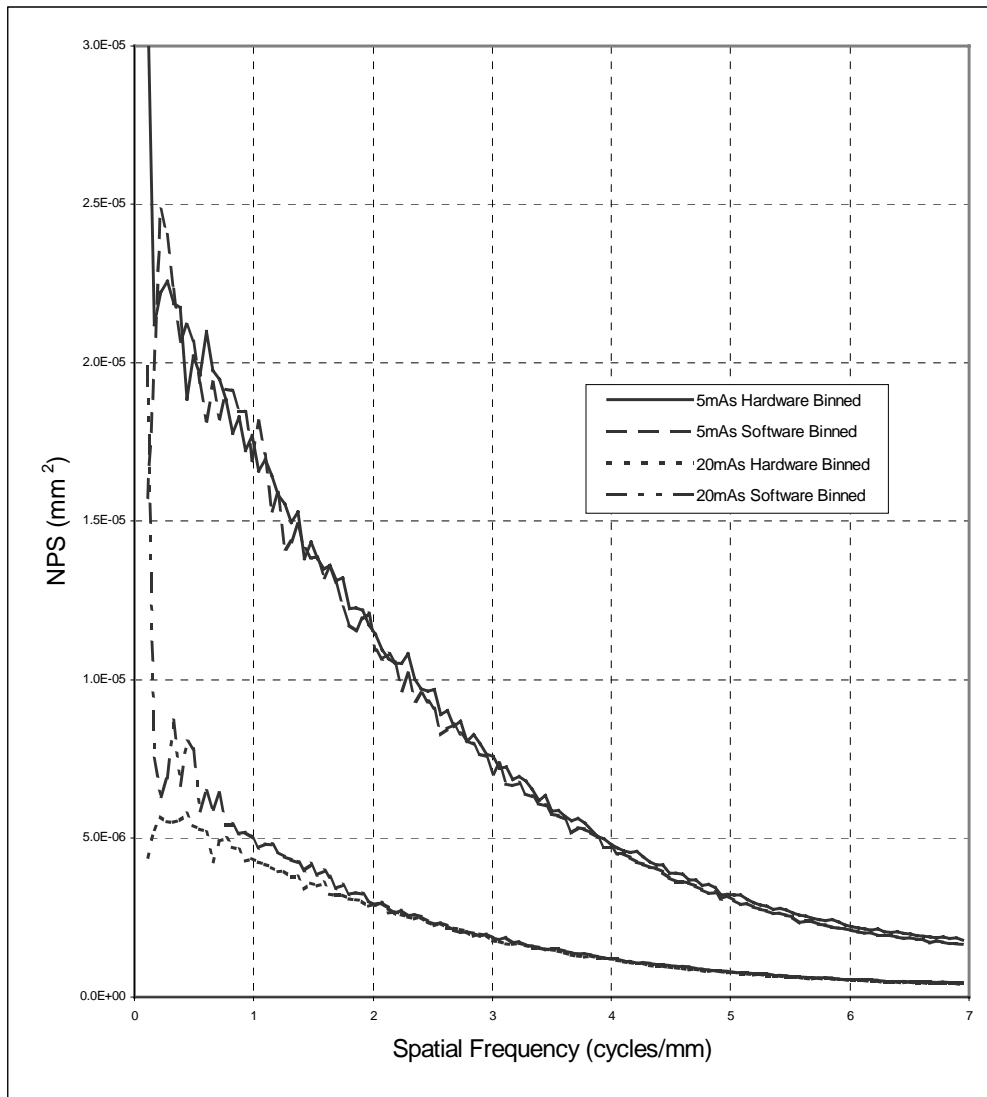


Figure A5. Hardware vs Software 3 x 3 Binning (72 micron), NPS for CsI:Tl at 5 mAs and 20 mAs. As with Kodak MIN-R 2000™, no significant difference is noted between hardware and software binning.

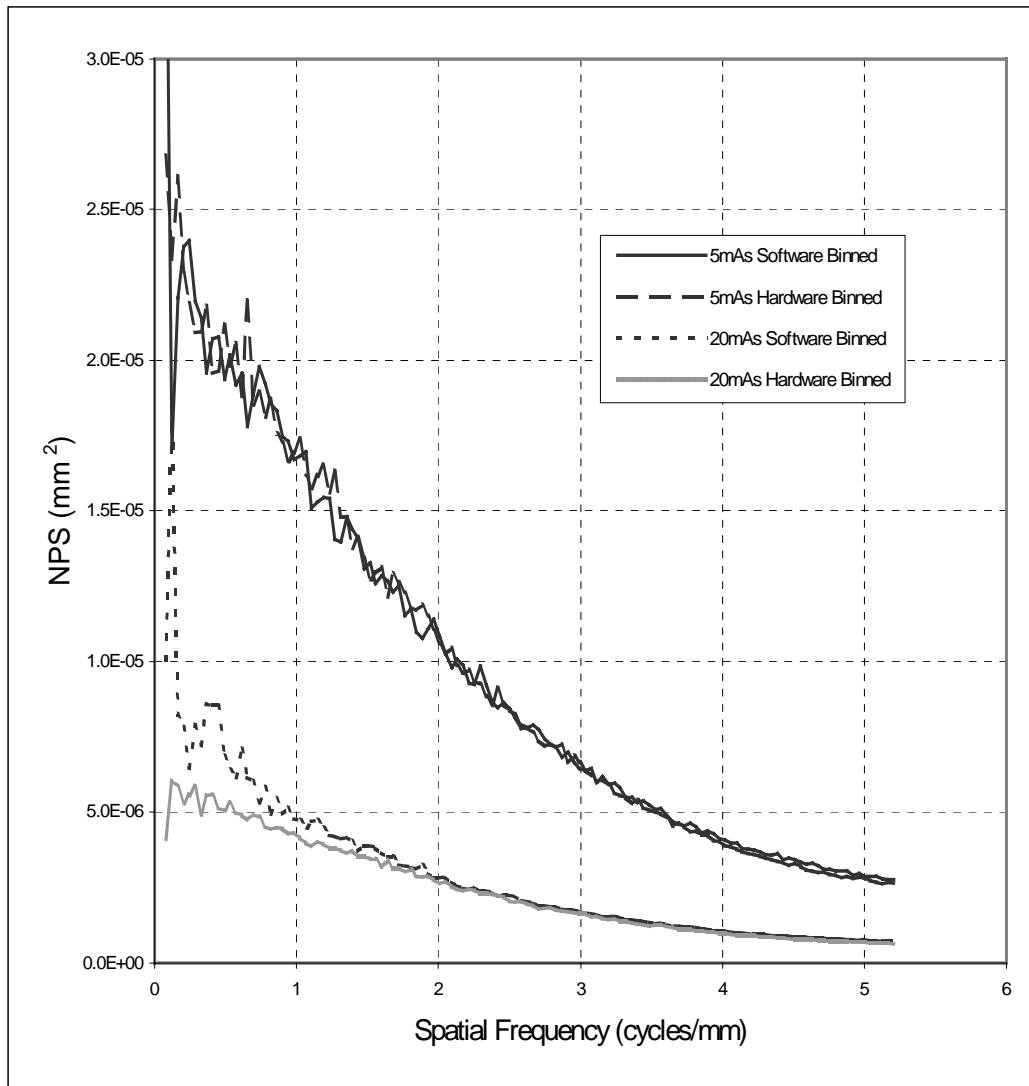


Figure A6. Hardware vs Software 4 x 4 Binning (96 micron), NPS for CsI:Tl at 5 mAs and 20 mAs. As with Kodak MIN-R 2000™, no significant difference is noted between hardware and software binning.



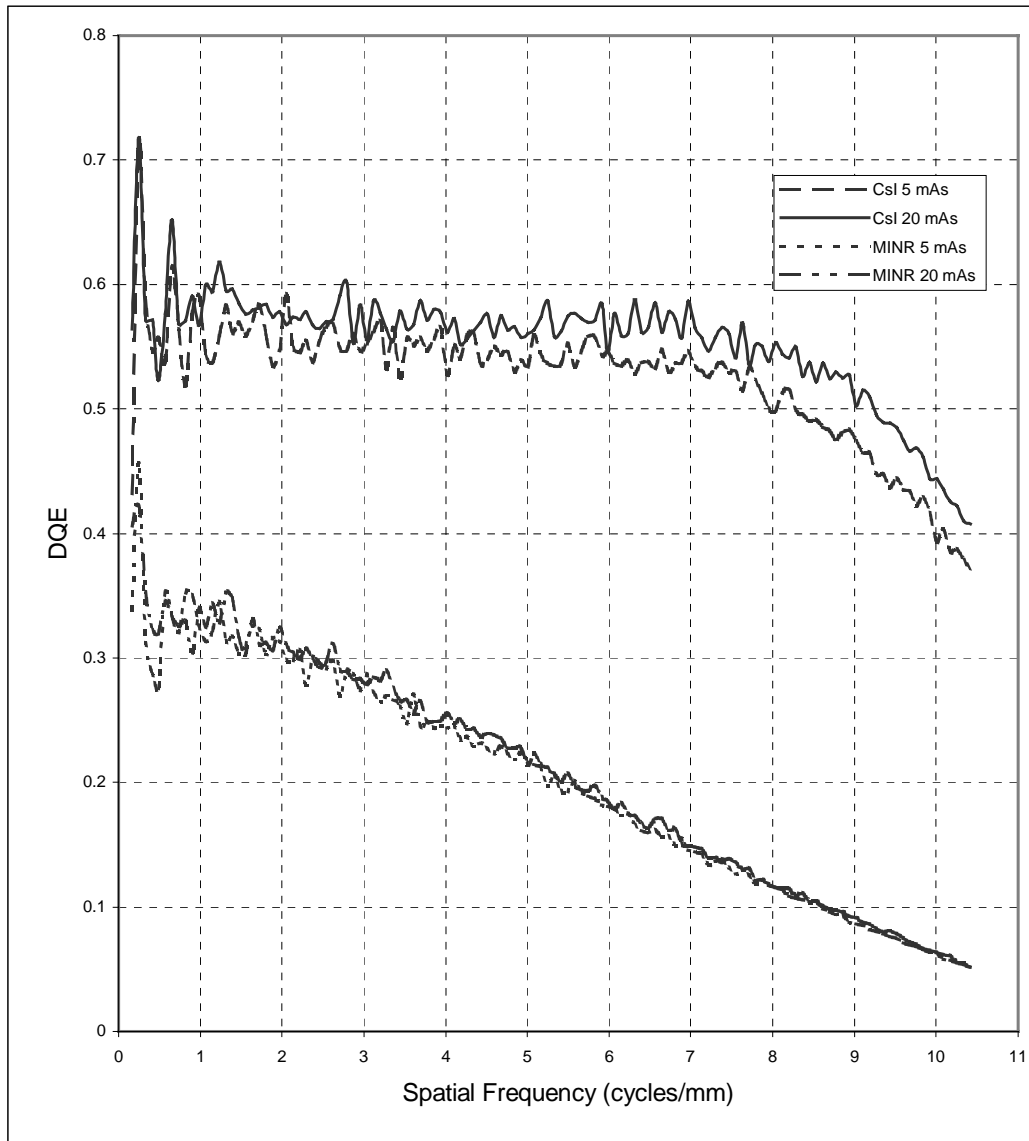


Figure A7. DQE comparison for Kodak MIN-R 2000™ and CsI:Tl with 2 x 2 binning (48 micron) at 5 mAs and 20 mAs. Not only is the DQE of the CsI:Tl initially higher than that of the Kodak MIN-R 2000™, it remains relatively high out to the Nyquist limit. The DQE for the Kodak MIN-R 2000™ falls below 0.1 at 8.5 cycles/mm, while the DQE for the CsI:Tl reaches the Nyquist limit before approaching 0.1.

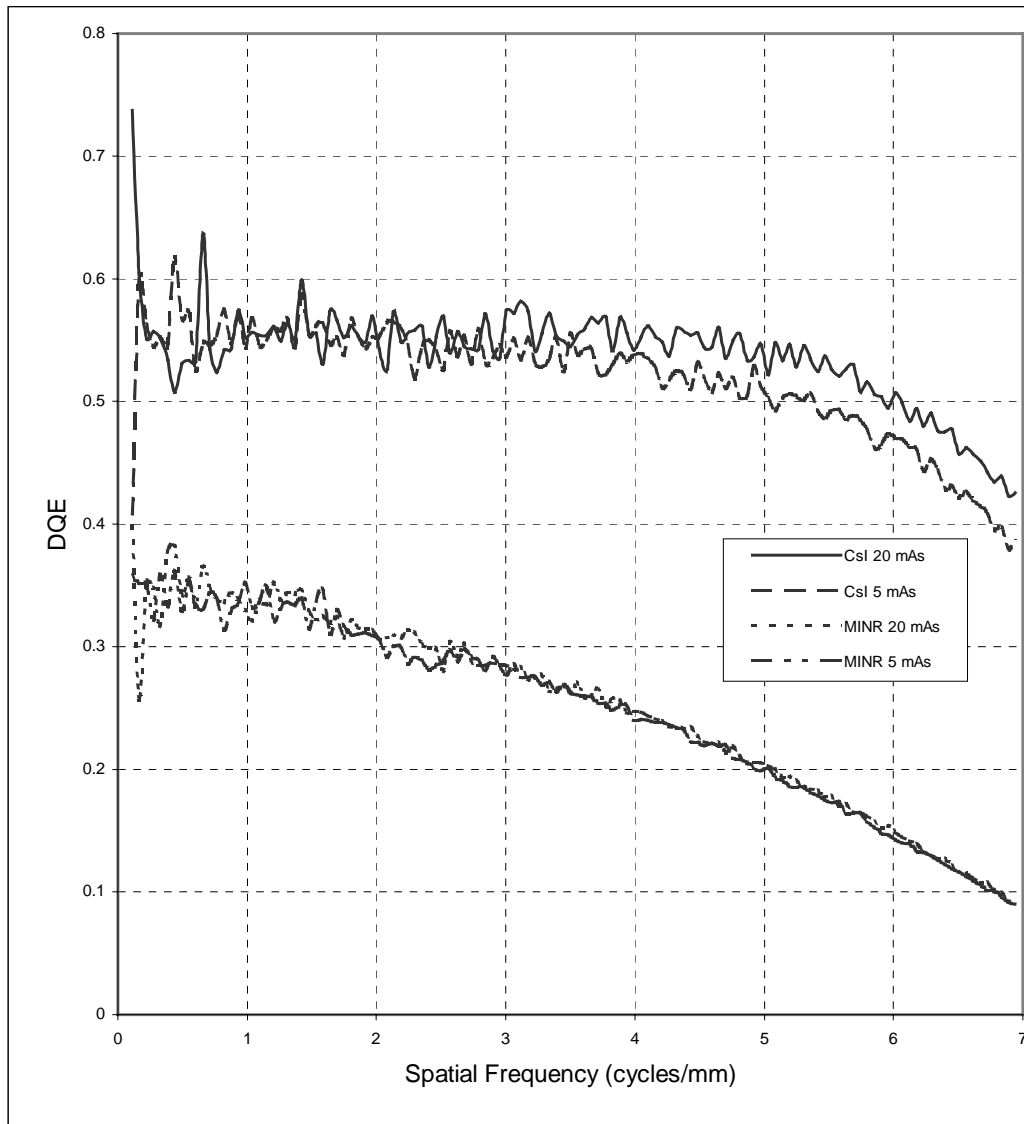


Figure A8. DQE comparison of Kodak MIN-R 2000™ and CsI:Tl with 3 x 3 binning at 5 mAs and 20 mas. Not only is the DQE of the CsI:Tl initially higher than that of the Kodak MIN-R 2000™, it remains relatively high out to the Nyquist limit. The DQE for the Kodak MIN-R 2000™ falls below 0.1 at 6.5 cycles/mm, while the DQE for the CsI:Tl reaches the Nyquist limit before approaching 0.1.

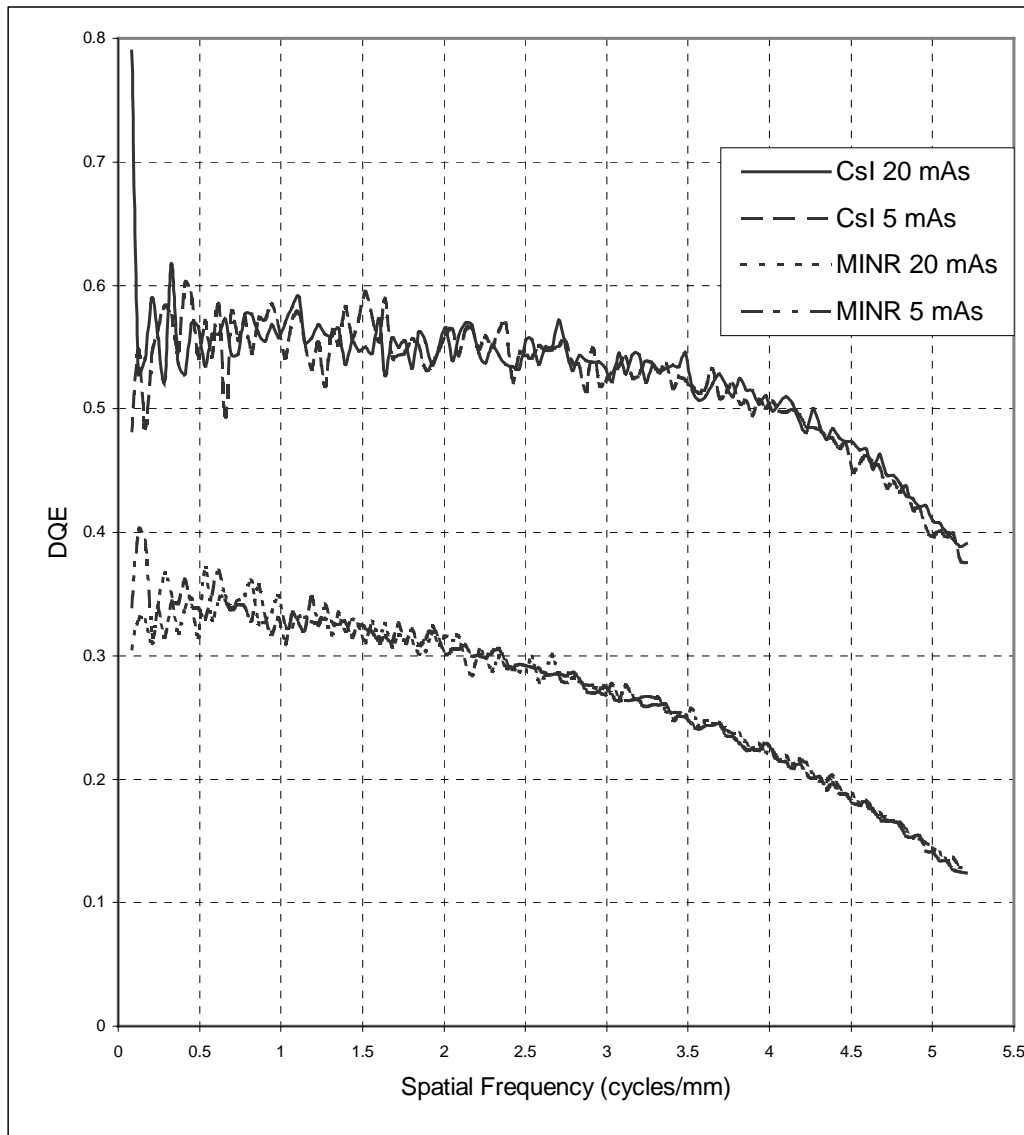


Figure A9. DQE comparison of Kodak MIN-R 2000™ and CsI:Tl with 4 x 4 binning at 5 mAs and 20 mAs. Not only is the DQE of the CsI:Tl initially higher than that of the Kodak MIN-R 2000™, it remains relatively high out to the Nyquist limit. The DQE for the Kodak MIN-R 2000™ approaches 0.1 at the Nyquist limit (5 cycles/mm), while the DQE for the CsI:Tl reaches the Nyquist limit before approaching 0.1.

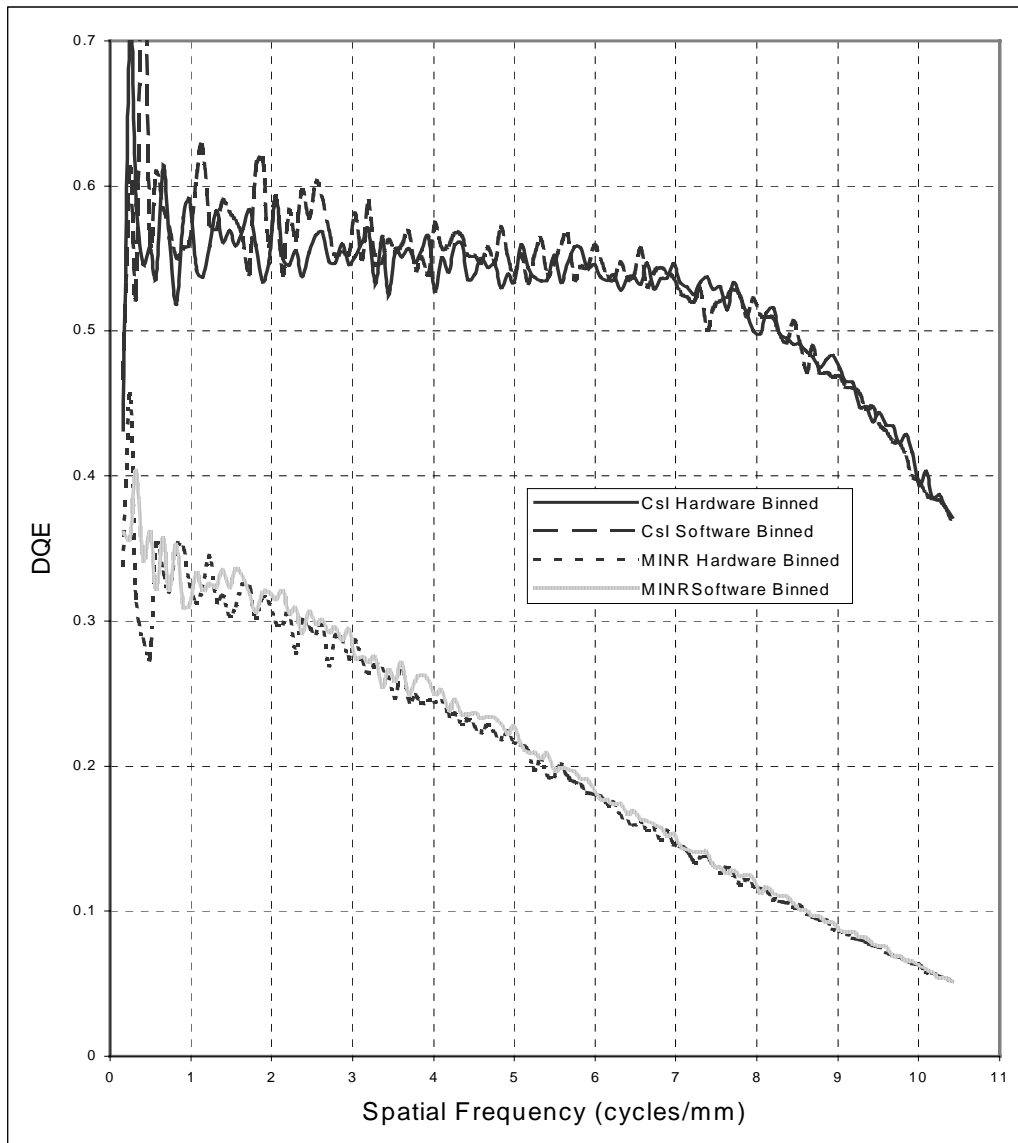


Figure A10. DQE comparison Kodak MIN-R 2000™ and CsI:Tl with 2 x 2 hardware and software binning at 5 mAs. No significant difference is noted between hardware and software binning.

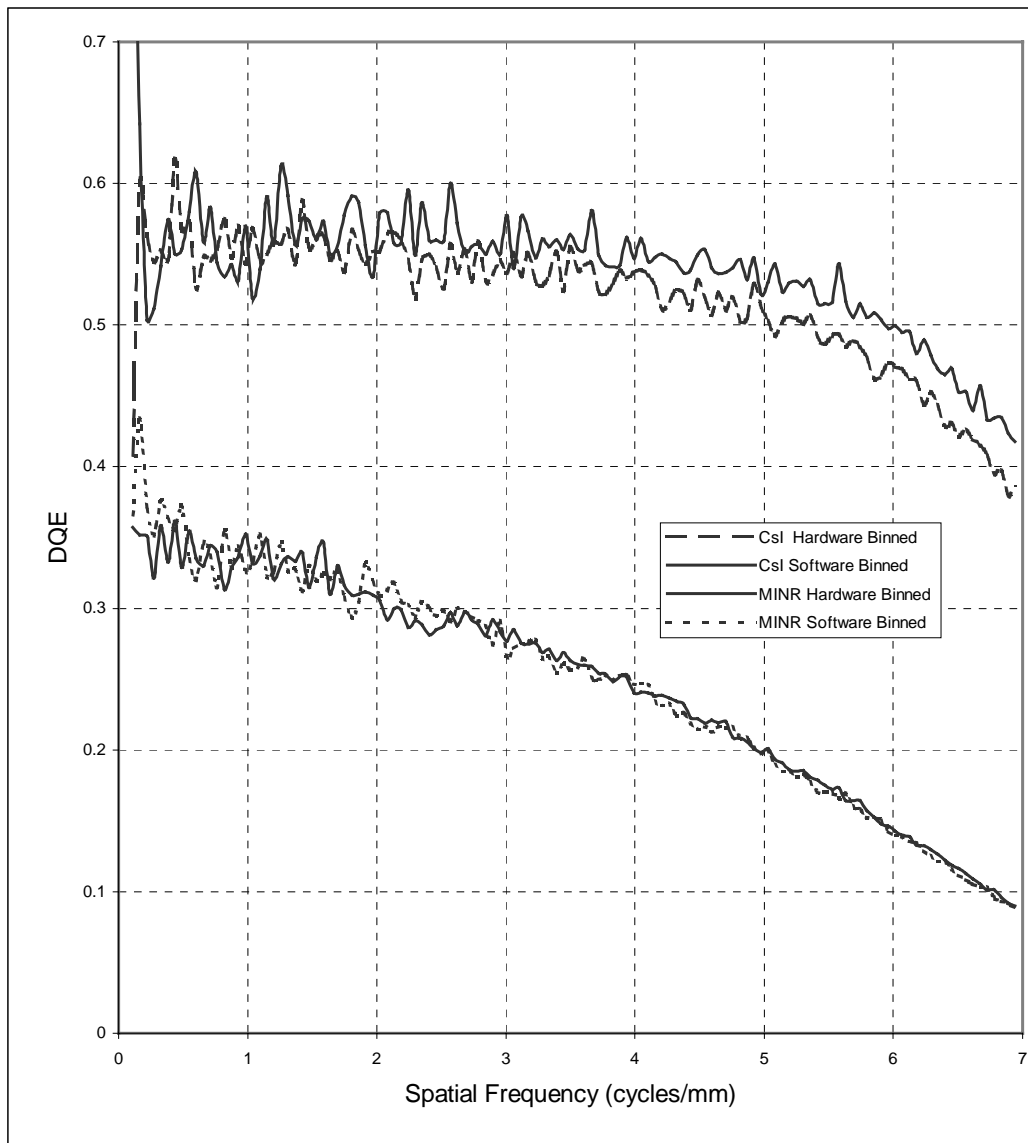


Figure A11. DQE comparison Kodak MIN-R 2000™ and CsI:Tl with 3 x 3 hardware and software binning at 5 mAs. No significant difference is noted between hardware and software binning.

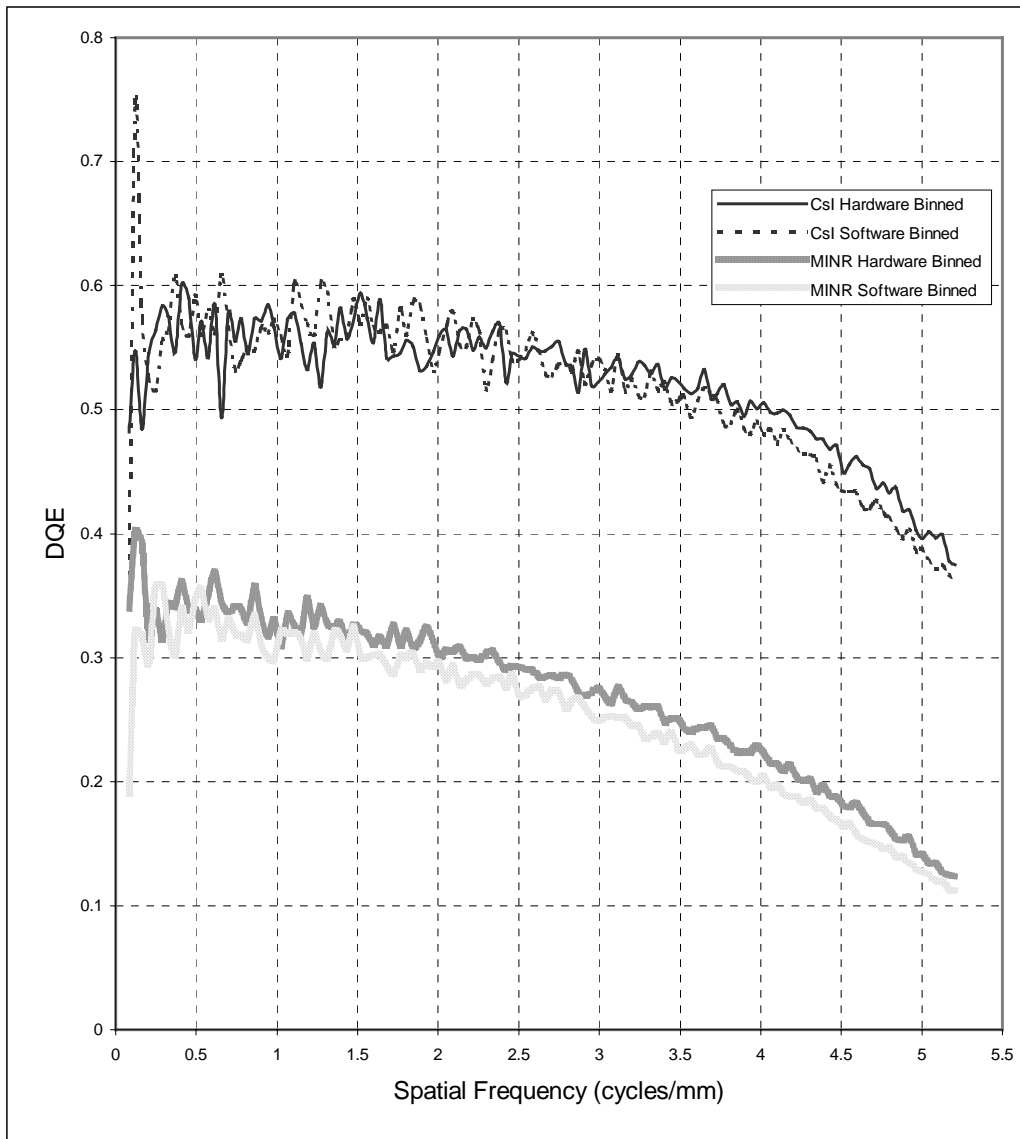


Figure A12. DQE comparison Kodak MIN-R 2000™ and CsI:Tl with 4 x 4 hardware and software binning at 5 mAs. No significant difference is noted between hardware and software binning.

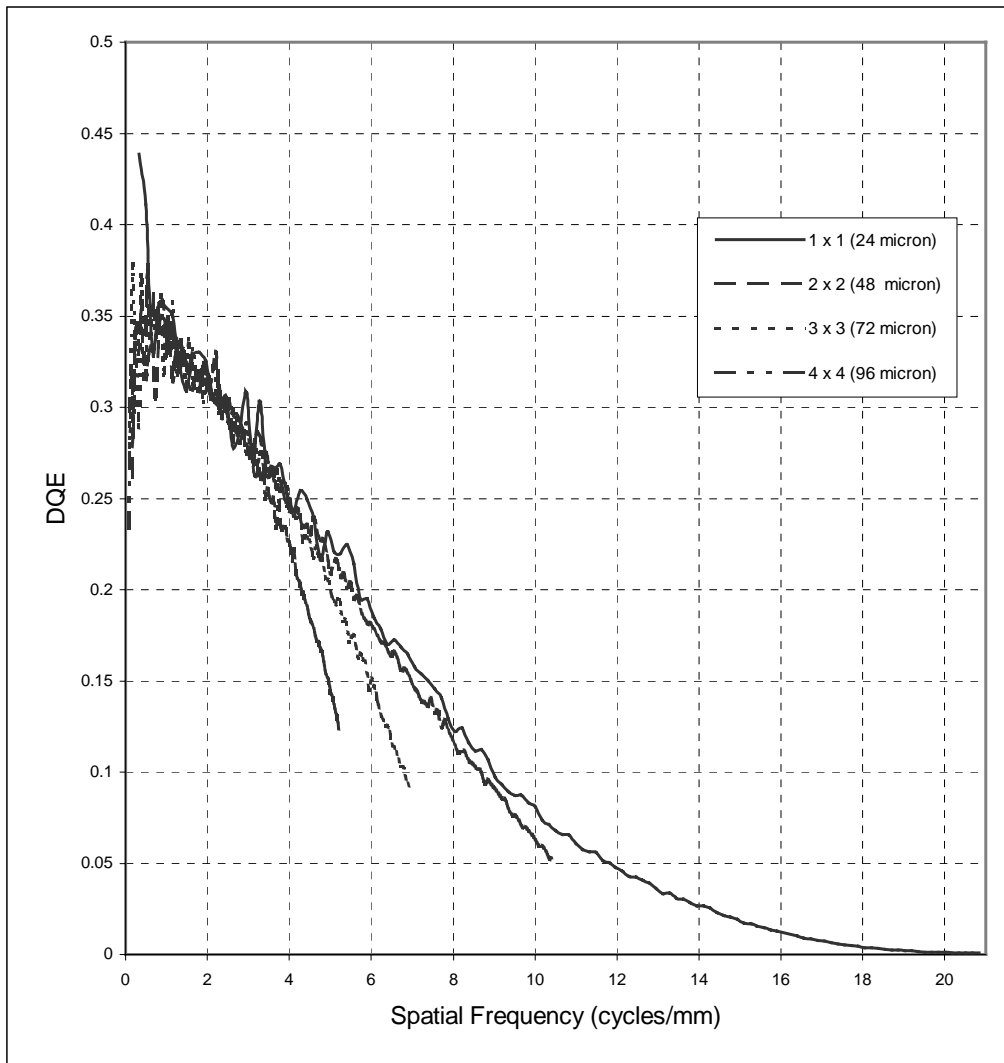


Figure A13. DQE for Kodak MIN-R 2000™ with and without binning at 10 mAs. Other than limiting spatial resolution, pixel size does not influence the DQE in this system.

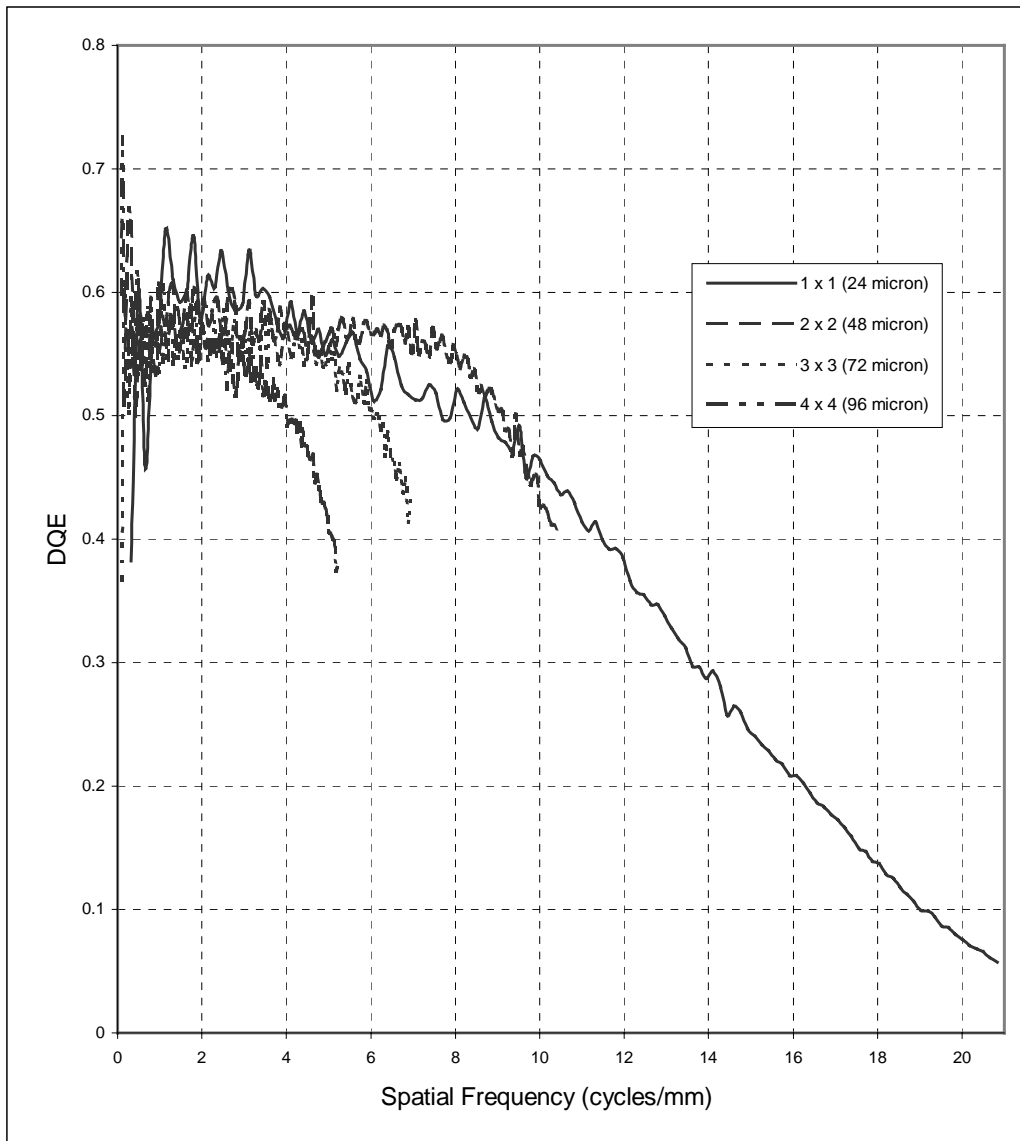


Figure A14. DQE for CsI:Tl with and without binning at 10 mAs. Other than limiting spatial resolution, pixel size does not influence the DQE in this system.



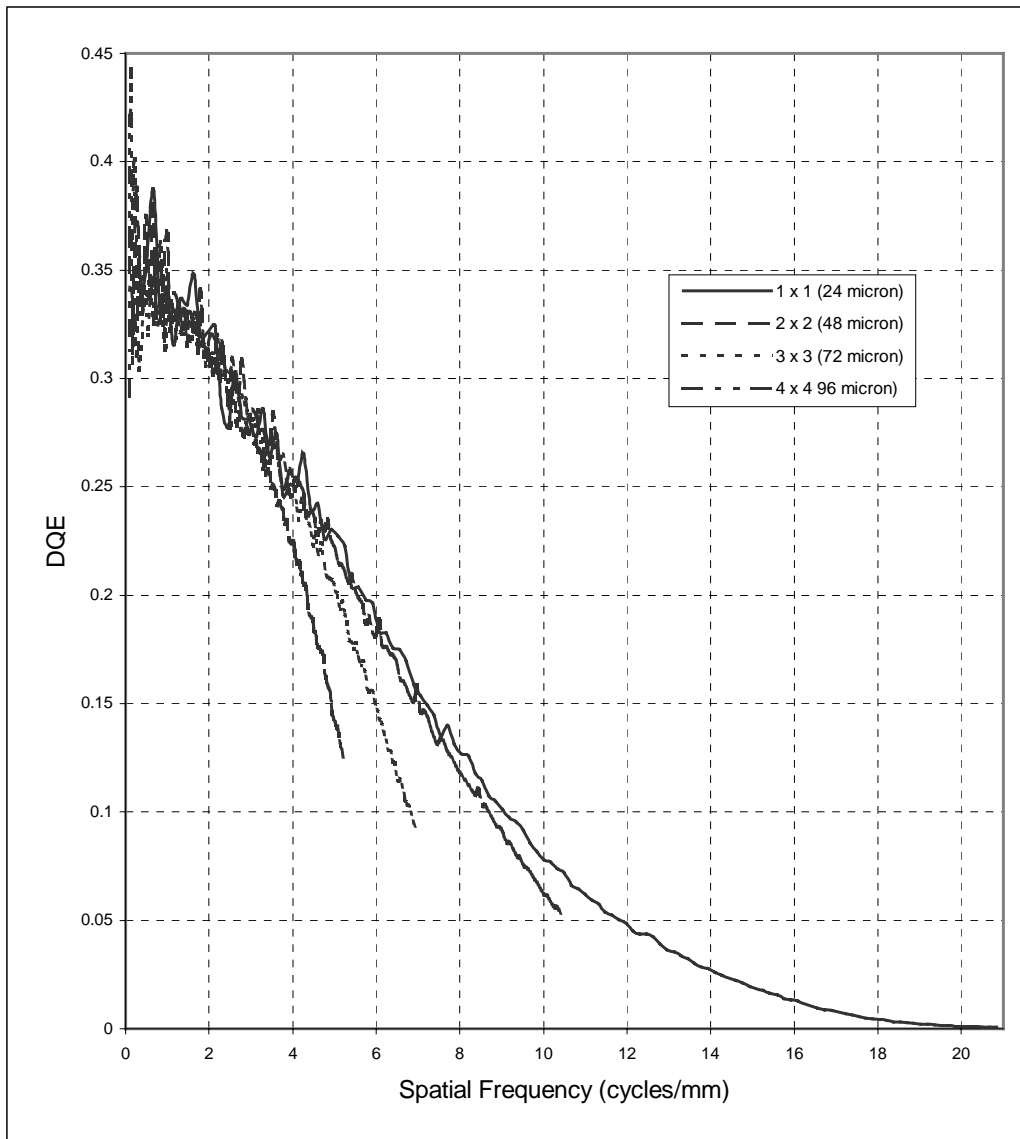


Figure A15. DQE for Kodak MIN-R 2000™ with and without binning at 16 mAs. Other than limiting spatial resolution, pixel size does not influence the DQE in this system.

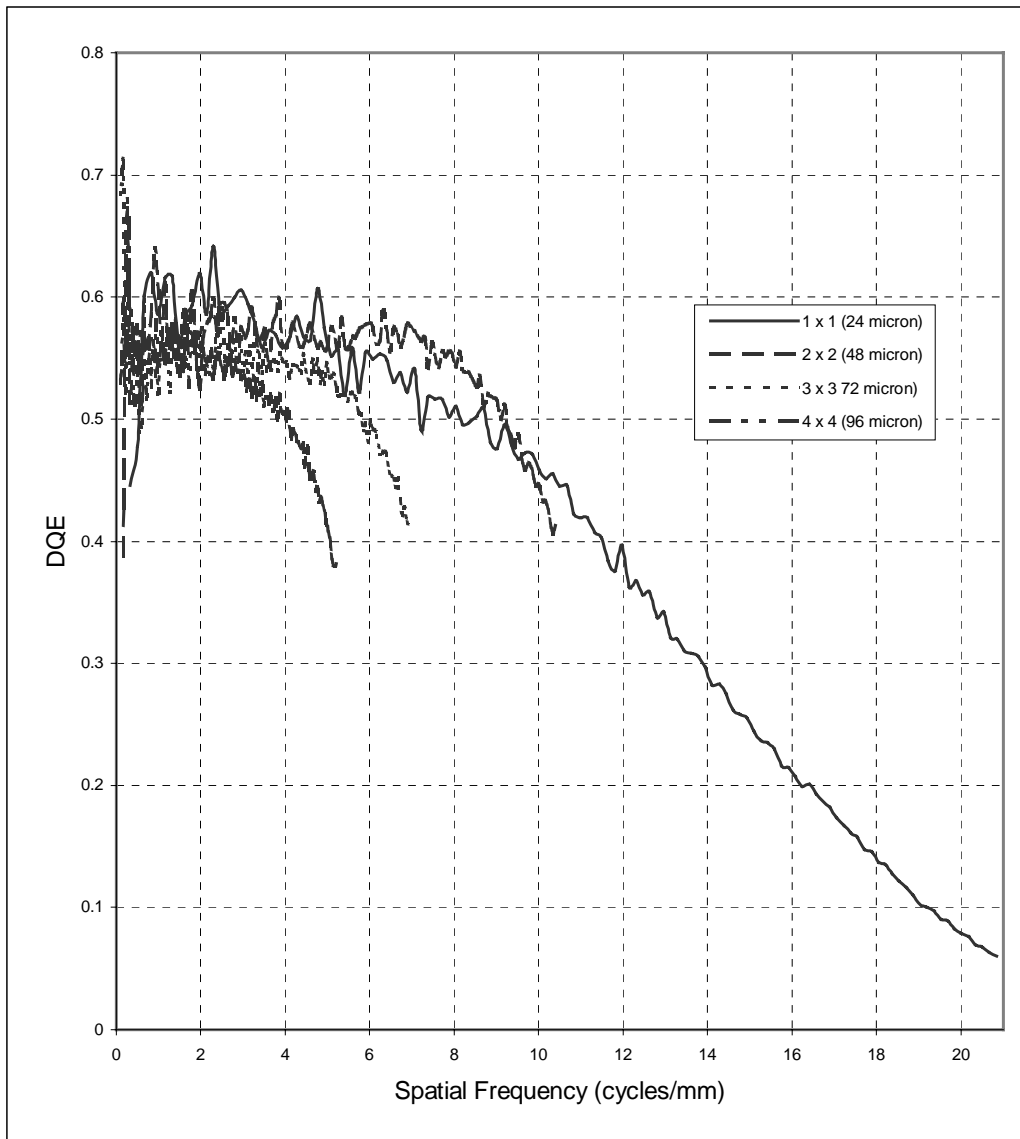


Figure A16. DQE for CsI:Tl with and without binning at 16 mAs. Other than limiting spatial resolution, pixel size does not influence the DQE in this system.

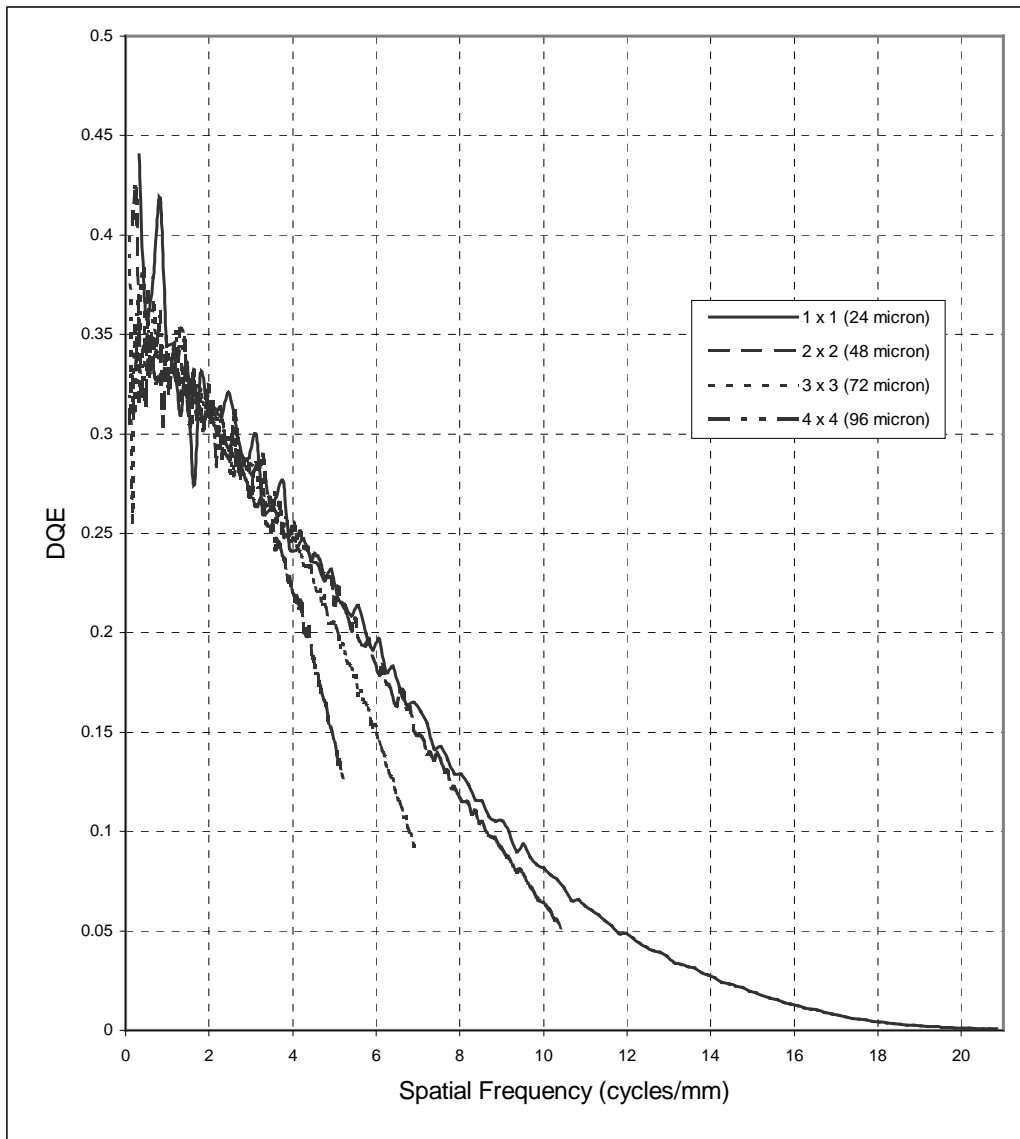


Figure A17. DQE for Kodak MIN-R 2000™ with and without binning at 20 mAs. Other than limiting spatial resolution, pixel size does not influence the DQE in this system.

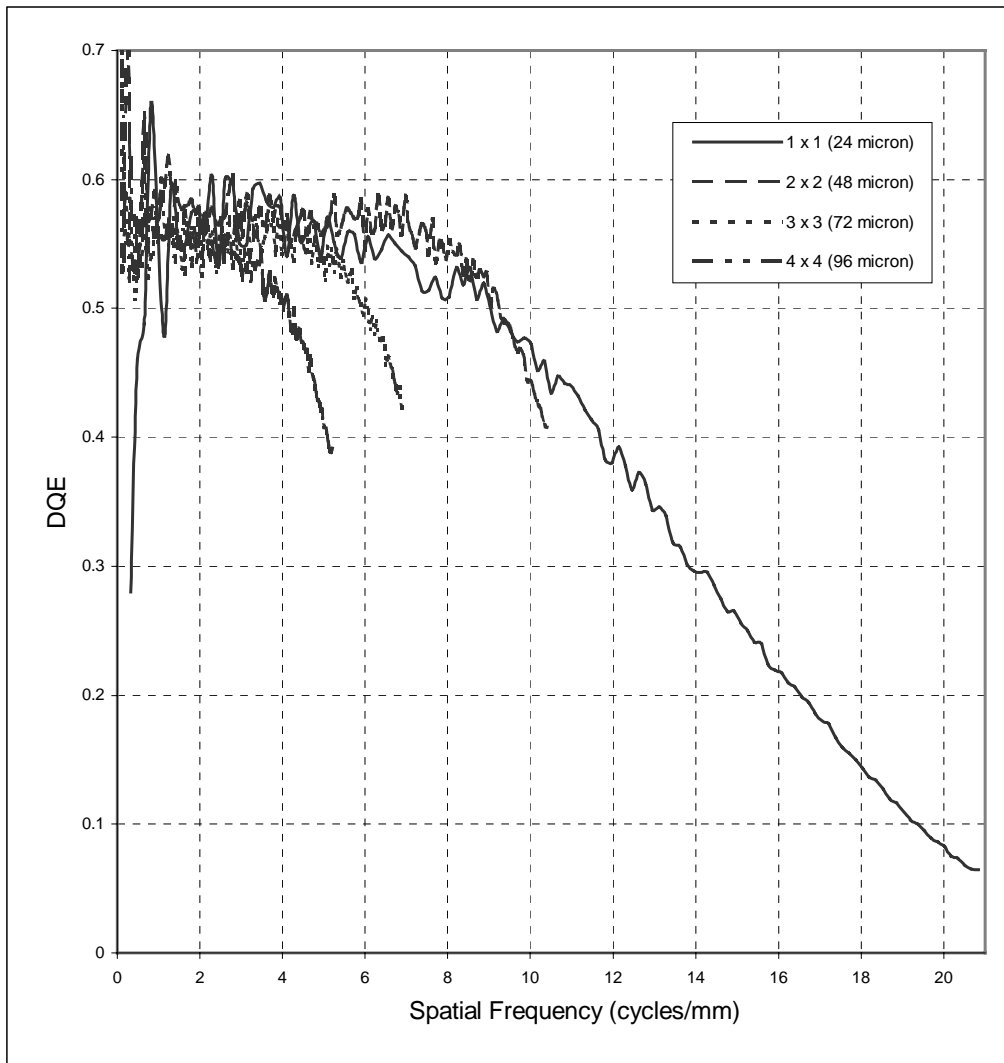


Figure A18. DQE for CsI:Tl with and without binning at 20 mAs. Other than limiting spatial resolution, pixel size does not influence the DQE in this system.